EIT Light Storage of Weak Coherent Pulses in a Doped Solid

EIT Lichtspeicherung schwacher kohärenter Pulse in einem dotierten Festkörper
Dissertation von Marcel Hain, Juni 2021

TECHNISCHE
UNIVERSITÄT
DARMSTADT

Fachbereich Physik
Institut für Angewandte Physik
Nichtlineare Optik / Quantenoptik

EIT Light Storage of Weak Coherent Pulses in a Doped Solid

Vom Fachbereich Physik
der Technischen Universität Darmstadt

zur Erlangung des Grades
eines Doktors der Naturwissenschaften
(Dr. rer. nat.)

genehmigte Dissertation von
M.Sc. Marcel Hain
aus Aschaffenburg

Referent: Prof. Dr. Thomas Halfmann
Korreferent: Prof. Dr. Thomas Walther

Tag der Einreichung: 29. Juni 2021
Tag der Prüfung: 21. Juli 2021

Darmstadt 2021
D17

Marcel Hain: EIT Light Storage of Weak Coherent Pulses in a Doped Solid
Darmstadt, Technische Universität Darmstadt
Jahr der Veröffentlichung der Dissertation auf TUprints: 2021
URN: urn:nbn:de:tuda-tuprints-192571

Tag der mündlichen Prüfung: 21.07.2021

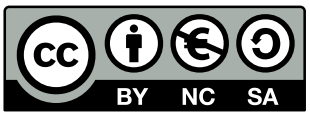

Contents

Introduction

Quantum mechanics enables technologies which are impossible by means of classical physics. Quantum computation speeds up computations, even compared to supercomputers [1, 2]. A prominent example for quantum computation is factorizing a given number by Shor's algorithm [3]. Another important application of quantum computers is the simulation of large quantum systems which is too complex for classical computers [4, 5]. For more powerful quantum computation, several computer nodes can be interconnected to build a quantum internet [6].

For a continental quantum network, transmission losses must be compensated. Briegel *et al.* proposed a quantum repeater protocol to overcome losses and infidelities with reasonably scaling overhead [7]. This protocol requires storage of quantum states in a quantum memory [8, 9]. Important properties of a quantum memory are storage time, efficiency, fidelity, and capacity to simultaneously store multiple input qubits [10].

In optical quantum communication, the exchange of single photons (representing the qubits) connects the nodes. Photons do not interact with each other which makes the communication robust. Due to low losses, high data rates, and robustness, modern communication systems are usually based on fiber networks. These networks can also be used for transmission of single photons. The implementation of optical quantum repeaters requires memories that preserve the quantum state of a photon. A variety of media can serve as an optical quantum memory. The most important examples are warm and cold atomic gases, trapped single ions and atoms, color centers and optical phonons in diamond, quantum dots, and rare-earth ion doped solids (REIDS) [10].

Atomic media provide large optical depth which enables high storage efficiency. Hsiao *et al.* achieved the so far highest light storage efficiency of 92% using electromagnetically induced transparency (EIT) in cold cesium atoms [11]. However, they implemented storage of classical light pulses rather than single photons. Reducing the energy of the stored light pulse to the single photon level is technically challenging because background noise, sometimes intrinsic to the storage protocol, limits the storage fidelity. At the single photon level, Wang *et al.* achieved the highest storage efficiency of 90.6%, also using EIT in a cold atomic gas [12]. However, in these media, the residual motion of the atoms usually limits the storage time to below one millisecond [13]. Only in particular setups, longer storage times (for classical light pulses) of up to 16 s were achieved in gaseous media [14–17].

Solid state media do not suffer from atomic motion and combine robustness with scalability. Among solid state media, REIDS offer an atom-like level structure and exceptionally long coherence lifetimes which enables long light storage times. In previous work in our team, light storage with a storage time of 42 s was implemented in the REIDS Pr^{3+}:Y_2SiO_5 [18, 19]. The longest light storage time so far of 53 min was achieved in the REIDS Eu^{3+}:Y_2SiO_5, though at very low storage efficiency of 0.035% [20]. On the single photon level, the longest storage time of solid state media, also implemented in Eu^{3+}:Y_2SiO_5, is only 1 ms [21]. The efficiency of all these experiments was much smaller compared to atomic media. In previous work,

we implemented a multipass setup to increase the efficiency of storage of classical light pulses at a storage time of 2 µs in Pr^{3+}:Y_2SiO_5 to 76% [22].

There are several appropriate protocols enabling storage of photons. Examples are echo-based memories which rely on shaping absorption features by a specific preparation [e.g., atomic frequency combs (AFC) [23]] or application of external fields [e.g., controlled reversible inhomogeneous broadening (CRIB) [24]]. Many echo-based memories exhibit only little noise which is beneficial for single photon storage with high fidelity. Efficiencies of up to 87% were achieved for storage of single photons using the gradient echo memory (GEM) technique (a variant of CRIB) and up to 38% for single photon storage based on AFC [25, 26]. However, the implementation of echo-based memories is challenging because it requires either a narrowband laser (for AFC) or precise control over an external electric field (for CRIB). In contrast, Raman memories and storage based on EIT are easier to implement [27–29]. However, these protocols require strong optical pulses which raise the background level and make storage of single photons more difficult.

This thesis deals with storage of weak coherent pulses down to the level of a single photon by EIT in the REIDS Pr^{3+}:Y_2SiO_5. We apply a multipass setup to increase the efficiency in combination with a narrowband spectral filter setup to suppress background noise. By combining these setups with techniques to suppress decoherence processes, we achieve storage of weak coherent pulses over several seconds. On shorter timescales in the microsecond regime, we experimentally demonstrate the first implementation of single photon storage using EIT in a solid state medium.

This thesis is structured as follows: In Chapters 1 and 2, we present the EIT light storage protocol and our implementation in the storage medium Pr^{3+}:Y_2SiO_5. We focus on processes limiting the light storage efficiency and the storage time. In Chapter 3, we discuss our spectral filter setup and demonstrate storage of single photons. Chapter 4 deals with our implementation of light storage at a static magnetic field which we use to prolong the storage time in the experiments shown in Chapter 5. In Chapter 6, we demonstrate storage of weak coherent pulses on a timescale of seconds.

An additional task of the research project dealt with the development and implementation of robust pulse sequences for rephasing and population inversion. The rephasing sequences are required to prolong the storage times of our memory. In Chapter 7, we discuss a novel composite sequence for robust population inversion. Finally, we present related experiments on coherent adiabatic population transfer by appropriately designed composite pulse sequences in Chapter 8.

Chapter 1

Basics of EIT Light Storage in Pr^{3+}:Y_2SiO_5

The goal of this work was to store weak coherent pulses in Pr^{3+}:Y_2SiO_5 by EIT. In this chapter, we introduce this storage protocol and present the relevant properties of the storage medium. We focus on attributes which are relevant for efficient and long term storage. Moreover, we discuss techniques to prolong the storage time.

1.1 Light Storage by EIT

We consider a three-level system coupled by two radiation fields, i.e., probe and control (see Figure 1.1). We follow the theoretical treatment given in [30–34] and refer to these references for a more detailed description. We describe the intense control as a classical field by its oscillating electrical field $E_c(\vec{r},t) = \mathcal{E}_c(\vec{r},t)\cos(\omega_c t - \vec{k}_c\vec{r})$ with the slowly varying (compared to ω_c and $|\vec{k}_c|$) envelope $\mathcal{E}_c(\vec{r},t)$ and the weak probe as a quantum field

$$\hat{E}_p(\vec{r},t) = E_p^{(SP)}\left[\hat{\mathcal{E}}_p(\vec{r},t)e^{-i(\omega_p t-\vec{k}_p\vec{r})} + \hat{\mathcal{E}}_p^{\dagger}(\vec{r},t)e^{i(\omega_p t-\vec{k}_p\vec{r})}\right]. \quad (1.1)$$

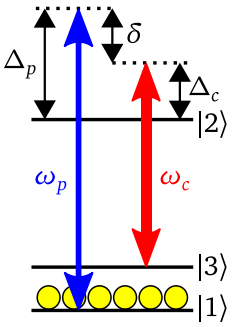

Figure 1.1: Three-level system coupled by the probe (blue) and control (red) fields in a Λ-configuration.

Here, $E_p^{(SP)} = \sqrt{\hbar\omega_p/(2\epsilon_0 V)}$ is the electrical field of a single probe photon in the quantization volume V and $\hat{\mathcal{E}}_p(\vec{r},t)$ is the dimensionless, slowly varying (compared to ω_p and $|\vec{k}_p|$) field operator. Note, that we consider plane waves with wave vectors $\vec{k}_i$ and assume all fields to be polarized in the same direction, i.e., the direction of the atomic dipole moments (hence, we drop the vector arrows). The vacuum wave numbers $|\vec{k}_i|$ are given by the respective angular frequency ω_i via $|\vec{k}_i| = \omega_i/c_0$ ($i = p$ or c) with the vacuum speed of light c_0. In general, the fields might be detuned from their respective transition by $\Delta_p = \omega_p - \omega_{12}$ and $\Delta_c = \omega_c - \omega_{23}$ (where ω_{ij} denotes the angular frequency of the $|i\rangle \leftrightarrow |j\rangle$ transition). However, we first consider the resonant case $\Delta_p = \Delta_c = 0$ and discuss the detuned case at the end of this section.

Using the slowly varying envelope approximation (SVEA), we derive the propagation equation for the probe field amplitude

$$\frac{\partial}{\partial t}\hat{\mathcal{E}}_p(\vec{r},t) + \frac{c_0}{|\vec{k}_p|}\vec{k}_p\vec{\nabla}\hat{\mathcal{E}}_p(\vec{r},t) = 2i\sqrt{N}\Omega_p^{(SP)}\hat{\mathcal{P}}(\vec{r},t), \quad (1.2)$$

where $\Omega_p^{(SP)} = \mu_{12}E_p^{(SP)}/\hbar$ denotes the single photon Rabi frequency with the dipole moment μ_{12} of the probe $|1\rangle \leftrightarrow |2\rangle$ transition and where N is the number of atoms in the interaction volume. Furthermore, we introduced the dimensionless polarization operator $\hat{\mathcal{P}}(\vec{r},t)$ describing the polarization on the probe transition. Equation 1.2 states that $\hat{\mathcal{P}}(\vec{r},t)$ is a source for the propagating probe field and is equivalent to the classical description based on the wave equation derived from Maxwell's equations.

To calculate $\hat{\mathcal{P}}(\vec{r},t)$, we consider the Hamiltonian of the coupled three-level system $\hat{H}=\hat{H}_0+\hat{V}_c+\hat{V}_p$, where $\hat{H}_0=W_1\left|1\right\rangle\left\langle 1\right|+W_2\left|2\right\rangle\left\langle 2\right|+W_3\left|3\right\rangle\left\langle 3\right|$ is the Hamiltonian of the free three-level system, $\hat{V}_c=-\hat{\mu}E_c(\vec{r},t)$ describes the dipole interaction with the control field, and $\hat{V}_p=-\hat{\mu}\hat{E}_p(\vec{r},t)$ is the Hamiltonian of the dipole interaction with the probe field. By applying the rotating wave approximation (RWA) and neglecting off-resonant couplings, we find

$$\hat{V}_c=-\frac{1}{2}\hbar\Omega_c(\vec{r},t)e^{-i(\omega_c t-\vec{k}_c\vec{r})}\left|2\right\rangle\left\langle 3\right|-\frac{1}{2}\hbar\Omega_c(\vec{r},t)e^{i(\omega_c t-\vec{k}_c\vec{r})}\left|3\right\rangle\left\langle 2\right| \tag{1.3}$$

$$\hat{V}_p=-\hbar\Omega_p^{(SP)*}\hat{\mathcal{E}}_p(\vec{r},t)e^{-i(\omega_p t-\vec{k}_p\vec{r})}\left|2\right\rangle\left\langle 1\right|-\hbar\Omega_p^{(SP)}\hat{\mathcal{E}}_p^{\dagger}(\vec{r},t)e^{i(\omega_p t-\vec{k}_p\vec{r})}\left|1\right\rangle\left\langle 2\right|, \tag{1.4}$$

where $\Omega_c(\vec{r},t)=\mu_{23}\mathcal{E}_c(\vec{r},t)/\hbar$ is the control field Rabi frequency with the dipole moment μ_{23} of the control transition $\left|3\right\rangle\leftrightarrow\left|2\right\rangle$. For simplicity we choose the phase of the electric field to yield a real valued control Rabi frequency.

We describe the state of the medium by the density operator $\hat{\rho}(\vec{r},t)$ and assume that only little population is transferred by the weak probe field from state $\left|1\right\rangle$, i.e., we set $\rho_{11}=1$ in good approximation. The evolution of the coherence operators $\hat{\rho}_{21}(\vec{r},t)$ and $\hat{\rho}_{31}(\vec{r},t)$ is then given by the coupled differential equations

$$\frac{\partial}{\partial t}\hat{\rho}_{31}(\vec{r},t)=-i(\omega_p-\omega_c)\hat{\rho}_{31}(\vec{r},t)+\frac{i}{2}\Omega_c(\vec{r},t)e^{i(\omega_c t-\vec{k}_c\vec{r})}\hat{\rho}_{21}(\vec{r},t) \tag{1.5}$$

$$\begin{aligned}\frac{\partial}{\partial t}\hat{\rho}_{21}(\vec{r},t)=&-i\omega_p\hat{\rho}_{21}(\vec{r},t)+\frac{i}{2}\Omega_c(\vec{r},t)e^{-i(\omega_c t-\vec{k}_c\vec{r})}\hat{\rho}_{31}(\vec{r},t)\\&+i\Omega_p^{(SP)*}\hat{\mathcal{E}}_p(\vec{r},t)e^{-i(\omega_p t-\vec{k}_p\vec{r})}.\end{aligned} \tag{1.6}$$

To solve Equations 1.5 and 1.6, we define the slowly varying coherence operators $\hat{\varrho}_{31}(\vec{r},t)$ and $\hat{\varrho}_{21}(\vec{r},t)$ via $\hat{\rho}_{31}(\vec{r},t)=\hat{\varrho}_{31}(\vec{r},t)\exp\{-i[(\omega_p-\omega_c)t-\vec{\kappa}\vec{r}]\}$ with the wave vector $\vec{\kappa}=\vec{k}_p-\vec{k}_c$ and $\hat{\rho}_{21}(\vec{r},t)=\hat{\varrho}_{21}(\vec{r},t)\exp\{-i(\omega_p t-\vec{k}_p\vec{r})\}$. Furthermore, we define the spin wave and polarization operators $\hat{S}(\vec{r},t)=\sqrt{N}\hat{\varrho}_{31}(\vec{r},t)$ and $\hat{\mathcal{P}}(\vec{r},t)=\sqrt{N}\hat{\varrho}_{21}(\vec{r},t)$ which act (analog to the field operator $\hat{\mathcal{E}}_p$) as annihilation operators for the respective excitation. Inserting in Equations 1.5 and 1.6 yields

$$\frac{\partial}{\partial t}\hat{S}(\vec{r},t)=\frac{i}{2}\Omega_c(\vec{r},t)\hat{\mathcal{P}}(\vec{r},t) \tag{1.7}$$

$$\frac{\partial}{\partial t}\hat{\mathcal{P}}(\vec{r},t)=i\sqrt{N}\Omega_p^{(SP)*}\hat{\mathcal{E}}_p(\vec{r},t)+\frac{i}{2}\Omega_c(\vec{r},t)\hat{S}(\vec{r},t). \tag{1.8}$$

The polarization operator represents essentially the spatio-temporal variation of the atomic coherence on the probe transition of an ensemble of N atoms. Analog to classical electromagnetism, it describes the density of the induced electric dipole moments in the medium. Accordingly, the spin wave operator represents the atomic coherence on the $\left|1\right\rangle\leftrightarrow\left|3\right\rangle$ transition. Typically, states $\left|1\right\rangle$ and $\left|3\right\rangle$ are different spin states, hence the name spin wave. Based on Equations 1.2, 1.7, and 1.8, we explain the different steps of EIT light storage which are schematically depicted in Figure 1.2. Initially **(i)**, there is no spin wave and we apply a control field, called the control write pulse. When we apply a probe pulse **(ii)**, the field creates a polarization according to Equation 1.8 which then generates a spin wave according to Equation 1.7. Due to the influence of the polarization on the probe field propagation (see Equation 1.2), the probe pulse is slowed down and spatially compressed in the medium. This

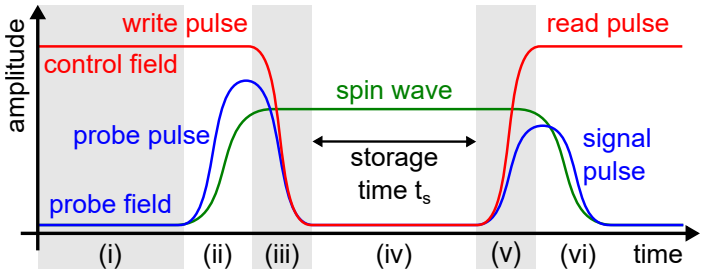

Figure 1.2: Sequence of the EIT light storage protocol (see main text). We plot the amplitude of the control field (red), the probe field (blue) and the spin wave (green) over time. Figure taken from [35], modified.

effect is called slow light. When the probe pulse is completely in the medium, we adiabatically turn off the control field in parallel to the probe pulse **(iii)** such that the spin wave remains. During the storage time **(iv)**, we do not apply any field and the spin wave evolves freely (see Equation 1.7). Since the spin wave is proportional to the coherence on the $|1\rangle \longleftrightarrow |3\rangle$ transition, techniques to prolong the lifetime of this coherence can be applied for prolonging the light storage time. For readout, we apply the control read pulse **(v)** which converts the spin wave to the polarization which in turn generates the signal pulse according to Equation 1.2. Finally, the signal pulse leaves the medium under slow light conditions **(vi)**.

In general, we can apply the control field in different directions during the write and read processes. The wave vector of the spin wave depends on the probe and control write pulse wave vectors $\vec{k}_p$ and $\vec{k}_w$ via $\vec{\kappa} = \vec{k}_p - \vec{k}_w$ (see calculations above). During readout, the signal wave vector is then $\vec{k}_s = \vec{\kappa} + \vec{k}_r$ (with the control read pulse wave vector $\vec{k}_r$) [36]. In our setup, we choose the same control beam path for the write and read pulses, i.e., $\vec{k}_r = \vec{k}_w$. Therefore, the signal pulse is emitted in the direction of the probe pulse, i.e., $\vec{k}_s = \vec{k}_p$. This configuration is called forward readout. Other configurations are possible and might enable a higher storage efficiency [33]. However, these configurations are very sensitive to alignment and cannot easily be combined with our multipass setup to increase the efficiency [35, 37].

EIT light storage was first implemented by Liu *et al.* and Phillips *et al.* in atomic gases [28, 29]. Under ideal conditions, the signal pulse resembles the probe pulse in all parameters, i.e., frequency, polarization, direction of propagation and amplitude. Thus, at the single photon level, the quantum state of a probe photon can be preserved, i.e., EIT light storage is a quantum memory protocol [38]. The main challenge of implementing EIT as a quantum memory can be seen in steps **(v)** and **(vi)**. The signal pulse is obtained when we apply the control read pulse. This requires separation of the weak signal pulse from the background of the strong control read pulse. For storage of classical probe pulses, sufficient separation can usually be achieved spatially (by choosing different beam paths). At the single photon level, however, additional filtering becomes necessary (see Chapters 3 and 6).

During the write and read processes, the probe and signal pulses propagate through the medium without being absorbed despite the population in $|1\rangle$. This is EIT. The susceptibility χ for the case of nonzero detunings Δ_p and Δ_c reads [32]

$$\chi = \frac{|\mu_{12}|^2 N}{\epsilon_0 \hbar V} \frac{\left[4\delta\left(|\Omega_c|^2 - 4\delta\Delta_p\right) - 4\Delta_p\gamma_{13}^2\right] + i\left[8\delta^2\gamma_{12} + 2\gamma_{13}\left(|\Omega_c|^2 + \gamma_{13}\gamma_{12}\right)\right]}{\left||\Omega_c|^2 + (\gamma_{12} + i2\Delta_p)(\gamma_{13} + i2\delta)\right|^2}. \tag{1.9}$$

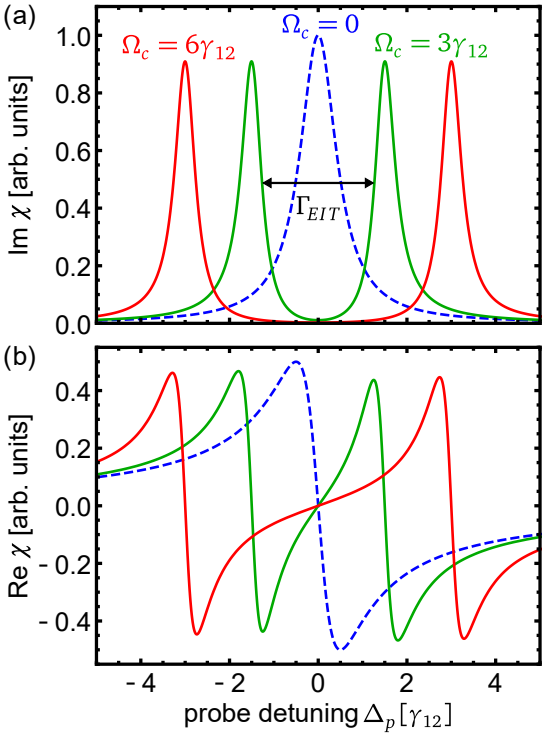

Figure 1.3: Susceptibility χ versus probe detuning Δ_p calculated for different control Rabi frequencies Ω_c, assuming a ground state decoherence rate $\gamma_{13} = 0.1\gamma_{12}$. (a) The imaginary part of χ determines the absorption. For $\Omega_c = 0$ (dashed, blue graph), we find a Lorentzian absorption peak which splits into two peaks for $\Omega_c > 0$ (solid graphs) with nearly perfect transmission (EIT) in between, i.e., at $\Delta_p = 0$. With larger Ω_c, the splitting and the EIT window width Γ_{EIT} increase and the residual absorption decreases (compare red and green graphs). (b) The imaginary part of χ shows anomalous dispersion on the absorption peaks and normal dispersion in the EIT window (positive slope of the solid graphs at $\Delta_p = 0$). The slope decreases with higher Ω_c (compare red and green graphs).

Here, γ_{ij} denotes the decoherence rate of the $|i\rangle \leftrightarrow |j\rangle$ transition and $\delta = \Delta_p - \Delta_c$ is the two-photon detuning. EIT becomes apparent when we consider the absorption coefficient α and refractive index n for light with wavelength λ

$$\alpha = \frac{4\pi}{\lambda}\,\mathrm{Im}\,\sqrt{1+\chi} \approx \frac{2\pi}{\lambda}\,\mathrm{Im}\,\chi \qquad \text{and} \qquad n = \mathrm{Re}\,\sqrt{1+\chi} \approx 1 + \frac{1}{2}\,\mathrm{Re}\,\chi\,. \quad (1.10)$$

Figure 1.3 shows the imaginary (a) and real (b) part of χ versus the probe detuning for different control Rabi frequencies Ω_c. For $\Omega_c = 0$ (i.e., when state $|3\rangle$ is irrelevant), we find the expected Lorentzian absorption profile. When we apply a control field, we observe two absorption peaks which are split by Ω_c. Around $\Delta_p = 0$, i.e., where we found maximal absorption for $\Omega_c = 0$, the medium now exhibits very low absorption. This is EIT. The slight residual absorption is due to the ground state decoherence with rate $\gamma_{13} \neq 0$ and can be suppressed by increasing Ω_c (note the lower residual absorption for $\Omega_c = 6\gamma_{12}$ compared to $\Omega_c = 3\gamma_{12}$). The lower absorption of the peaks in the EIT case compared to $\Omega_c = 0$ is also caused by $\gamma_{13} \neq 0$.

We define the EIT window width Γ_{EIT} as the full spectral width at a transmission $T = \exp(-\alpha l) = 0.5$ (with the medium length l). Using Equation 1.9, we find in first approximation, i.e., for $|\Delta_p| \ll \Omega_c^2/\gamma_{12}$:

$$\Gamma_{EIT} = \frac{\Omega_c^2\sqrt{\ln 2}}{\gamma_{12}\sqrt{\mathrm{OD}}}. \quad (1.11)$$

Here, $\mathrm{OD} = \alpha_0 l$ denotes the optical depth of the medium with absorption coefficient (for $\Omega_c = 0$) $\alpha_0 = 4\pi|\mu_{12}|^2 N/(\lambda\gamma_{12}\epsilon_0\hbar V)$. We note that for typical values of OD $\lesssim 10$, the approximation is barely fulfilled at the edges of the EIT window. This is due to the rather broad definition of Γ_{EIT}. If we defined Γ_{EIT} as the width at higher T (i.e., lower Im χ) then the approximation would be fulfilled better. Nevertheless, we find

that Γ_{EIT} scales predominantly with the square of the control Rabi frequency Ω_c.

Figure 1.3(b) depicts the dispersion relation for the three different control Rabi frequencies. For $\Omega_c = 0$, we find the expected anomalous dispersion (negative slope of Re χ) on the resonance, i.e., for $\Delta_p = 0$. For $\Omega_c \neq 0$, however, the medium exhibits normal dispersion (positive slope of Re χ) in the EIT window. Due to the dependence of the group velocity v_g on the dispersion $\mathrm{d}n/\mathrm{d}\omega_p$ via

$$v_g = \frac{c_0}{n + \omega_p \frac{\mathrm{d}n}{\mathrm{d}\omega_p}} = \frac{c_0}{1 + c_0 \alpha_0 \frac{\gamma_{12}}{\Omega_c^2}} \approx \frac{\Omega_c^2}{\alpha_0 \gamma_{12}}, \tag{1.12}$$

where we set $\gamma_{13} = 0$, the dispersion causes a reduction of the group velocity which is slow light by EIT. We find, that v_g can be controlled experimentally by changing Ω_c. For typical values of our experiments ($\Omega_c \approx \gamma_{12} \approx 2\pi \times 100\,\mathrm{kHz}$ and $\alpha_0 \approx 10^3\,\mathrm{m}^{-1}$), we obtain $v_g \approx 600\,\mathrm{m/s}$, i.e., a reduction of the group velocity by a factor of about 5×10^5 compared to c_0. This extremely low and experimentally controllable group velocity combined with the high transmission of the EIT window are the key features which enable EIT light storage.

The light storage efficiency η_{LS}, defined as the ratio of the signal and probe pulse energies (or equivalently for storage of a single probe photon, as the probability to obtain a signal photon), depends on the shape of the probe pulse. In order to avoid absorption, the spectral bandwidth of the probe pulse must be narrower than the EIT window width, i.e., we obtain lower absorption for temporally longer probe pulses. This spectral condition can be expressed for a probe pulse with duration τ_p as

$$\Gamma_{EIT} \approx \frac{\Omega_c^2}{\gamma_{12}\sqrt{\mathrm{OD}}} \gg \frac{1}{\tau_p} \Leftrightarrow \frac{\Omega_c^2 \tau_p}{\gamma_{12}} \gg \sqrt{\mathrm{OD}}. \tag{1.13}$$

However, the spatial condition demands that the probe pulse must fit completely

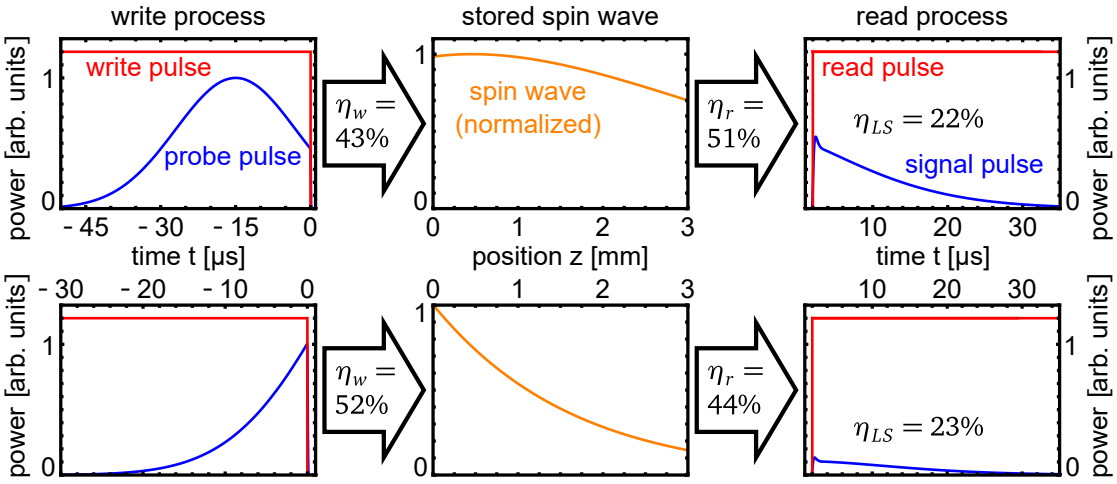

Figure 1.4: Optical power versus time and spin wave amplitude versus position for simulated EIT light storage in a $l = 3\,\mathrm{mm}$ long medium with $\mathrm{OD} = \alpha_0 l = 5$. We simulate storage of truncated Gaussian probe pulses by control pulses with $\Omega_c = 2\pi \times 200\,\mathrm{kHz}$.

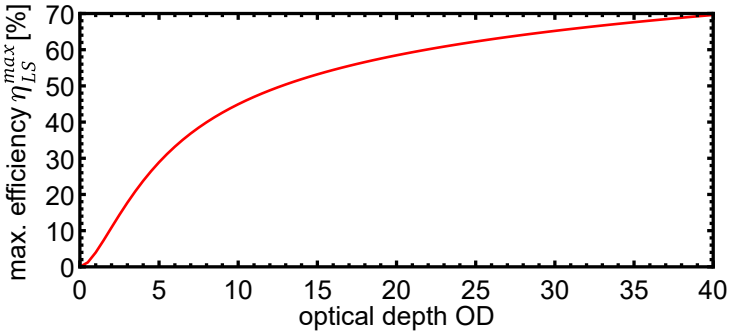

Figure 1.5: Theoretical maximum light storage efficiency versus OD for forward readout. The data was calculated based on [34].

into the medium during the write process and favors short probe pulses:

$$l \geq v_g \tau_p \approx \frac{\Omega_c^2 \tau_p}{\alpha_0 \gamma_{12}} \Leftrightarrow \mathrm{OD} \gtrsim \frac{\Omega_c^2 \tau_p}{\gamma_{12}}. \tag{1.14}$$

This simple consideration shows that the probe pulse shape has to fulfill a compromise between the spectral and spatial condition in order to be stored with high efficiency. We also find that we better fulfill both conditions simultaneously for higher OD, i.e., we achieve higher efficiency for higher OD.

Figure 1.4 shows a simulation of EIT light storage of two different probe pulse shapes based on the differential equations derived above. We find that the write and read efficiencies η_w and η_r vary with the probe pulse shape (compare the two rows). This is due to the different shapes of the spin wave which are either optimal for reading (top) or for writing (bottom). Gorshkov *et al.* found that $\eta_{LS} = \eta_w \eta_r$ is maximized when η_w and η_r are equal, i.e., when the spin wave fulfills a compromise between optimal storage and readout [33]. This compromise can be found by optimizing the temporal probe pulse shape in an iterative process, i.e., a pulse shaping algorithm, which was first implemented by Novikova *et al.* [39]. We present the algorithm in Section 5.2 along with our experimental implementation. Gorshkov *et al.* also showed that the highest possible efficiency η_{LS}^{max} depends only on the the OD as depicted in Figure 1.5 [33, 34]. With higher OD, η_{LS}^{max} increases. Perfect storage, i.e., $\eta_{LS}^{max} = 1$, can only be achieved in the limit of infinite OD.

1.2 Relevant Spectroscopic Properties of Pr^{3+}:Y_2SiO_5

EIT light storage is often implemented in atomic gases due to their spectrally narrow and isolated optical transitions with high OD [28, 29, 40]. However, the storage time in atomic gases is usually limited to the millisecond range. An attractive alternative to atomic media are REIDS. Solid state media have the benefit of being scalable, are easy to implement and do not suffer from motional decoherence processes. A special feature of REIDS is the narrow homogeneous linewidth of the optical transitions combined with low decoherence rates. We implement EIT light storage in the REIDS Pr^{3+}:Y_2SiO_5 (Pr:YSO for short).

In Pr:YSO, the praseodymium dopant ions Pr^{3+} replace yttrium ions at two different crystallographic sites. We perform our experiments on the $^3H_4 \leftrightarrow {}^1D_2$ transition[1] of site 1 (nomenclature corresponding to [41]) at a wavelength of $\lambda_0 = 605.98\,\mathrm{nm}$ (see

[1] Russel-Saunders notation $^{2S+1}L_J$

Figure 1.6). In the free ion this transition is dipole forbidden but the crystal field lifts the $(2J+1)$-fold degeneracy and weakly allows dipole transitions. The weakness of the coupling leads to a long population lifetime of the excited state $T_1^e = 164\,\mu s$ [42]. The transitions take place within the 4f orbital which is shielded from external fields by the larger, fully populated 5s and 5p orbitals. Due to the low interaction of Pr^{3+} ions with the Y_2SiO_5 host and other Pr^{3+} ions (at typical dopant concentrations below 0.1%), the decoherence time of the optical transition is not much lower than T_1^e which leads to a narrow homogeneous linewidth of $\gamma^e = 2\pi \times 2.9\,\text{kHz}$ [41, 42].

The inhomogeneous linewidth $\Gamma^e \approx 2\pi \times 7\,\text{GHz}$ is, however, significantly larger. This is due to stress in the crystal lattice caused by the slightly different atomic radii of praseodymium and yttrium. The stress leads to different crystal fields (and hence crystal field splittings) at the different positions of the Pr^{3+} ions.

The crystal field splittings are in the order of terahertz. We optically couple only the lowest of the states and perform our experiments at temperatures below 4 K. Therefore, phononic excitation of other crystal field states is suppressed. However, population of the excited state can decay spontaneously to higher ground states (i.e., substates of $^3H_4$) and cause fluorescence at wavelengths $\lambda > 606\,\text{nm}$.

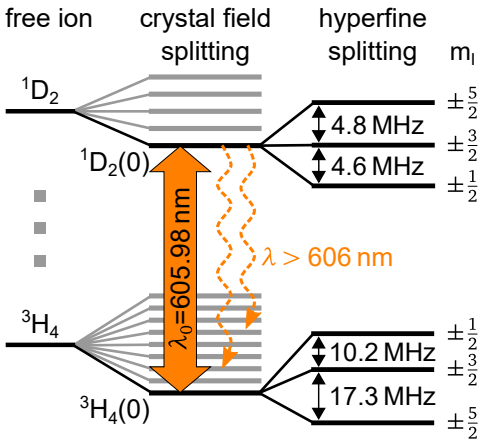

Figure 1.6: Level scheme of a free Pr^{3+} ion and splittings due to the Y_2SiO_5 crystal field and hyperfine interaction. Figure taken from [35], modified.

The nuclear spin of praseodymium causes a hyperfine splitting in the range of $\Delta\nu_{hfs} \approx 10\,\text{MHz}$, i.e., at radio frequencies (RF). At zero external magnetic field, each of the lowest crystal field states splits into three doubly degenerate hyperfine states (see Figure 1.6). Due to $\Gamma^e \gg 2\pi \times \Delta\nu_{hfs}$, the optical transitions between these hyperfine states are hidden in the inhomogeneous line. To address individual transitions, the population of the $^3H_4(0)$, $m_I = -\frac{5}{2}, \ldots, +\frac{5}{2}$ ground states (which is equally distributed in thermal equilibrium) has to be prepared by an optical pumping sequence. We use different preparation sequences throughout this work, each matched to the specific requirements of the experiments and explained in the respective chapter. Optical pumping is possible due to the long ground state population relaxation time $T_1 \lesssim 100\,\text{s}$ at cryogenic temperatures compared to the decay time of the optically excited state $T_1^e = 164\,\mu s$ [43]. Furthermore, it is this long T_1 time that enables a coherence lifetime, i.e., light storage time, up to the range of a minute [19]. However, we must apply several techniques to overcome decoherence processes in order to reach such long storage times.

1.2.1 Rephasing

EIT light storage uses the spin wave, i.e., the spatio-temporal variation of the atomic coherence among ground states, to store the probe pulse. In Pr:YSO, the ground state transition is inhomogeneously broadened with a linewidth of $\Gamma \approx 2\pi \times 30\,\text{kHz}$ [41]. This means that the phases of the individual coherences within the inhomogeneous

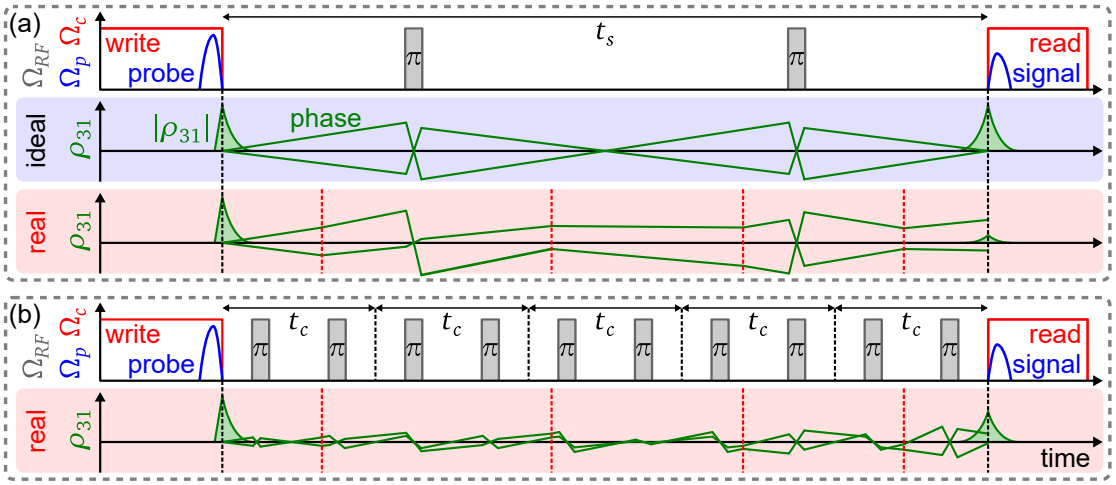

Figure 1.7: Rephasing and dynamical decoupling (DD) of an atomic coherence (at a fixed spatial position, i.e., with well-defined initial phase) generated by EIT light storage. (a) The top row shows the sequence of the applied optical [control (red) and probe (blue)] and RF pulses (gray). The middle and lower rows show the amplitude (filled curve) of the total coherence ρ_{31} (summed over the inhomogeneous line) and the phase evolution of two constituting coherences (green lines) with different transition frequencies. The middle row depicts the ideal situation of a constant environment and the lower row the real environment causing spontaneous changes of the transition frequencies (at the times indicated by the red, dashed lines). (b) Pulse sequence (top) and evolution of the coherence (bottom) for DD, i.e., application of π pulses with a cycle time t_c shorter than the noise's correlation time. Figure taken from [18], modified.

line have a different time evolution (given by their transition frequencies). Therefore, the spin wave suffers from destructive interference with a characteristic $1/e$ time of $T_2^* = 2\sqrt{2\ln 2}/\Gamma \approx 10\,\mu s$ (assuming a Gaussian frequency distribution with FWHM Γ). In the context of this work we call this deterministic process dephasing and other (usually stochastic) processes leading to a loss of coherence decoherence.

Dephasing is well known from nuclear magnetic resonance (NMR). There are a multitude of techniques to counteract dephasing and decoherence. In the simplest case, we apply a single RF π pulse (resonant to the transition with the coherence) to recover the spin wave (or magnetization in the case of NMR). The π pulse inverts the phases of all coherences so that the following free evolution leads to a rephasing, i.e., constructive interference. In NMR, the magnetization is usually generated by an RF $\pi/2$ pulse and the recovered signal is then called a spin echo. We use spin echoes for evaluating the coherence time at different magnetic fields (see Section 4.1).

For EIT light storage we must apply an even number of π pulses to ensure phase matching and a properly prepared population distribution (see [44, 45] for a comparison of spin echo and EIT light storage). Figure 1.7(a) illustrates the effect of the π pulses on two atomic coherences. Shortly after the storage, the dispersing phases lead to destructive interference and a vanishing net coherence (i.e., spin wave). Ideally, the π pulses invert the phases such that they are in phase after the storage time t_s. However, in the real situation the transition frequencies (i.e., the slopes of the phase evolution in Figure 1.7) fluctuate stochastically. In Pr:YSO this is mainly due to spin flips of yttrium ions in the vicinity of the praseodymium ions causing minor changes in the local magnetic field [46]. Because of the varying frequencies,

the spin wave is not rephased perfectly after t_s, i.e., the signal amplitude is reduced.

Dynamical decoupling (DD) is a typical countermeasure to overcome this perturbing effect [47–49]. The basic idea of DD is to apply several rephasing sequences, each with a duration (also: cycle time) t_c, within the storage time [see Figure 1.7(b)]. When t_c is shorter than the correlation time of the frequency fluctuation the perturbing effect of the varying frequencies is suppressed. This is due to the shorter timescale at which the phase changes evolve. With shorter t_c, better decoupling from external influences (causing the frequency variation) can be achieved, i.e., the spin wave can be preserved for longer times. In the limit of perfect decoupling, the coherence time is only limited by spontaneous decay, i.e., to $2T_1 \approx 200\,\mathrm{s}$ in Pr:YSO.

A common problem with DD is that the rephasing efficiency suffers from imperfections of the π pulses. Due to the usually large number of applied π pulses (more than 10^4 pulses were applied for $t_s = 1\,\mathrm{s}$ in previous work [18]), even minor imperfections can cause a significant reduction of the signal amplitude. There are two different approaches to reduce this signal loss [50]. First, the pulse imperfections can be reduced by replacing the π pulses by more robust pulses, e.g., applying the techniques of adiabatic passage [51–53] or shortcuts to adiabaticity [54]. Second, we can exploit the phases of the pulses as control parameters to design a pulse sequence which is overall robust with regard to errors induced by the single pulses [50, 55–57]. In this thesis, we apply the second kind of error compensation, namely universally robust DD sequences [57] and universal composite pulses (UCPs) [58]. We introduce the universally robust DD sequences in Section 5.3 and discuss their application to increase the light storage efficiency for storage of weak coherent pulses (see Chapter 6). In Chapter 7 we introduce and characterize different UCPs.

1.2.2 Prolongation of Coherence Times by Static Magnetic Fields

In Pr:YSO we can apply DD to suppress decoherence due to spin flips of yttrium ions causing changes in the local magnetic field. However, due to different experimental limitations, e.g., pulse imperfections and heating due to high RF power, we cannot achieve perfect decoupling of the spin wave from the environment. To reduce the remaining effect of the environment, we apply a static magnetic field. This field reduces the rate of the yttrium spin flips in the vicinity of the praseodymium ions and additionally lowers the effect of those spin flips on the spin wave for specifically chosen field amplitudes and directions.

The reduction of the spin flip rate is due to an enhancement of the so-called frozen core effect [60, 61]. In Pr:YSO, the magnetic moment of the Pr^{3+} ions dominates that of the Y^{3+} ions [62]. The large magnetic moments of the Pr^{3+} ions align the moments of the Y^{3+} ions in their vicinity (see Figure 1.8). The region of aligned Y^{3+} moments is called the frozen core. Due to the Zeeman effect, the energy associated with an Y^{3+} spin flip in the frozen core differs from that of the surrounding Y^{3+} ions. Therefore, spin exchange processes between the Y^{3+} ions in the frozen core and the surrounding ions are suppressed.

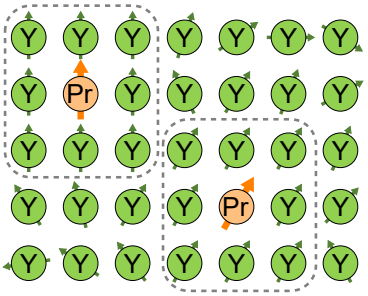

Figure 1.8: Sketch of frozen cores in Pr:YSO. Figure taken from [59], modified.

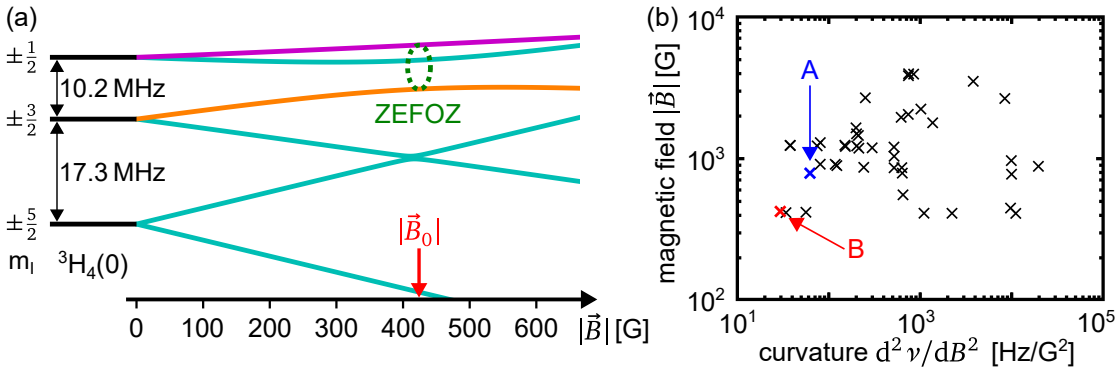

Figure 1.9: ZEFOZ in Pr:YSO. (a) Level splitting of magnetic site 1 of the $^3H_4(0)$ ground state when a magnetic field in the direction of $\vec{B}_0$, i.e., ZEFOZ point "B", is applied. Calculation based on [63]. (b) Magnitude of the magnetic field $|\vec{B}|$ and the curvature of the transition frequency $d^2\nu/dB^2$ at different ZEFOZ points in Pr:YSO (marked by the crosses). In our work, we use the point labeled "B". Figure (b) taken from [64], modified.

In a static magnetic field, the magnetic moment of the Pr^{3+} ions is increased and the frozen cores are enlarged. Therefore, an external magnetic field leads to an enhanced frozen core effect, a reduction of Y^{3+} spin flips and hence an increased coherence time. Furthermore, the magnetic field lifts the degeneracy of the hyperfine states. Due to two different orientations of the Pr^{3+} nuclear spins in the crystal lattice (called magnetic sites), each of the hyperfine states splits into four. In each of the two magnetic sites we find six ground states and six optically excited states. Figure 1.9(a) shows the calculated level splitting of magnetic site 1 when we apply a magnetic field in a specific direction. At low magnetic fields ($|\vec{B}| \lesssim 100\,\mathrm{G}$), the splitting depends linearly on the magnetic field (Zeeman regime).

At higher fields, however, the splitting becomes nonlinear. As a result from this nonlinearity, there are specific magnetic fields (e.g., $\vec{B}_0$) at which the frequency ν of a transition between two states [orange and purple in Figure 1.9(a)] does (to first order) not depend on $\vec{B}$. This is called a zero first order Zeeman shift (ZEFOZ) and the corresponding magnetic field is called a ZEFOZ point. Note that the vanishing dependence of ν on the magnetic field has to be fulfilled for all three components of $\vec{B}$. For simplicity, we depict only one direction in Figure 1.9(a). When we prepare a coherence on a transition under ZEFOZ conditions, it is to first order decoupled from fluctuations of the magnetic field. Since these fluctuations (mainly caused by yttrium spin flips) dominate the decoherence in Pr:YSO [46], ZEFOZ substantially prolongs the coherence time. In previous work of our team, the coherence time was prolonged by a factor of 780 using the ZEFOZ technique [18].

The remaining influence of magnetic field fluctuations at a ZEFOZ point is dominated by second order effects which depend on the curvature $d^2\nu/dB^2$. Longdell *et al.* calculated several ZEFOZ points in Pr:YSO [64] which are depicted as crosses in Figure 1.9(b). The points are characterized by the magnitude of their magnetic field (lower values are typically easier to implement) and their curvature (lower values enable longer coherence times). Prior to this work, the point labeled "A" was commonly used [18, 19, 65–69] but point "B" has a lower curvature at a lower magnetic field and is therefore expected to be superior [64]. Hence, we use the ZEFOZ point labeled "B" in this work.

Chapter 2

Experimental Setup

The goal of this work was to apply the EIT light storage scheme in a Pr:YSO crystal for storage of weak coherent pulses on the timescale of seconds. In this chapter, we present the required setup for EIT light storage in Pr:YSO. While the long ground state population lifetime of Pr:YSO enables storage times in the regime of a minute, it is necessary to apply coherence control techniques in order to reach such long storage times. In this chapter, we show the electrical setups for generating static and dynamic magnetic fields which we use to implement coherence control techniques. Due to the large inhomogeneous linewidth of the optical transition in Pr:YSO, it is necessary to prepare the population by a sequence of optical pumping pulses in order to enable EIT. In the last section of this chapter, we present our preparation sequence and demonstrate EIT light storage.

2.1 Optical Setup

We intend to implement the EIT light storage protocol on hyperfine substates of the ${}^3H_4 \leftrightarrow {}^1D_2$ transition of Pr:YSO. Therefore, we require a coherent light source emitting at a wavelength of $\lambda_0 = 605.98\,\text{nm}$ which we present below. We also show our setup of optical beams for EIT and present a multipass setup for increasing the storage efficiency.

2.1.1 Laser System Based on an Optical Parametric Oscillator

For the generation of coherent light with a wavelength of $\lambda_0 = 605.98\,\text{nm}$, we convert laser light with $\lambda_p = 1064\,\text{nm}$ using an optical parametric oscillator (OPO) and sum frequency generation (SFG). We use a commercial OPO[1], extended by intra-cavity SFG. It was developed in previous work [43, 70] and modified in the context of this thesis.

The laser system is sketched in Figure 2.1. We use an amplified[2] fiber laser[3] to generate coherent light with a wavelength of $\lambda_p = 1064\,\text{nm}$ and up to $P_p = 16\,\text{W}$ power. Note that the seed fiber laser differs from the one used in previous work [18, 43, 44]. This light is then converted in an OPO to signal and idler radiation with wavelengths $\lambda_s = 1408\,\text{nm}$ and $\lambda_i = 4335\,\text{nm}$. The OPO process occurs in a periodically poled lithium niobate (PPLN) crystal as the nonlinear medium and is enhanced by a bow-tie resonator for the signal radiation. Due to the fan-out structure of the poling period (see Figure 2.1), the phase matching can be tuned by shifting the crystal with respect to the pump beam (as well as by temperature tuning). The

[1] Argos Model 2400 SF-15, Lockheed Martin Aculight

[2] YAR-15K-1064-LP-SF, IPG Photonics

[3] Koheras ADJUSTIK Y10 PM FM, NKT Photonics

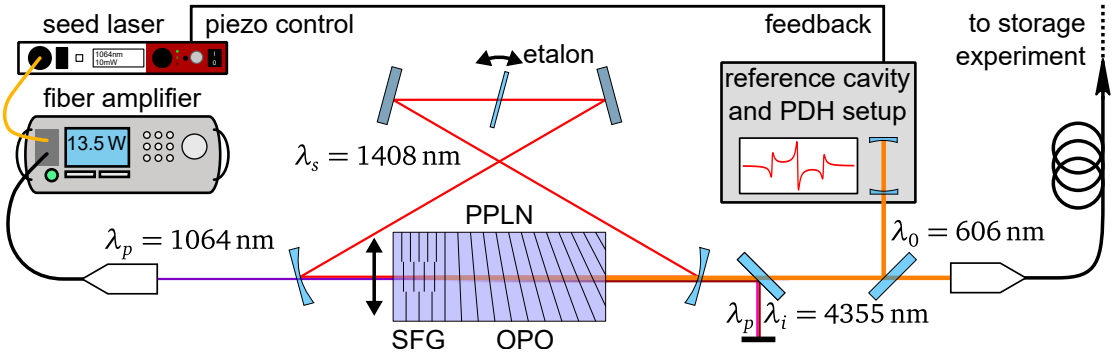

Figure 2.1: Sketch of the laser system used in this work. The pump beam is depicted in purple, the signal in red and the idler in dark red. The sum frequency with wavelength $\lambda_0 = 606\,\mathrm{nm}$ is illustrated in orange.

resonator has a free spectral range of 750 MHz and contains a low finesse etalon to suppress simultaneous operation of more than one resonator mode.

To generate the output light, the PPLN crystal contains a section with a different poling period, optimized for SFG. In this section, the signal and the pump radiation mix to the output light with $\lambda_0 = 606\,\mathrm{nm}$. The phase matching of the SFG section can be adjusted coarsely by choosing one of three tracks with different poling periods and within a track by temperature tuning. The OPO and SFG sections of the PPLN crystal have a length of 42.5 mm and 7 mm, respectively. From these lengths we calculate the acceptance bandwidths of the quasi-phase-matching $\Delta\nu_{OPO} = 93\,\mathrm{GHz}$ and $\Delta\nu_{SFG} = 239\,\mathrm{GHz}$ using the software SNLO (AS Photonics). Since $\Delta\nu_{SFG} > \Delta\nu_{OPO}$, any signal radiation generated in the OPO part of the crystal (i.e., within $\Delta\nu_{OPO}$ around the central frequency) can be mixed efficiently with the pump radiation to the visible output (assuming optimal phase matching for the central frequencies). Therefore, any parametric noise, i.e., signal radiation not resonant with the bow-tie resonator, will be converted to 606 nm and cause a weak background with $\Delta\nu \approx 100\,\mathrm{GHz}$ spectral width. Note that in contrast to previous work [43, 70], the SFG section precedes the OPO section. Due to the resonator for the signal radiation, this does not impede the operation of the SFG. According to [71, 72], this order enhances the stability of the system. However, we did not find a significant difference between the two configurations.

To stabilize the central wavelength of the OPO-SFG system, we use a homemade Pound-Drever-Hall (PDH) stabilization unit [73, 74]. We employ the error signal to steer the pump wavelength via a piezo control input of the fiber seed laser. We apply a commercial locking device[4] to implement the error signal generation and the proportional-integral-derivative (PID) controller. The locked laser system typically has a linewidth of about 50 kHz (standard deviation, measured with a commercial device[5]) on a timescale of 100 ms and the output power is $P_0 \approx 600\,\mathrm{mW}$ for $P_p = 13.5\,\mathrm{W}$ pumping power. We transfer the light to the experiment via a single mode fiber.

[4] DigiLock 110, Toptica Photonics

[5] EagleEye, Sirah

2.1.2 EIT Light Storage Setup

Figure 2.2 depicts the probe and control beams for EIT as well as the electrical setup required for prolongation of the storage time. After coupling the light out of the single mode fiber, it has a power of up to 500 mW. To counteract power fluctuations, we use an actively controlled[6] feedback loop to drive[7] an acousto-optical modulator[8] (AOM) such that the undiffracted (i.e., zeroth order) beam has a constant power which is monitored by a photodiode[9] (PD). We then split the beam into two beamlines and modulate each beam in frequency and power by an AOM[10] set up in a cat's eye double pass configuration [75]. This setup allows for modulation of the frequency by 160 ± 40 MHz. We use the beams as the probe and control beams for EIT. Their maximal power is 500 µW and 150 mW, respectively, which typically enables Rabi frequencies of up to $\Omega_p = 2\pi \times 70$ kHz and $\Omega_c = 2\pi \times 380$ kHz (note that the Rabi frequencies also depend on the dipole moment of the chosen transition).

To obtain the RF signals driving the AOMs for the probe and control beams, we use two different direct digital synthesis drivers[11,12]. For the driver of the control beam AOM, the amplitude and frequency are set by a digital signal provided by an I/O card[13]. This enables the generation of preprogrammed frequency and amplitude sequences. For the probe beam AOM driver, the frequency is digitally programmed in advance and the amplitude is modulated by an analog signal generated by a waveform generator[14]. This allows for generation of our typical probe pulses with duration of several microseconds. To vary the timing of the probe pulse, we use a digital delay generator[15] (not shown).

The probe beam can be attenuated by neutral density[16] (ND) filters to the level of coherent pulses and is spatially filtered before entering the multipass storage setup (highlighted by the green box). Within the storage setup, we first focus the probe beam by a lens with $f = 150$ mm focal length to a focus with $155 \times 135\,\mu m^2$ (width × height, FWHM) cross section. The focus is centered in the $5 \times 5 \times 3\,mm^3$ large Pr:YSO crystal[17] with 0.05% dopant concentration which we cool to temperatures below 4 K employing a continuous flow cryostat[18]. The crystal's axes (as defined in [76]) are aligned such that the probe beam's polarization is along the D_2 axis (which gives maximal OD) and the propagation axis (z-axis) coincides with the b-axis. A second lens with $f = 150$ mm collimates the probe beam again.

Using high reflective prisms and mirrors, we set up a multipass geometry in which we guide the probe beam around the cryostat and focus it again into the crystal. A similar setup was used in previous work [35] and we refer to this thesis for a more detailed description. In short, the optical path around the cryostat, i.e., back to the entrance window, contains a 4f imaging system to avoid deterioration of the spatial probe pulse profile. By shifting mirror M_D, we can select how many passes N the probe beam makes through the crystal.

To ensure interferometric stability despite the rather long optical path of 1.2 m

[6] PID 100, Toptica Photonics
[7] AA.MOD.80.B46, AA Opto-Electronic
[8] AOMO 3080-125, Crystal Technology
[9] PDA10A-EC, Thorlabs
[10] BRI-TEF-80-50-.606, Brimrose
[11] AODS 20160-1, Crystal Technology
[12] DDSPA-B8b23b-0, AA Opto-Electronic
[13] PCIe-6535, National Instruments
[14] 33220A, Agilent Technologies
[15] DG535, Stanford Research Systems
[16] NExxA-A series, Thorlabs
[17] Scientific Materials
[18] ST-100, Janis

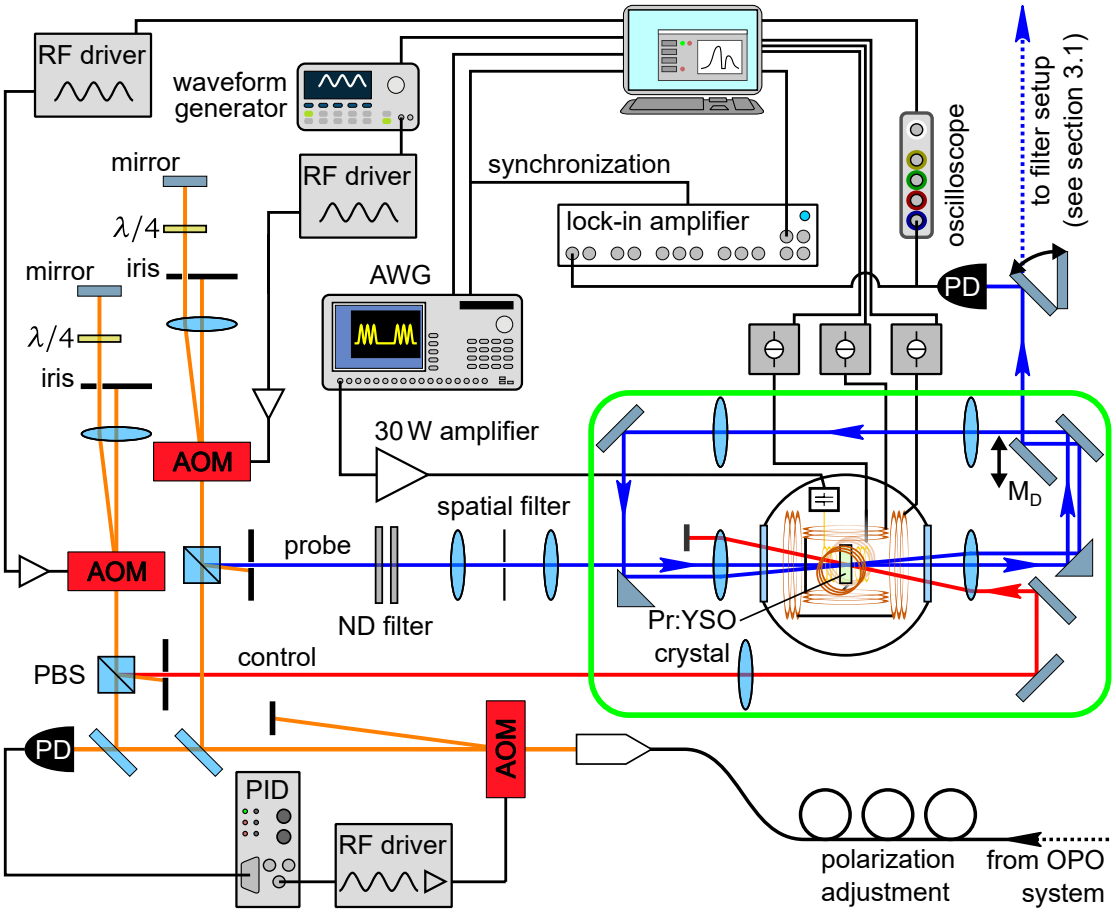

Figure 2.2: Scheme of the optical setup for EIT light storage. The thick black line on the bottom right depicts the fiber coming from the OPO laser system, the colored lines represent free-space beams and thin black lines are electrical connections. In the green box we show the ring-type multipass setup for the probe beam (blue) and the cryostat containing the Pr:YSO crystal and the coil system (brown, described in Section 2.2). AOM: acousto-optical modulator, AWG: arbitrary waveform generator, $\lambda/4$: quarter-wave plate, ND: neutral density filter, PBS: polarizing beamsplitter, PD: photodiode, PID: proportional-integral-derivative controller

per pass, we use stable optical mounts[19] and enclose the optical table with sound absorbing foam[20]. The transmission of one round trip of the probe beam is about $\mathcal{T} = 85\%$ and mainly limited by the transmission of the Pr:YSO crystal despite its anti-reflection coating. The control beam passes the crystal only once. Its propagation direction is opposite to the probe beam and it intersects the first pass of the probe beam under an angle of about 1°. This arrangement ensures a low coupling of stray light from the control pulses into the probe path (i.e., also the signal path due to the forward readout configuration). In combination with a single mode fiber, which is part of the filer setup presented in Section 3.1, the crosstalk from the control beam into the probe beam path is as low as ~ -80 dB [77]. In the crystal, the control beam is collimated and has a cross section of $625 \times 355\,\mu m^2$ (width × height, FWHM). The large elliptical shape ensures equally high control intensity within the profile of the

[19] PLS-Pxxx/M series, Thorlabs
[20] Basotect, BASF

probe passes. Since a constant intensity is beneficial for optical pumping as well, we also use the control beam path for preparation of the Pr:YSO crystal.

For detection of the signal, we use a PD[21] or a single photon detector after the filter setup (presented in Section 3.1. The electrical signal of the PD is either measured by an oscilloscope[22] or, for Raman heterodyne measurements [78, 79] (including spin echo experiments, see Section 4.1), by a lock-in amplifier[23]. We measure the demodulated lock-in amplifier signal by an I/O card[24] that also provides the trigger signals for the external devices.

2.2 Magnetic Field Setup

In order to achieve long coherence times, we use ZEFOZ and DD. ZEFOZ requires a precisely controllable static magnetic field in three dimensions and DD requires a complex sequence of RF pulses. In this section, we present the experimental setup of the coils and electrical driving circuits applied for these purposes.

2.2.1 Generation of Static Magnetic Fields

The relevant ZEFOZ point occurs at a magnetic field of $|\vec{B}_0| = 424\,\mathrm{G}$. To generate this field, we use three pairs of superconducting Helmholtz coils around the Pr:YSO crystal. This setup was developed in previous work and we refer to [18] for a more detailed description.

Figure 2.3 shows a photograph of the system during assembly and Figure 2.4 illustrates the setup in an exploded view drawing. The coils are made of 0.1 mm thick niobium-titanium alloy wires embedded in a copper matrix and wound on copper mounts. These mounts are gold-plated to avoid an increased thermal contact resistance due to surface oxidation (note that the wires must be cooled to temperatures below 9 K to ensure superconductivity). The coils are nested into each other such that the smallest one generates the field in y-direction, the medium coil in x-direction and the largest one in z-direction (which coincides with the optical axis). The system mount contains holes right next to the Pr:YSO crystal to hold an additional pair of Helmholtz coils for application of RF fields. These coils are described in the following subsection. To provide the currents driving the superconducting coils, we use three identical power amplifiers[25] controlled by analog output channels of an additional I/O card[26]. The system has a resolution

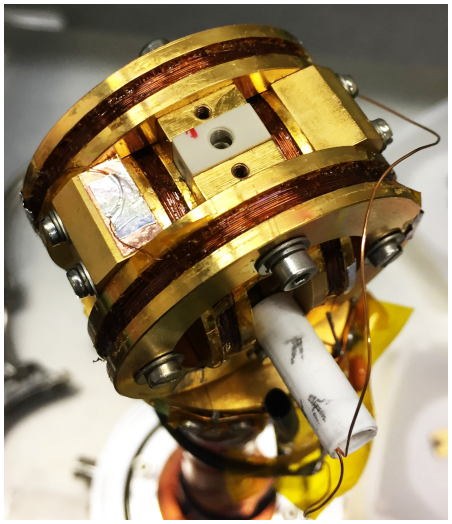

Figure 2.3: Photograph of the coil system in the cryostat during assembly. The white tube on the bottom right contains one of the RF coils (not yet at its final position).

[21] 2051-FS, New Focus
[22] Picoscope 5444B, Pico Technology
[23] HF2LI, Zurich Instruments
[24] PCIe-6363, National Instruments
[25] DCP390/12X, Servowatt
[26] PCIe-6363, National Instruments

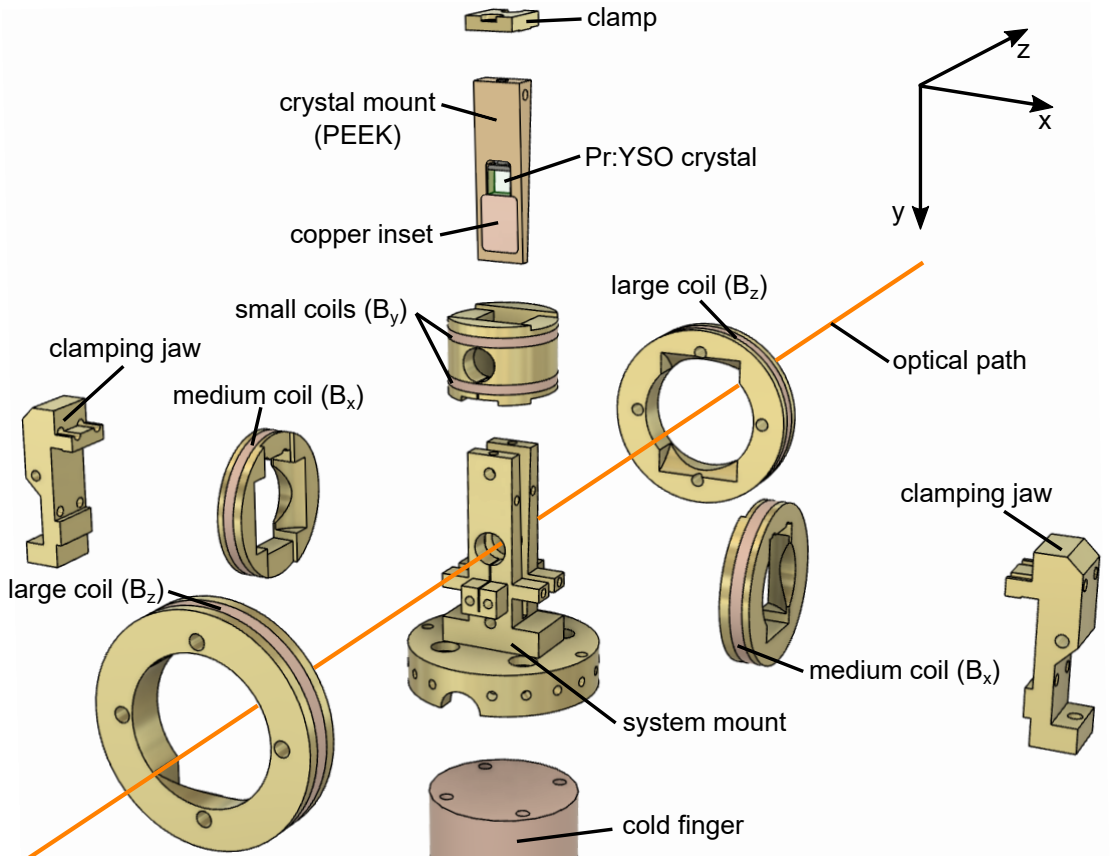

Figure 2.4: Setup of the superconducting Helmholtz coils and crystal mount in the storage cryostat. The system mount is attached to the cryostat's cold finger and holds three pairs of Helmholtz coils. The crystal mount is wedged into the center of the three coil pairs. Figure based on [18].

of $\Delta B_i \approx 90\,\mathrm{mG}$ in each of the magnetic field components. ΔB_i is limited by the resolution of the analogue output channels. Due to the Helmholtz configuration, the magnetic field has a high homogeneity. Within the relevant volume of the crystal (estimated by the size of the control beam), the variation in the field strength is well below 1‰ which is sufficiently low to achieve a coherence time of up to one minute using ZEFOZ [18, 69].

2.2.2 Generation of Homogeneous Magnetic RF Fields

To apply RF rephasing pulses, our setup contains a fourth pair of coils. In order to achieve a high rephasing efficiency, the Rabi frequency of the RF pulses Ω_{RF} must be larger than the inhomogeneous broadening of the ground state $\Gamma_{gnd} \approx 2\pi \times 30\,\mathrm{kHz}$. Therefore, these coils are placed directly next to the Pr:YSO crystal, i.e., in the center of the other three coil pairs, to provide an RF field with high amplitude. Here, however, the RF coils are surrounded by the system mount and other coil mounts which are made of copper to ensure high thermal conductivity. Therefore, RF fields will induce eddy currents which, in turn, lower the field's amplitude and homogeneity (due to the inhomogeneous distribution of copper). To reduce the effect of eddy currents, the system mount and the small coil mount are partially slit. Additionally,

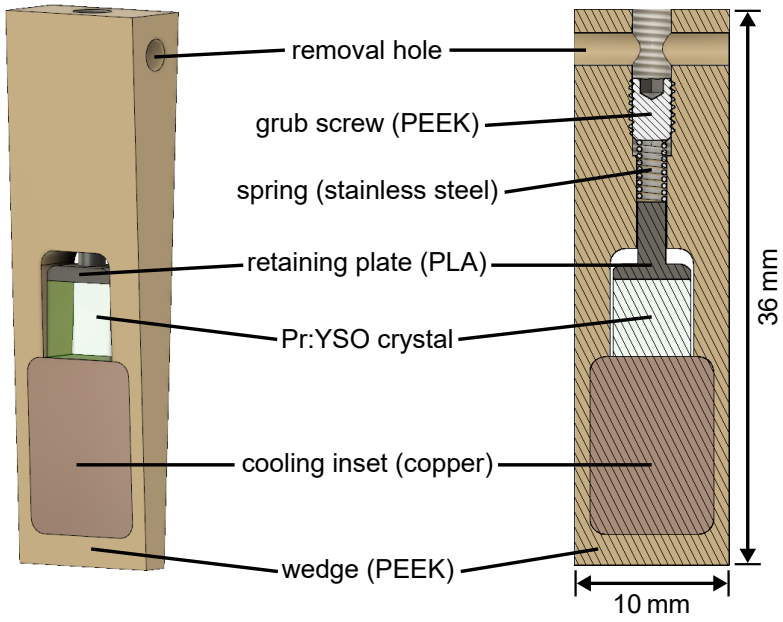

Figure 2.5: PEEK crystal mount with copper inset. The perspective view on the left gives an overview and the sectional view on the right explains the retaining mechanism for the Pr:YSO crystal. The component's materials are given in brackets. PEEK: polyether ether ketone, PLA: polylactide

we developed a new crystal mount to reduce the overall amount of copper in the vicinity of the crystal compared to previous work [18].

Crystal Mount for Reduced Eddy Currents

Figure 2.5 shows the design of this crystal mount and Figure 2.6 a photograph of the mount with a Pr:YSO crystal. The outline of the crystal mount is a wedge, designed to match the intake of the system mount. However, in contrast to the previous design [18], we chose polyether ether ketone (PEEK) as the main material. PEEK is a plastic with high mechanical robustness and vacuum compatibility. It is not electrically conductive and therefore ideally suited for construction of the crystal mount with reduced eddy currents. We put the Pr:YSO crystal on an inset made of copper to ensure proper thermal contact to the system mount. The copper inset is slightly thicker than the PEEK wedge such that it makes better contact to the system mount.

To ensure sufficient pressure between the crystal and the copper inset, we use a spring. This construction automatically compensates for different thermal contraction of the different materials during cooldown of the whole system. As there are no plastic springs commercially available with the small dimension required for our system (note the small spring diameter of 2 mm), we use a spring made of stainless steel. While this material is electrically conductive, it exhibits only very little ferromagnetism leaving the static magnetic field unaffected. To lower the effect of eddy currents induced in the spring, we use a retaining plate to increase the distance between the spring and the Pr:YSO crystal. Furthermore, this plate spreads the pressure induced by the spring over the whole surface of the crystal leading to a uniform pressure distribution. The retaining plate is 3D printed[27] from polylactide (PLA) plastic.

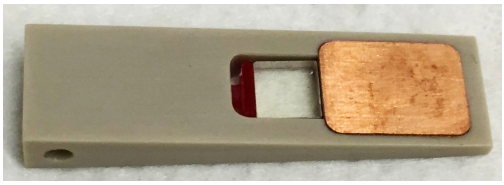

Figure 2.6: Photograph of the crystal mount with an installed Pr:YSO crystal.

[27] Adventurer 3, Flashforge

RF Coil Setup

To obtain a homogeneous RF magnetic field in the Pr:YSO crystal, the RF coils should obey the Helmholtz configuration, i.e., their radius should equal their distance. However, the system mount can hold only coils of up to 3.5 mm radius. As this includes a mount for the coils and since the crystal has a length of 3 mm (limiting the coils' separation), we have to deviate slightly from the Helmholtz configuration. We use a simulation software [80] to optimize the coil design. To simplify the simulation, we assume rotational symmetry around the optical axis. However, with this assumption, we cannot include the asymmetric distribution of copper, i.e., the static magnetic field setup. To mimic the effect of eddy currents induced in this coil system, we include surrounding copper in the simulation. The distance of this copper to the Pr:YSO crystal corresponds to the mount of the smallest ZEFOZ coil. The optimization objective is a homogeneous magnetic field along the optical axis and a high average field strength. Experimentally, we found that the homogeneity is more important for high rephasing efficiency than the average field strength. We explain this by averaging of different Rabi frequencies in the case of an inhomogeneous field. The averaging outweighs the advantage of higher (mean) Rabi frequency (which is due to a spectrally broader interaction, see Section 5.1). Therefore, we focus on generating a homogeneous field.

Figure 2.7(a) shows a sectional view of the coil mounts. Each mount consists of two tubes which are plugged into each other and aligned concentrically to the optical axis. In each of the mounts, the coil (pink, hatched rectangles) is wound into a groove on the end of the inner tube (yellow, hatched rectangles). Each coil is made of copper wire with 0.34 mm diameter (including insulation) and has two layers with a total of 18 turns. The two-layer design enables a smaller mean distance between the coils (7 mm) and reduces the coil's mean radius (2.7 mm) only slightly compared to a single layer design, i.e., it brings the design closer to the Helmholtz configuration. At the same time, it enables electrical access from one side which is required because the crystal blocks the other side. The two coils are connected by a wire which goes around the static magnetic field setup (see Figure 2.3). We plug the inner tubes with the coils into outer tubes (red, hatched rectangles) that fit into the system mount and protect the coils from mechanical damage during the assembly process (note that the insulator is only a thin layer of lacquer which is sensitive to scratches). To reduce the production time, we 3D print the coil mount from PLA. In Figure 2.3 we show one RF coil mount (white tube) during assembly of the coil system.

Figure 2.7(b) shows the simulated magnetic flux density (color scale) and the field lines in a cross section of the coils and the crystal. The optical axis coincides with the z-axis of the plot and is the symmetry axis of the rotational symmetry. We assume a sinusoidal current with 1 A peak value and 10 MHz frequency. In the crystal (central rectangle), the field has its highest homogeneity. Within the surrounding copper (rectangles on the sides) there is no field at all which is due to the induced eddy currents. To quantify the remaining inhomogeneity, we consider the flux density along the optical axis [Figure 2.7(c)]. In the Pr:YSO crystal (light green shaded area), the flux density varies from +23% to −13% of its mean value. This significant inhomogeneity will limit efficient interaction of the RF field with the crystal due to averaging effects along the propagation axis.

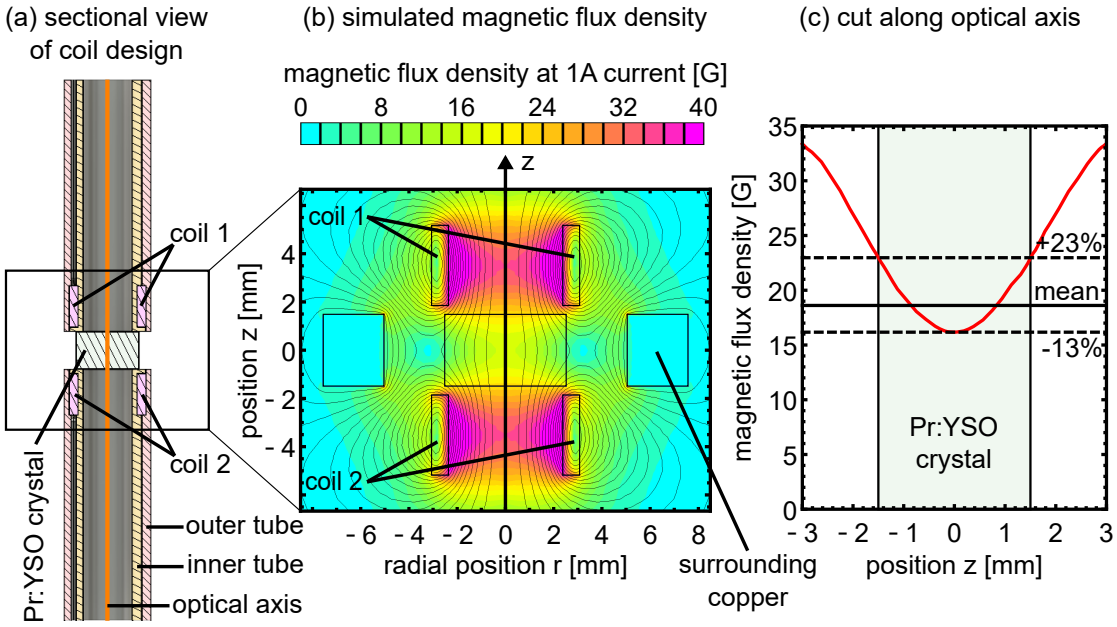

Figure 2.7: Design of the RF coils. (a) Sectional view of the coil mount. The coils are wound on the end of two (inner) tubes and mechanically protected by outer tubes. (b)–(c) Simulated peak magnetic flux density for a sinusoidal current with 10 MHz frequency and 1 A peak current. The simulation considers eddy currents induced in surrounding copper. (b) Density plot of the flux density (color scale) in the vicinity of the coils. The central rectangle represents the Pr:YSO crystal. (c) Magnetic flux density along the optical axis (z-axis).

The inhomogeneity is partially (by about 25%) due to the surrounding copper and mainly due to the deviation from the Helmholtz configuration, i.e., the elongated cross section of the coils and their distance being larger than the radius. However, due to the limitations given by the system mount, it is not possible to design significantly better coils (generating fields with higher homogeneity) unless we allow the mean flux density to be significantly lower. A Helmholtz configuration would be possible with two single turn coils. However, in this configuration the mean flux density would be reduced by a factor of 10 compared to the current design.

Electrical Circuit to Drive RF Currents

In our setup, the RF pulses are generated by an arbitrary waveform generator[28] (AWG) and amplified by an RF amplifier[29]. The AWG is also used as a main frequency reference for the lock-in amplifier as well as for synchronization of the RF and optical sequences (see Figure 2.2). In order to drive an alternating current in a mainly inductive load (i.e., the RF coils), the impedance of the load has to be matched to the output impedance of the amplifier, i.e., 50 Ω. To achieve this, we apply the impedance matching circuit shown in Figure 2.8. The idea of the matching circuit is to add capacitors in parallel (C_p) and in series (C_s) to the RF coil such that the resulting circuit represents a resonance circuit. At the resonance frequency, the current in the RF coil is enhanced which leads to a higher magnetic field and bigger losses in the resistance R of the coils. If the enhancement is chosen correctly, the effective

[28] AWG5014, Tektronix

[29] LZY-22+, Mini-Circuits

resistance of the resonance circuit matches the impedance of the transmission line which is equal to the amplifier's output impedance. To match the enhancement and the resonance frequency, the values of C_p and C_s must be chosen correctly. In contrast to previous work [18], we put the impedance matching circuit directly across the RF coil, i.e., into the cryostat. This is necessary due to the changed RF coils which have a ten times higher inductance L. When we put the matching circuit outside of the cryostat, the wires between the coils and the matching circuit have such a big parasitic capacitance that optimal matching cannot be achieved. We use capacitors with high temperature stability[30] to ensure little deterioration at cryogenic temperatures (however, we operate at 4 K which is well below the specified lowest operating temperature of −55°C). We use a network analyzer[31] to measure the reflected electrical power at different frequencies and optimize C_p and C_s for minimal reflection, i.e., optimal impedance matching. We find the values $C_p = 263\,\text{pF}$ and $C_s = 50\,\text{pF}$ for impedance matching at a resonance frequency $\nu_{RF} = 7.27\,\text{MHz}$ which is the transition frequency at the ZEFOZ point that we use in this thesis. The bandwidth of the matched circuit is $\sim 200\,\text{kHz}$ (FWHM) and therefore allows some tunability of the RF frequency and switching times of $\sim 5\,\mu\text{s}$ (setting a lower limit to the pulse duration).

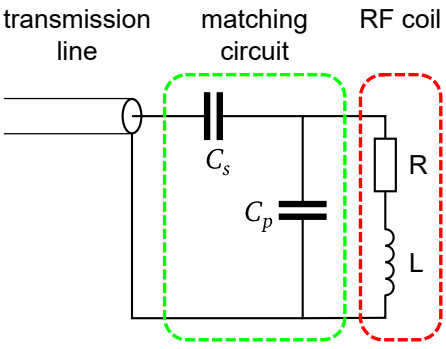

Figure 2.8: Circuit for matching the impedance of an inductive load to a transmission line.

2.3 Implementation of EIT Light Storage in Pr:YSO

In order to observe EIT in Pr:YSO, we need to prepare the population of the relevant states. In this section, we explain the principles of this preparation (for Pr:YSO at zero magnetic field), present the general sequence of our experiments and show the signals of an EIT light storage experiment.

2.3.1 Optical Preparation for Light Storage at Zero Magnetic Field

Due to the large inhomogeneous broadening (i.e., larger than the splitting of the relevant levels) of the optical transition of Pr:YSO, individual transitions cannot be driven directly, i.e., without preparation. A single frequency laser couples all possible transitions at the same time, though in different ions within the inhomogeneous line. Ions in which the laser drives the same transition are classified as an ensemble. In thermal equilibrium, i.e., without a preparation, the three ground states are equally populated in all ensembles. In order to enable coupling of the laser to a specific transition in a single ensemble at the frequency ν, we must ensure zero population of the states which are also coupled at ν in other ensembles. Due to the long population lifetime of the ground states (compared to the excited states), optical pumping can be used to create such a non-thermal population distribution.

[30] 561R series, Vishay Intertechnology

[31] miniVNA, mini Radio Solutions

The general idea of the optical pumping sequence used in this work is to first prepare a spectral region without any absorption, called a spectral pit and then prepare isolated absorption peaks in this pit that correspond to single transitions. This scheme was first applied in the closely related REIDS Eu^{3+}:Y_2SiO_5 [81] and then adapted to Pr:YSO [82]. We use a variant of the preparation scheme presented in [82] to enable EIT in Pr:YSO at zero magnetic field. Note that at the ZEFOZ point (i.e., at nonzero magnetic field), the level structure is more complicated and we use a different preparation sequence (presented in Section 4.2).

Figure 2.9 summarizes our preparation scheme. For ease of presentation, we consider only a single excited state. However, the preparation scheme works for any of the three excited states of Pr:YSO. Therefore, the presented preparation sequence actually prepares three ensembles at the same time and the ensembles differ only by the excited state.

We start the preparation by preparing a 16 MHz wide spectral pit by applying ten pumping pulses, each with a duration of 20 ms. Each pulse is chirped from $\nu = -12$ MHz to $\nu = 4$ MHz (ν denotes a relative frequency, i.e., the frequency difference to the probe transition). In the target ensemble, i.e., the ensemble in which we aim to perform EIT, each of these chirped pulses excites the population of the upper two ground states to the excited state [Figure 2.9(a)]. Due to spontaneous decay, the population then redistributes among all three ground states (according to the transition moments). Via repeating the excitation out of the upper ground states (by the ten repetitions of the pumping pulse), the population accumulates in the lowest ground state. In other ensembles the population might be prepared in other ground states. However, in all ensembles the population is prepared such that it does not cause any absorption within the pumped spectral region, i.e., the spectral pit. Figure 2.9(e) shows the fully transparent spectral pit in the measured spectrum (green graph).

In order to obtain an isolated absorption peak, we apply a 5 ms long single fre-

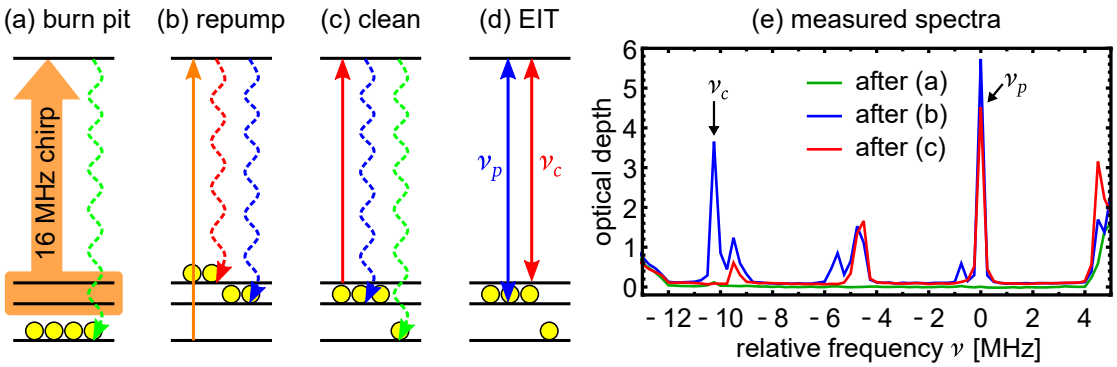

Figure 2.9: Preparation scheme for EIT in Pr:YSO at zero magnetic field. (a)–(c) Optical pumping pulses (orange and red arrows) redistribute the population. Yellow disks indicate the population after the respective pumping step. (a) We prepare a spectral pit by chirping a pumping pulse over a 16 MHz wide frequency range. (b) A repumping pulse prepares isolated absorption peaks in the pit. (c) The cleaning pulse clears absorption at the control frequency ν_c (d) In the prepared medium, EIT can be performed in a Λ-configuration. (e) Absorption spectra measured after the different preparation steps: OD versus frequency (relative to the probe frequency ν_p).

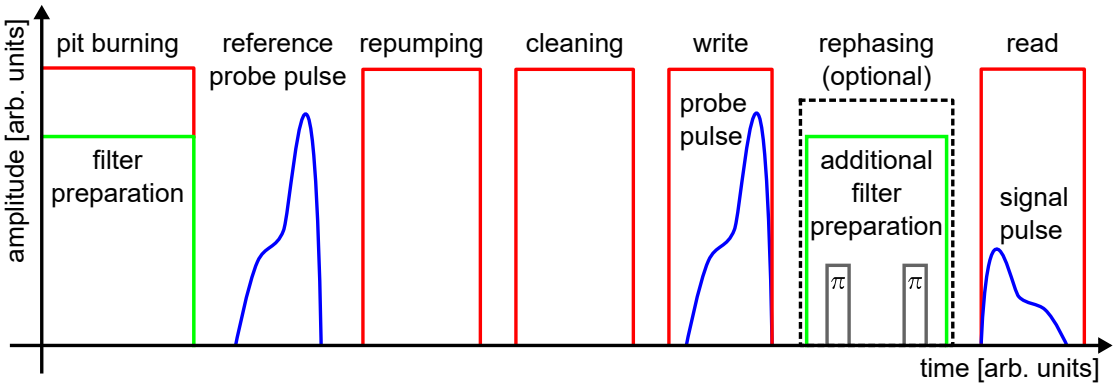

Figure 2.10: Sequence of EIT light storage experiments in Pr:YSO. We show schematically the amplitude in the different beam paths and the RF field versus time. The additional filter preparation is only performed if the storage time exceeds 1 s. Colors represent the beam path. Red: control path, blue: probe path, green: filter preparation path (see Figure 3.1)

quency pulse with 500 µW power, called the repumping pulse. This pulse excites the previously shelved population out of the lowest ground state such that it redistributes among the upper ground states [Figure 2.9(b)]. In the absorption spectrum [blue graph in Figure 2.9(e)], this leads to two distinct peaks at the probe and control frequencies $\nu_p = 0$ MHz and $\nu_c = -10.2$ MHz. The probe peak has an OD of about OD ≈ 5.5 which allows for storage efficiencies of up to 31% (see Section 1.1). The additional (lower) absorption peaks are due to repumping and absorption via other excited states which are not considered in Figure 2.9(a)–(c).

In the last preparation step, we apply four cleaning pulses with 2 mW power on the control transition to remove the population from the highest ground state, i.e., to provide full transmission at ν_c [Figure 2.9(c)]. The cleaning pulses are 5 ms long and chirped over 800 kHz around ν_c to ensure no absorption even for spectrally broadened control pulses (which might be due to the Fourier spectrum of the steep slopes when switching the pulses). The medium is now prepared for EIT in a Λ-type coupling scheme [see Figure 2.9(d)], i.e., all absorption at ν_p stems from one transition in the target ensemble and the medium is fully transparent at the corresponding control frequency ν_c [see red graph in Figure 2.9(e)]. We note again that the preparation described above prepares three ensembles simultaneously for EIT (with coupling to different excited states). Compared to preparation of a single ensemble (which is possible by changing the repumping frequency) this increases the OD and enables higher storage efficiency [37].

We summarize the sequence of our light storage experiments in Figure 2.10. First, we prepare the Pr:YSO crystal as described above and then we apply the control write and read pulses for storage and readout. As a reference for the efficiency calculation, we measure an additional probe pulse right before the repumping pulse, i.e., when the medium is fully transparent. To prolong the storage time, we can apply a rephasing sequence after the control write pulse. For storage of weak coherent pulses (see Chapters 3 and 6), we prepare the spectral filter during the pit burning step and, if the storage time is long enough to accommodate the filter preparation, in parallel to the rephasing sequence.

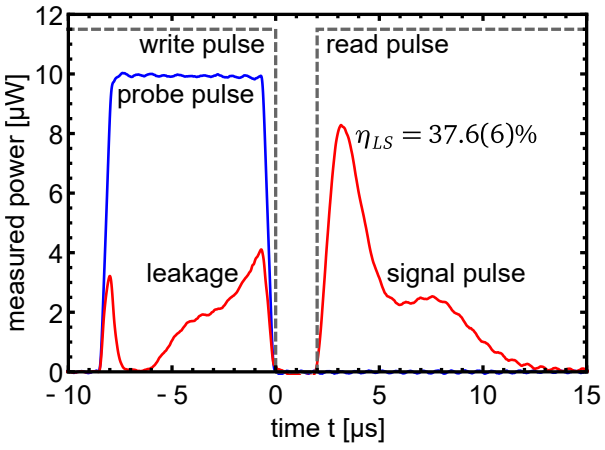

Figure 2.11: Optical power versus time for an EIT light storage experiment at zero magnetic field. The probe pulse (blue, measured reference pulse) is stored and read using the control write and read pulses (dashed, gray lines, not to scale). The red graph shows the power during the storage experiment. Upon storage ($t \leq 0\,\mu s$), a part of the probe pulse leaks through the Pr:YSO crystal and reaches the PD (leakage). After $t_s = 2\,\mu s$ storage time, the control read pulse retrieves the signal pulse. The efficiency is $\eta_{LS} = (37.6 \pm 0.6)\%$.

2.3.2 EIT Light Storage at Zero Magnetic Field

We apply the optical sequence described above to store a probe pulse with $\tau_p = 8\,\mu s$ duration. We use a control pulse power of $P_c = 15\,mW$, corresponding to a Rabi frequency of $\Omega_c \approx 135\,kHz$. Both τ_p and Ω_c were optimized for maximal efficiency (given the rectangular probe pulse shape). Figure 2.11 shows the pulses involved in the storage experiment. The dashed, gray lines indicate the timing of the control write and read pulses. In parallel to the control write pulse, we emit the probe pulse. A part of the probe pulse, called leakage, leaves the Pr:YSO crystal. At $t = 0\,\mu s$ we turn off the control write pulse, i.e., store the portion of the probe pulse which is still in the crystal. The control read pulse starts after a storage time of $t_s = 2\,\mu s$ and retrieves the signal pulse. By dividing the energy of the signal pulse by the probe pulse energy (determined by integration of the power), we calculate the storage efficiency of $\eta_{LS} = (37.6 \pm 0.6)\%$. This is higher than expected value of $\eta_{LS} = 31\%$ for the prepared absorption peak with OD ≈ 5.5. We explain the deviation to be due to an underestimation of the OD in the spectroscopy (compare Section 6.1) and the effect of an inhomogeneously broadened absorption peak (see Section 5.2).

In this chapter, we presented the experimental setup for EIT light storage in Pr:YSO. We described the OPO and SFG based laser system generating coherent light at a wavelength of 606 nm. We discussed the coil setup for generating static magnetic fields up to several hundred gauss with 90 mG resolution. At the ZEFOZ field, the variation in field strength is well below 1‰. Furthermore, we presented the crystal holder and RF coil setup for generation of RF fields with less than $\sim 25\%$ inhomogeneity. Finally, we demonstrated EIT light storage of a classical pulse for a short storage time of $t_s = 2\,\mu s$ with an efficiency of 38%.

Chapter 3

Storage of Weak Pulses at Short Times

In the previous chapter, we presented light storage of classical probe pulses with energies in the range of 100 pJ, i.e., with $\sim 3 \times 10^8$ photons. In this chapter, we focus on storage of weak coherent pulses. Thus, the suppression of background noise becomes more important. In the EIT protocol, the control read pulse is the major contribution to the background signal. With the typical control read pulse power $P_c \approx 15$ mW and signal pulse duration $\tau_p \approx 10\,\mu$s, we calculate that we must filter out $\sim 5 \times 10^{11}$ control read pulse photons. We chose a setup with counterpropagating control and probe beamlines to prevent a coupling of control light into the probe beamline. Furthermore, we use a single-mode (SM) fiber in front of the SPCM to enhance the spatial suppression of the background and achieve a total suppression of ~ 80 dB. This matches our observation that for storage of $\sim 10^4$ photons with $\sim 10\%$ efficiency, the control read pulse background becomes significant (see [77]). Therefore, we need an additional suppression of ~ 40 dB for storage of weak coherent pulses at the single photon level with a signal to noise ratio (SNR) around 1.

In this chapter, we describe the setup of a narrowband spectral filter, implemented in an optically prepared Pr:YSO crystal, and explore the limitations for storage of weak coherent pulses on a short, i.e., microsecond, timescale. Dephasing is negligible at this timescale and we do not require rephasing or ZEFOZ. The concept of exploiting optical pumping for a spectral filter has previously been implemented in REIDS, also in the context of quantum memories, and a separation of up to 60 dB has been achieved [83–85]. We implement the concept for the first time to suppress the control read pulse background of an EIT driven memory and achieve EIT light storage on the single photon level which was previously only accomplished in gaseous media. This result is part of a manuscript that we prepared for publication.

We note that in the experiments described in this chapter, the fiber seed laser[1] differs from the one described in Section 2.1 which results in an increased optical linewidth of about 100 kHz on a timescale of 100 ms.

3.1 Filtering Optical Background

Since the read and signal pulses have the same polarization and coincide temporally, the frequency is the only remaining criterion to distinguish between them. Therefore, we apply a spectral filter which we present in this section.

3.1.1 Optical Filter Setup

The spectral filter must increase the separation of the control read and the signal pulse by at least 40 dB. In our storage medium Pr:YSO, the frequency difference

[1] Koheras AdjustiK Y10 PM PztM, NKT Photonics

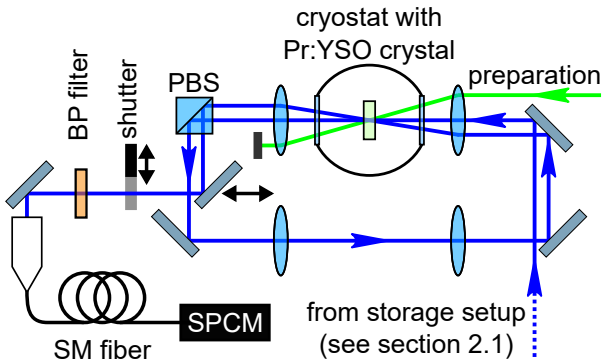

Figure 3.1: Setup of the spectral filter. The signal (blue) passes a Pr:YSO crystal (faint green) which we prepare using a separate beam (green). We can utilize a ring-type multipass setup to increase the absorption. BP: bandpass, PBS: polarizing beamsplitter, SM: single-mode, SPCM: single photon counting module

between the read and signal pulse is only 10.2 MHz if we apply no magnetic field and 7.3 MHz at the ZEFOZ point. Dispersive elements cannot reach such a high frequency resolution. A high-finesse Fabry-Perot cavity as an interferometric spectral filter might achieve the goal, but is technically challenging. Therefore, we use a second Pr:YSO crystal (filter crystal) as a programmable bandpass filter, prepared by an appropriate optical pumping sequence.

Figure 3.1 depicts the setup. We place the filter crystal in a cryostat[2] and prepare it using an additional beam. This preparation beam is derived from the OPO system and modulated by an AOM[3] double pass setup analog to the probe and control beams (not shown in Figure 2.2). The AOM driver[4] can be programmed with an appropriate preparation sequence (described in the following subsection) and is synchronized with the storage sequence. In the filter setup, the signal passes the filter crystal and its polarization is filtered by a polarizing beamsplitter[5] (PBS). The PBS reflects the signal onto the intended path and transmits light with rotated polarization. This increases the suppression of control read pulse photons because of a partial rotation of their polarization in the filter crystal. This rotation is due to the birefringence of Pr:YSO and the specific alignment of the transition dipole moment [86]. Since the signal photons pass through a transmissive part of the filter spectrum, their polarization remains unchanged. In previous work, we found that a polarization filter increases the suppression of read photons by about a factor of 3.5 [77].

In the filter crystal, the signal beam is collimated with a diameter of $130 \times 125\,\mu m^2$ (width × height, FWHM). The collimated beam path reduces the solid angle in which signal photons can be detected. Since fluorescence (which might be caused by the absorbed control read pulse) is emitted isotropically, a detection path covering only a small solid angle reduces the number of detected fluorescence photons. The preparation beam has a diameter of $960 \times 730\,\mu m^2$ (width × height, FWHM) in the filter crystal and is collimated as well to ensure a uniform preparation. We typically apply 1 mW optical power for the preparation which corresponds to a Rabi frequency in the range of $2\pi \times 20$ kHz, i.e., less than the linewidth of the laser system.

By shifting a mirror, we can select to let the signal pass the filter again to increase the absorption (using a ring-type multipass setup analog to the storage setup) or to guide it directly through a shutter[6] and a bandpass (BP) filter[7] to the detector. We note that in the experiments presented in this chapter, i.e., at zero magnetic

[2] ST-100, Janis
[3] BRI-TEF-80-50-.606, Brimrose
[4] Model 409b, Novatech Instruments
[5] PBS101, Thorlabs
[6] homemade, based on [87]
[7] #65-103, Edmund Optics

field, we do not use the filter in a multipass yet. We apply it only for storage at the ZEFOZ point where the efficiency, and hence the SNR, are reduced (see Chapter 6). The shutter blocks the beam during the preparation sequence of the filter crystal to protect the detector from saturation and the BP filter blocks light with wavelengths outside its 10 nm wide transmission window (FWHM). By rotating the filter away from normal incidence, we tune its transmission window such that its top end lies at 606 nm to block fluorescence at higher wavelengths (compare Section 1.2). Finally, we couple the signal into a SM fiber[8] to enhance spatial filtering and guide the signal to a single photon counting module[9] (SPCM). The electrical pulses (one for each detected photon) are processed by our oscilloscope and time binned in software.

The filter setup has a transmission of $\mathcal{T}_f = (40.9 \pm 0.8)\%$ for $N_f = 1$ pass of the filter crystal and $\mathcal{T}_f = (19.1 \pm 0.7)\%$ for $N_f = 2$ passes. Considering the detector efficiency of $\sim 66\%$, this means that for $N_f = 1$ ($N_f = 2$) we will detect about 27% (13%) of all signal photons leaving the storage setup.

3.1.2 Preparation of the Filter Crystal

In order to use Pr:YSO as a filter crystal, the desired absorption spectrum must be prepared by optical pumping. Without preparation, i.e., in thermal equilibrium, the absorption is constant within the relevant frequency range of ~ 10 MHz. However, an arbitrary non-thermal population distribution can be achieved by applying a suitable sequence of optical pumping pulses. The modified population distribution leads to an altered absorption spectrum. For our spectral filter we require a high absorption at the control frequency ν_c (to suppress the control read pulse) and a high transmission at the probe frequency ν_p (to transmit the signal). In order to obtain high absorption and transmission also in a spectral range around the central frequencies, we prepare spectral bands around ν_c and ν_p by chirping the preparation pulses. This ensures a high absorption even when the read and signal pulses are spectrally broadened, e.g., due to the Fourier limit. These bands are called stopband and passband, respectively.

In Figure 3.2 we show schematically the preparation sequence of the filter crystal designed for EIT light storage in Pr:YSO without a magnetic field. In this case, the relative frequencies (i.e., with respect to the probe transition) $\nu_p = 0$ MHz and $\nu_c = -10.2$ MHz are given by the level scheme shown in Figure 3.2(a). Note that we show only one of the three optically excited states in the level schemes in Figure 3.2 to simplify the figure. For preparation of the stopband, we perform six chirps with 1 MHz width and central frequencies [see straight arrows in Figure 3.2(b)] chosen such that in three ensembles [illustrated by the three level schemes in Figure 3.2(b)] the population is cleared in two of the three ground states (see yellow disks). We note, that in the full level scheme, pumping is performed in nine ensembles (which differ in the excited state from the three ensembles discussed here). However, the preparation does in principle work the same in ensembles that only differ in the excited state. The ensembles are chosen (via the pumping frequencies) such that the third ground state (now holding most of the population) is coupled to the excited state at frequency ν_c. This results in a threefold absorption at ν_c compared to an equal distribution of population, i.e., the unprepared thermal distribution, and represents the stopband.

[8] SM600, Thorlabs

[9] SPCM-780-41-FC, Excelitas Technologies

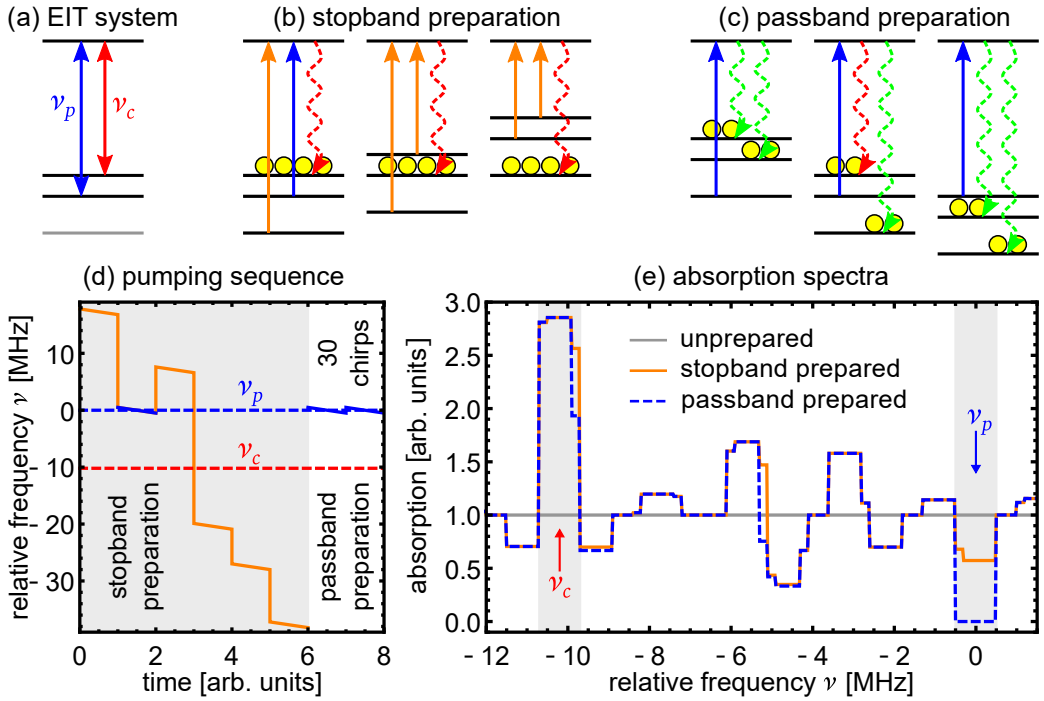

Figure 3.2: Preparation scheme of the filter crystal for EIT light storage without a magnetic field. For simplification, we consider only a single optically excited state in (a) to (c). Yellow disks represent the population distribution after the respective pumping step. (a) EIT coupling scheme. The probe and control pulses (blue and red) couple two ground states (lower black lines) to the same excited state. The gray line indicates the position of the third ground state. (b) Optical pumping (in the filter crystal) at six frequencies prepares the population (yellow disks) in the ground states such that the absorption at ν_c is maximized, i.e., the filter stopband is prepared. (c) Pumping at the probe frequency ν_p pumps the population into other ground states such that the passband is created. (d) Frequency shift of the preparation beam versus time for the preparation of the filter crystal. The frequency shifts of the preparation beam are shown over time. For each optical pumping frequency we perform a 1 MHz wide chirp (see falling slopes at each time step). First, the stopband preparation (orange line with blue section) is performed. Then, we perform 30 chirps with 1 MHz width centered at ν_p to create the passband (blue, solid line at time units 6 to 8). (e) Simulated absorption spectra, i.e., absorption versus frequency, after each preparation step. In the unprepared medium the absorption is 1 for all frequencies (gray line). After the preparation of the stopband (orange graph), an absorption plateau centered at ν_c, i.e., the stopband can be seen (gray shaded area on the left). After the passband preparation (dashed, blue graph), a narrow spectral pit around ν_p is prepared (gray shaded area on the right).

The order of the chirps preparing the stopband has no relevant influence on the resulting absorption spectrum and was chosen arbitrarily.

For preparation of the passband, we perform 30 chirps with 1 MHz width centered at ν_p. The chirps redistribute the population such that no absorption remains within the pumped spectral region [see Figure 3.2(c)]. We choose the high number of chirps due to the importance of a perfectly transparent passband. Any absorption will reduce the number of detected signal photons, lower the SNR and increase the statistical error. Figure 3.2(d) summarizes the preparation sequence for the filter crystal and displays the frequencies of the involved chirps over time. The first six chirps constitute the stopband preparation (gray shaded area) and the passband is

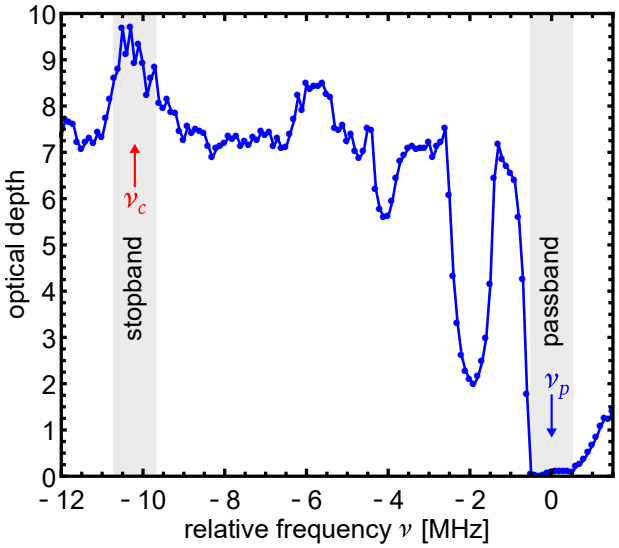

Figure 3.3: Absorption spectrum, i.e., OD versus frequency, of the filter crystal after application of the preparation sequence designed for EIT storage at zero magentic field. The absorption is measured for 40 µs long rectangular probe pulses with 200 pW power. For each frequency we measure the number of transmitted photons summed over 50 repetitions and calculate the OD. To prevent saturation of the SPCM, we use a ND filter with $\mathcal{T} = 5\%$ at frequencies with high transmission. In the stopband around ν_c, the average OD is 8.8 ± 0.1 and in the passband maximal transmission is obtained.

prepared by 30 chirps (only 2 shown).

Pr:YSO has three optically excited states. This makes it complicated to predict the absorption spectrum after a series of pumping pulses. We use a simulation that calculates the redistribution of population for each ensemble after every optical pumping process. Based on the distribution of population we calculate the absorption spectrum. Figure 3.2(e) shows the simulated absorption spectra for the unprepared medium (gray line), after preparation of the stopband (orange graph) and after preparation of the passband (dashed, blue graph). The stopband (gray shaded area on the left) almost reaches maximal absorption, i.e., 3 times the value of the unprepared medium, over the full 1 MHz wide range. The passband (gray shaded area on the right) is fully transparent.

In our experiment we use a 10 mm long Pr:YSO crystal[10] with 0.05% dopant concentration as a filter crystal. We apply five repetitions of the preparation sequence (to ensure optimal pumping) and measure the absorption spectrum. We normalize the transmission by assuming full transmission at the frequency with minimal measured absorption. We note that this might not actually be full transmission, however we estimate that OD < 0.2 in the passband [77]. In contrast to the setup described above, we use a Glan-Thompson prism[11] as a polarization filter instead of the PBS and do not use the BP filter in this measurement.

Figure 3.3 shows the measured absorption spectrum. Comparison to the simulation [dashed, blue line in Figure 3.2(e)] shows a general agreement. Spectral holes and peaks occur at the same frequencies, however in the experiment the structures are washed out. We explain this by different broadening mechanisms of the pumping process, e.g., instantaneous spectral diffusion [88] and power broadening, and the limited spectral resolution of the absorption measurement, e.g., due to the finite length of the probe pulses and the linewidth of the OPO laser system. The relative absorption of the different spectral features differs between the experiment and simulation. In the simulation, the stopband has about 3 times higher absorption than for the surrounding frequencies, however in the experiment, the stopband is far less pronounced. Furthermore, in the simulation the spectral hole at $\nu \approx -4.5$ MHz has

[10] Scientific Materials

[11] GTH5M, Thorlabs

a lower absorption than the hole at $\nu \approx -2.2\,\mathrm{MHz}$ while the situation is reversed in the experiment. We explain both observations by a broad spectral width of the probe pulse which leads to a leaking of photons through the passband at $\nu_p = 0\,\mathrm{MHz}$ thus limiting the maximal achievable absorption. Due to the lower spectral distance, this leaking is more pronounced for the hole at $\nu \approx -2.2\,\mathrm{MHz}$. In Section 6.1 we investigate this effect more closely. Nevertheless, in the 1 MHz wide stopband (gray shaded area on the left), the average OD is 8.8 ± 0.1. This corresponds to a control suppression of 38 dB which almost fulfills the requirement of 40 dB.

So far, we used the probe beam for the absorption measurement. In the experiment, however, the filter must absorb a reflected portion of the control beam. Due to the different size and power, this might alter the absorption. In previous work, we measured the absorption using the control beam path and found a 6 dB lower value than expected from the measurement with the probe beam [77]. It was limited by fluorescence which indicates an optical pumping process in (at least) one of the Pr:YSO crystals. Using the BP filter we were able to block the fluorescence light and obtained a suppression of the control read pulse of 42 dB [77]. According to our estimation this is sufficient for storage of a single photon with SNR > 1.

3.2 Storage of Weak Coherent Pulses for Short Times

We discuss now EIT light storage of a probe pulse attenuated to the few-photon level. We apply control pulses with a power of $P_c = 15\,\mathrm{mW}$, corresponding to a Rabi frequency of $\Omega_c \approx 135\,\mathrm{kHz}$, to store and read a rectangular probe pulse with a duration of 8 µs (see Section 2.3 for storage of a classical probe pulse with these parameters). We optimized these parameters for maximal efficiency. Since the storage time of $t_s = 2\,\mu\mathrm{s}$ is well below T_2^*, we require no rephasing. Figure 3.4 shows the photon counts over time for a probe pulse containing $\bar{n} = 8.4 \pm 0.7$ photons and the corresponding signal pulse as well as a signal pulse for $\bar{n} = 1.1 \pm 0.1$. Even for the latter measurement, i.e., on the single photon level, the signal pulse can clearly be discriminated from the background.

For calculating the storage efficiency η_{LS} and SNR, we must select the time interval for integrating the signal pulse. For a wider interval we integrate a bigger portion

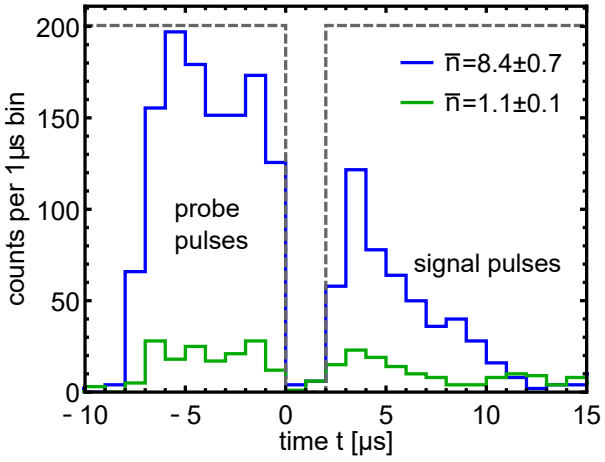

Figure 3.4: Photon counts in 1 µs wide bins versus time for EIT storage of weak coherent pulses with $\bar{n} = 8.4 \pm 0.7$ (blue) and 1.1 ± 0.1 (green) photons. We store the probe pulse (data before $t = 0$) for $t_s = 2\,\mu\mathrm{s}$ using the control write and read pulses (indicated by the gray, dashed line). The signal pulses (data after $t = 2\,\mu\mathrm{s}$) are clearly visible, even for $\bar{n} = 1.1$. We accumulate all data for $\bar{n} = 8.4$ over 500 repetitions and scale them by a factor of 2 to match the measurement for $\bar{n} = 1.1$ (based on 1000 repetitions).

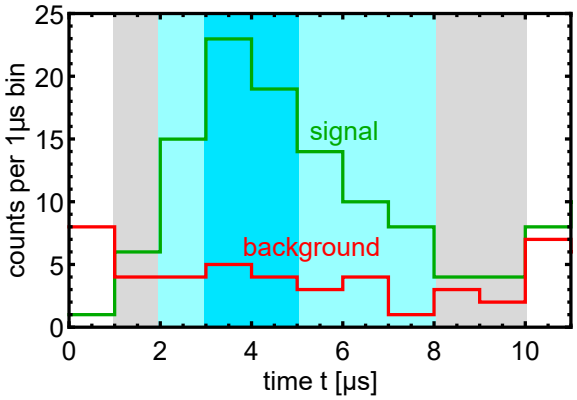

Figure 3.5: Photon counts of signal (green) and background (red) versus time for EIT storage of weak coherent pulses with $\bar{n} = 1.1 \pm 0.1$. The background counts are taken from a later time of the signal measurement (when the signal itself is definitely zero). The gray and blue rectangles indicate different integration gates.

of the signal pulse, hence we get a higher efficiency. However, as more bins are considered, we also accumulate more background counts which reduces the SNR. Therefore, the width of the integration gate has to fulfill a compromise between high η_{LS} and high SNR. In Figure 3.5 we show the photon counts for the measurement with $\bar{n} = 1.1 \pm 0.1$ and the background counts and illustrate three different choices for the integration gate. For the widest gate, we get SNR $= 2.4 \pm 0.6$ and $\eta_{LS} = (45.1 \pm 8.0)\%$. Using the gate with medium width, the efficiency drops only slightly to $\eta_{LS} = (42.0 \pm 7.3)\%$ but the SNR increases more significantly, i.e., to SNR $= 3.2 \pm 0.9$. When we reduce the width of the integration gate further, η_{LS} drops drastically to half of its value, i.e., to $\eta_{LS} = (20.4 \pm 4.7)\%$, but the SNR increases only slightly to 3.7 ± 1.5. This shows that the integration gate with medium width represents a reasonable compromise enabling both a high η_{LS} and SNR. We note, however, that the choice of the integration gate depends strongly on the pulse shape and we optimize it for every experiment.

Using the integration gate with medium width, we showed EIT light storage on the single photon level with SNR $\gtrsim 3$. This is sufficiently large to enable operation as a true quantum memory. The efficiency of $\eta_{LS} = (42.0 \pm 7.3)\%$ could be increased further using the multipass setup which enabled an efficiency of up to 76% for storage of classical light pulses in previous work [35]. In this work, however, we aimed for efficient storage at longer storage times and therefore used the multipass setup only to increase the efficiency under the unfavorable conditions at the ZEFOZ point (see Chapters 5 and 6). Moreover, we note that application of the filter multipass setup is expected to increase the SNR even further. However, in the experiments presented in this thesis, we apply this multipass setup also only for storage of weak coherent pulses at the ZEFOZ point (see Chapter 6). Still, to the best of our knowledge, our result at zero magnetic field represents the first implementation of EIT light storage in a solid state system operating at the single photon level.

In this chapter, we presented the storage of weak coherent pulses with an average of 1.1 photons at a light storage efficiency of 42% via EIT in Pr:YSO. We applied a spectral filter, implemented in a second Pr:YSO crystal, to suppress control read pulse background by 42 dB and achieved a SNR of 3.2. Previous research on few-photon storage via EIT was always realized in atomic gases. Therefore, our result is the first successful implementation of EIT light storage on the single photon level in a solid state medium.

Chapter 4

Light Storage at the ZEFOZ Point

In the experiments presented in this chapter, we employ the ZEFOZ technique in order to proceed toward longer storage times. ZEFOZ was applied in previous work of our team to achieve light storage on the timescale of a minute [18, 19]. In this chapter, we present our characterization of a different ZEFOZ point which was first identified by Longdell *et al.* [64]. Then, we demonstrate the first implementation of light storage at this ZEFOZ point.

4.1 Characterization of the ZEFOZ Point

As discussed in Chapter 1, the prolonged storage time at the ZEFOZ point bases on an enhanced frozen core effect which does not depend on the direction of the magnetic field and on the insensitivity of a transition to changes in the magnetic field [65]. This insensitivity results from an extremum of the transition frequency with respect to the magnetic field and is only achieved at specific fields. Longdell *et al.* found and characterized a ZEFOZ point in PrYSO (labeled "B" in their work) which exhibits a T_2 time of 1.4 s in a spin echo experiment [64].

Although the coherence is created by a different process than in a spin storage experiment (as performed by Longdell *et al.*), we expect the T_2 time to stay roughly the same for EIT light storage [18]. According to a simulation based on the work of Lovrić *et al.* [63], we expect the ZEFOZ point at $\vec{B}_0 = (-77, 169, 381)$ G (in our coordinate system where $x \parallel D_1$, $y \parallel D_2$, and $z \parallel b$, with the crystal axes D_1, D_2, and b, compare Section 2.2). However, due to minor misalignments of the crystal's axes with respect to the Helmholtz coils and imperfect calibration of the magnetic field in relation to the applied current, we expect the setting of $\vec{B}$ to differ slightly in our experiment. Previous work showed that even 1% deviation from the ZEFOZ point can reduce T_2 by an order of magnitude [66, 69]. In order to obtain maximal T_2, we thus optimize $\vec{B}$ prior to every experiment using a gradient descent algorithm [18, 69]. This also allows us to counteract fluctuations of the calibration and background fields happening between different measurement days. We perform the first optimization of $\vec{B}$ using a spin echo experiment as described in [18] because of the simple optical preparation (i.e., no knowledge about the level structure is required). The gradient descent algorithm converges to the magnetic field $\vec{B}_0' = (-72.30, 174.45, 376.52)$ G. The difference in magnetic field to the simulated value $\vec{B}_0$ is only 8.5 G (or 2%) which demonstrates the accuracy of our magnetic field calibration compared to the work of Lovrić *et al.* [63]. We characterize the ZEFOZ point by performing spectroscopy based on Raman heterodyne detection [78, 79] at different $\vec{B}$ in the vicinity of $\vec{B}_0'$. The Raman heterodyne technique allows for probing an RF transition without requiring a complicated preparation sequence (which would in turn require knowledge of the level structure). Therefore, it is ideally suited for measuring the transition frequency

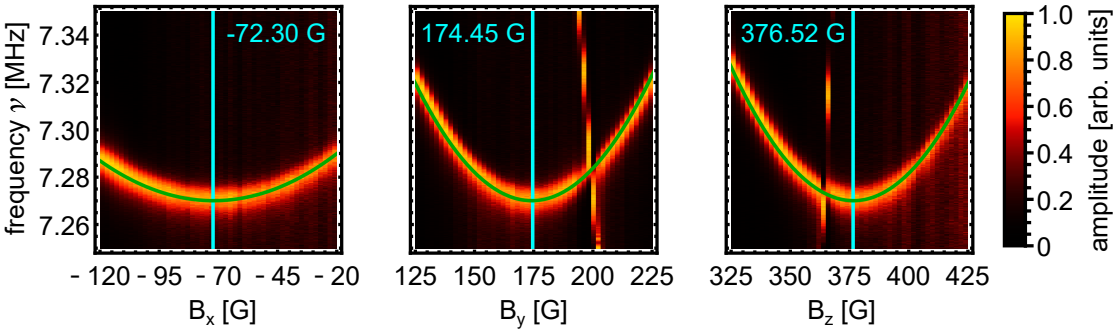

Figure 4.1: Spectra of the ground state transitions measured with Raman heterodyne detection for different magnetic field in the vicinity of the ZEFOZ point. In each plot we vary one of the $\vec{B}$ components (x-axis of the plots) while the others stay fixed at the values given in cyan (in their respective plot). The color scale shows the amplitude of the Raman heterodyne signal indicating a transition at the respective frequency (y-axis). For each column of the spectra (i.e., for each value of $\vec{B}$), we normalize the amplitude of the signal to values between 0 and 1 in order to maintain a high contrast over the whole range of magnetic fields. The green lines show a fit of parabolas to the ZEFOZ transition.

of the ZEFOZ transition under varying external conditions, i.e., for different $\vec{B}$.

Figure 4.1 shows spectra of the ground state transitions (color scale versus y-axis) when we vary one of the three components of $\vec{B}$ around $\vec{B}_0'$ (x-axis), i.e., we keep the respective other two components fixed at $\vec{B}_0'$ (cyan lines). For the scan in B_x we observe only one transition (red to yellow colored signal) within the the probed frequency range which is the ZEFOZ transition. For the scan in B_y and B_z, the measurement shows an additional transition whose frequency changes rapidly with the magnetic field. This transition occurs in the other magnetic site and does not impede light storage at the ZEFOZ point. In contrast, the smooth ZEFOZ transition frequency follows a parabola with a minimum close to $\vec{B}_0'$. This is the key feature of ZEFOZ. At $\vec{B} = \vec{B}_0'$ any magnetic noise, i.e., fluctuation of $\vec{B}$, has, in first order, no impact on the transition frequency. This leads to a decoupling of a coherence stored on this transition (i.e., the spin wave for EIT light storage) from the environment, thus enabling extremely long storage times.

We perform fits of parabolas to the data (green lines in Figure 4.1) which give the positions of the minima $B_x^* = (-72.10 \pm 0.04)\,\mathrm{G}$, $B_y^* = (174.05 \pm 0.07)\,\mathrm{G}$, and $B_z^* = (376.67 \pm 0.04)\,\mathrm{G}$. Note, however, that $\vec{B}^* = (B_x^*, B_y^*, B_z^*)$ is not exactly the experimental field of the ZEFOZ point, i.e., $\vec{B}_0'$, which is due to minor fluctuations of the magnetic field in our setup. Nevertheless, the parabolic behavior and the close proximity of $\vec{B}^*$ to $\vec{B}_0'$ (with only 1‰ deviation) prove that the gradient descent algorithm has converged to the ZEFOZ point. Furthermore, the measured transition frequency of 7.27 MHz matches the simulation.

In order to further characterize the ZEFOZ point, we perform a spin echo experiment. Details of the principle behind spin echo measurements in Pr:YSO can be found elsewhere [18, 44]. In short, we first create a ground state population difference by optical pumping at a fixed frequency, create an atomic coherence by an RF $\pi/2$ pulse, use a π pulse for rephasing and read the rephased coherence (i.e., the spin echo signal) by Raman heterodyne detection. This allows us to determine the T_2 time without a specific optical preparation which would require further knowledge of the

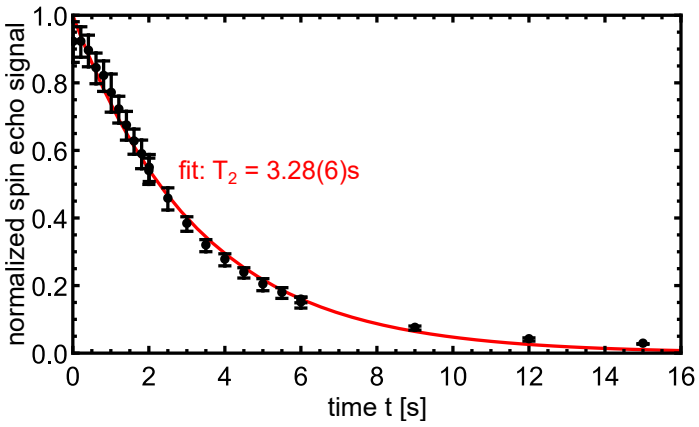

Figure 4.2: Spin echo signal amplitude versus time at the ZEFOZ point. The signal (black data points) decays exponentially. An exponential fit (red line) shows a $1/e$ decay time $T_2 = (3.28 \pm 0.06)$ s. We use the fitted amplitude at $t = 0$ and offset for $t \to \infty$ to normalize the signal and account for an offset of the signal detection using the lock-in amplifier.

level structure. Figure 4.2 shows the spin echo signal over time and an exponential fit. The signal decays exponentially with a characteristic time of $T_2 = (3.28 \pm 0.06)$ s. This is a significant improvement of almost four orders of magnitude compared to the field free case with $T_2 \approx 500\,\mu$s [18]. Compared to another ZEFOZ point (called "A" in [64]) which was used in previous work [18, 69], our result represents an improvement of almost one order of magnitude. This is due to a lower curvature of the transition frequency at the ZEFOZ point used here.

A rough estimation of the coherence time can be calculated via $1/T_2 = S_2(\Delta B)^2$ with the largest of the one-dimensional curvatures $S_2 = \mathrm{d}^2\nu/\mathrm{d}B_z^2 = 21\,\mathrm{Hz/G^2}$ (given by the fitted spectra) and the variance of the magnetic field fluctuation due to yttrium spin flips $(\Delta B)^2 \approx (0.14\,\mathrm{G})^2$ [64]. The estimation gives $T_2 = 2.4$ s which is consistent with our experimental result of $T_2 = 3.3$ s, considering the roughness of the estimation. We note that Longdell *et al.* measured $T_2 = 1.4$ s, i.e., less than half of our result [64]. We explain the higher T_2 in our experiment by a more precise setting of $\vec{B}$ since even minor deviations cause significant reduction of T_2 [66, 69].

4.2 Light Storage Preparation at the ZEFOZ Point

In order to exploit the long coherence time at the ZEFOZ point for EIT light storage, we must apply an optical pumping sequence to prepare a Λ system. Due to the altered level scheme at the ZEFOZ point, the preparation described in Section 2.3 cannot be used. Using a simulation based on the results of Lovrić *et al.* [63], we calculate the level scheme and adapt a preparation scheme developed by Lauritzen *et al.* [89]. Since we expect minor deviations in our experiment, we confirm the simulated level scheme using spectroscopy.

Figure 4.3(a) shows the resulting level scheme. Note that the transition frequencies of the excited state's sublevels are based on the simulation only, while the transition frequencies of the ground state transitions result from our own spectroscopy. The maximal deviation from the simulated values is 26 kHz which is higher than the precision of 7.5 kHz stated by Lovrić *et al.* [63]. However, it can be explained by different samples and varying mechanical stress induced level shifts. In previous work, we observed a variation of the ground state splittings by more than 500 kHz for different ions within the optical inhomogeneous line of the same crystal (i.e., for different local strain within the crystal) [37]. Though we used a Pr:YSO crystal with larger dopant concentration (1%) compared to the sample in our experiment

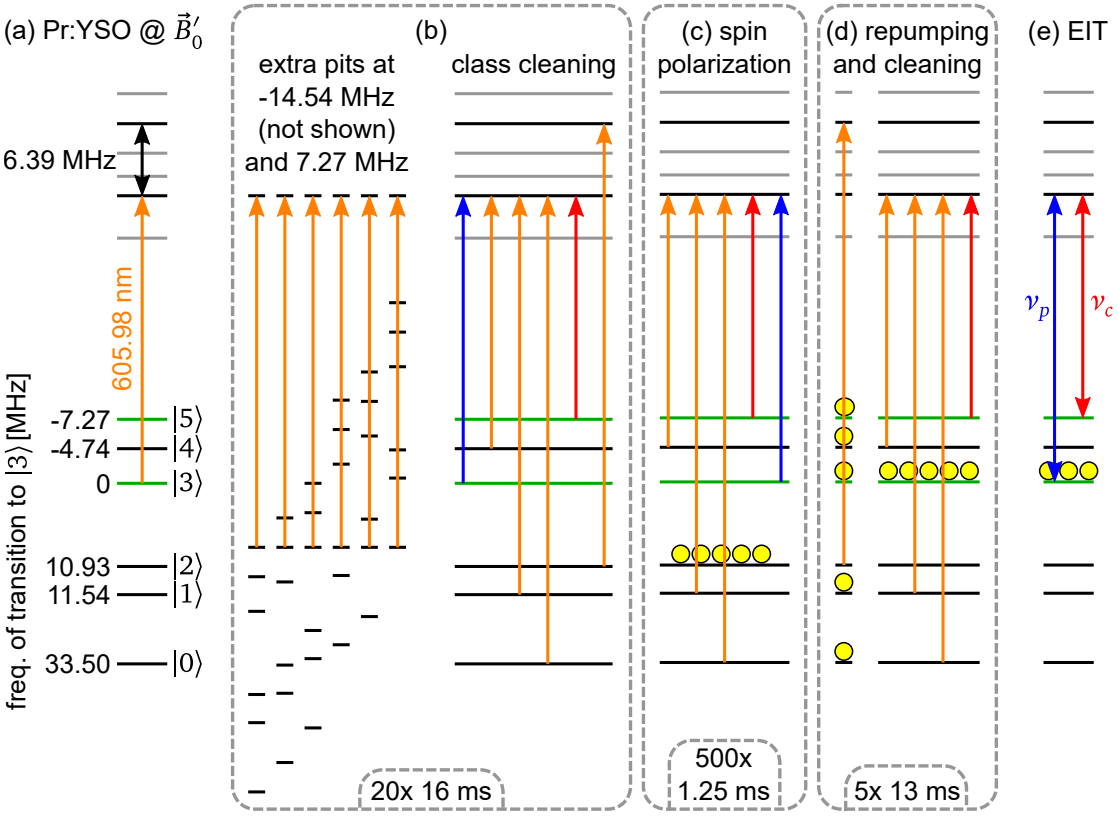

Figure 4.3: Preparation scheme for EIT light storage at the ZEFOZ point $\vec{B}_0' = (-72.30, 174.45, 376.52)$ G. (a) Level scheme of Pr:YSO. The positions of the ground states are determined spectroscopically. The ZEFOZ transition $|3\rangle \leftrightarrow |5\rangle$ is highlighted in green. The excited states' energies are calculated based on [63]. We highlight the 6.39 MHz transition within the excited states because of its relevance for the class cleaning and repumping steps. (b) In the first step, we prepare spectral pits at $\nu_p + 7.27\,\text{MHz}$ and $\nu_p - 14.54\,\text{MHz}$ (with the frequency ν_p of the probe transition) and select the desired ensemble by pumping population in a circular process via two different excited states (class cleaning). (c)–(d) Yellow disks indicate the population after the respective preparation step. (c) In the spin polarization step, we prepare the population in $|2\rangle$ by repeatedly pumping it out of the other five ground states. (d) The repumping pulse pumps part of the population (i.e., only in a single or narrow range of ensembles) out of $|2\rangle$ and cleaning pulses transfer the population into $|3\rangle$. (e) The coupling scheme of EIT involves the second lowest excited state and the ground states $|3\rangle$ and $|5\rangle$, i.e., the ZEFOZ transition with the population (yellow disks) prepared in $|3\rangle$. All pumping pulses in (b) to (d) are chirped with 300 kHz width except for the repumping pulse which has either 200 kHz chirp width (for preparation of an absorption plateau at ν_p) or no chirp (for a single absorption peak at ν_p).

(0.05%), it illustrates the effect of level shifts induced by mechanical stress.

In order to prepare a proper Λ system for EIT within this complicated level structure, we perform a preperation sequence based on spectral tailoring of the absorption profile [89]. The goal of the preparation sequence is to obtain an absorption peak at the frequency of the probe transition ν_p that is not contaminated by absorption of any other transition in any other ensemble than the intended Λ system. At the same time, the preparation must ensure full transmission at the control frequency ν_c. This is an ambitious goal because we have to consider 36 ensembles in each of the two magnetic sites (note that the degeneracy of these sites is lifted at the ZEFOZ point).

The general idea for constructing a preparation sequence described by Lauritzen *et al.* [89] leaves some freedom regarding the choice of the involved states as well as the order and width of the chirps. We use a simulation of the optical pumping process to optimize these parameters with the goal of a high absorption at ν_p and a wide spectral pit at ν_c. The optimized preparation sequence is illustrated in Figures 4.3(b)–(e). We start the preparation by burning two spectral pits at the frequencies $\nu_p + 7.27\,\mathrm{MHz}$ and $\nu_c - 7.27\,\mathrm{MHz} = \nu_p - 14.54\,\mathrm{MHz}$. These pits are not required for preparation of the EIT Λ system [hence the term "extra pits" in Figure 4.3(b)], however, when we apply RF pulses for rephasing (as it is required for prolonging the storage time), remaining absorption at these frequencies might be transferred to ν_p and ν_c. This would limit the efficiency and could cause fluorescence leading to an elevated noise floor. We note, that full transmission of the two pits is not sustained completely during the following preparation steps. However, the absorption remains reduced.

After preparation of the two extra pits, we select 1 of the 72 ensembles by pumping the population in this ensemble in a circular process. This so-called class cleaning step involves six pumping pulses with frequencies chosen such that in the target ensemble each of the ground states is coupled by one of the pulses. Each pulse pumps the population out of the respective ground state and causes a redistribution among the other states according to the transition moments. Since the last pulse couples to a different excited state [see Figure 4.3(b)], the population is pumped in a circular process only within the target ensemble. In other ensembles at least one of the pulses does not couple a transition and therefore the population accumulates in the uncoupled ground states. This means that the population in the unwanted ensembles is "hidden", i.e., it will not be pumped by the following preparation steps. We note that we chirp the pumping pulses which leads to the preparation of a range of ensembles instead of a single one. However, the chirp width of 300 kHz is small enough to avoid pumping of different transitions within one ensemble. Therefore, we can consider the pumping procedure as if there were no chirps. Experimental optimization has shown that 20 repetitions of burning the extra pits and class cleaning (with 2 ms long pulses) are sufficient for eliminating absorption due to other ensembles. According to our simulation it is possible to chirp all pulses over 600 kHz without spoiling the intended coupling. The chirp width directly translates to the width of the prepared pits, especially at ν_c. Therefore, wide chirps are beneficial for avoiding population pumping by the control pulses. Due to the limited linewidth of the laser system and to avoid off-resonant coupling (which is not included in the simulation) we reduce the chirp width to 300 kHz in the experiment.

After the class cleaning, the population is distributed among all ground states but $|2\rangle$ (since $|2\rangle$ was emptied by the last pulse) in the target ensembles. In order to collect all population in a single state, we apply pump pulses at five frequencies (again, chirped by 300 kHz). These pulses pump the population into $|2\rangle$ [see Figure 4.3(c)] and clear all absorption within the 300 kHz wide chirp ranges. We repeat this preparation step (called spin polarization) 500 times with a pulse duration of 250 µs. Now, we apply a 5 ms long repumping pulse that pumps part of the population (i.e., in a subset of the previously prepared ensembles) out of $|2\rangle$ and generates absorption in the previously cleared pits [see Figure 4.3(d)]. By changing the chirp width and frequency of the repumping pulse, we can control the width and spectral position of the absorption feature. Since we aim for a high absorption on the probe transition,

we apply four pulses that pump the previously prepared population to state $|3\rangle$. These cleaning pulses have a duration of 1 ms (for the first three pulses) and 5 ms (for the last pulse). The last pulse cleans the absorption out of the pit at ν_c, hence we choose a longer duration to ensure maximal transmission. Since the cleaning pulses will pump part of the population back into $|2\rangle$, we repeat the repumping and cleaning steps five times to prepare a high absorption at ν_p.

By application of the previously explained steps we prepared a Λ system in an isolated ensemble despite the complicated level structure [see Figure 4.3(e)]. In this Λ system all the population is in one of the ground states such that application of a control pulse will lead to EIT.

We note that the preparation sequence described above is also applicable at magnetic fields in the vicinity of $\vec{B}_0'$. The only requirement is that the level shifts compared to the level scheme in Figure 4.3(a) remain smaller than the chirp width of the involved preparation pulses, i.e., less than 300 kHz. This is the case for the daily fluctuations in the laboratory environment. Therefore, we can apply EIT light storage instead of a spin echo experiment for optimization of the magnetic field using a gradient descent algorithm. This removes the requirement of switching between the experiments and facilitates the implementation.

4.3 EIT and Light Storage at the ZEFOZ Point

Now, we perform spectroscopy to measure the prepared absorption feature around ν_p. Figure 4.4(a) shows the absorption spectra after different steps of the preparation sequence. After the spin polarization (blue graph), high transmission is observed over the 600 kHz wide frequency range. From a simulation of the pumping process we expect only a 300 kHz wide pit (corresponding to the chirp width of the preparation pulses). We explain the broad transmission range by off-resonant coupling and frequency jitter of the laser system (note that the preparation takes almost 1 s until the spin polarization is finished, so jitter on this long timescale becomes relevant). Since we reduced the chirp width of the preparation pulses compared to the maximal possible width of 600 kHz, the broader pumping range does not impede a proper preparation.

The green graph in Figure 4.4(a) shows the absorption spectrum after the repumping and cleaning pulses. We find a rectangular absorption plateau (despite the washed-out edges) with 200 kHz width and OD ≈ 2.3 which matches the 200 kHz chirp width of the repumping pulse. As we will see later, preparation of an absorption plateau slightly increases the light storage efficiency compared to preparation of a single absorption peak. At the edges of the spectrum we observe an increased absorption up to OD ≈ 0.5 which we do not expect from the simulation and which indicates unintentional pumping of other ensembles. By interpolation we expect these ensembles to contribute to a background absorption at ν_p which will lower the EIT visibility and storage efficiency. We tried to circumvent this pumping by changing the chirp width, power, duration, number of repetitions and order of the preparation pulses, but were unable to reduce the absorption below the value observed in Figure 4.4(a). When we apply a control pulse with $P_c = 20$ mW power, the absorption plateau is split in two peaks with ~ 200 kHz separation indicating a control Rabi

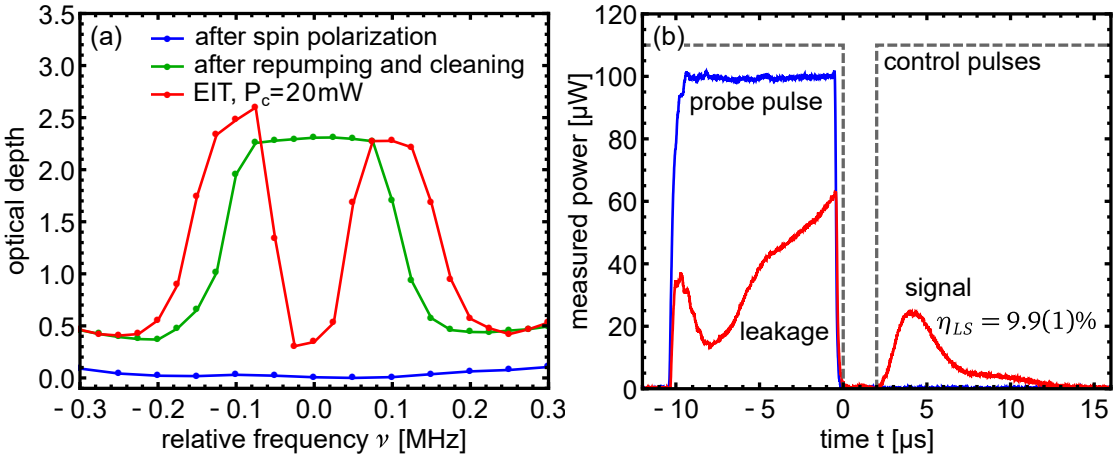

Figure 4.4: EIT and light storage measurements at the ZEFOZ point. (a) OD versus frequency (relative to the probe frequency ν_p) around ν_p. Colors indicate at which time of the preparation the spectrum was measured (see legend). (b) EIT light storage of a classical pulse: optical power versus time. We store a 10 µs long probe pulse (blue) at time $t = 0\,\mu s$ by the control write pulse with $P_c = 15\,mW$ (gray, dashed line, power not to scale). A part of the pulse is not stored and leaks through the medium (red graph for $t < 0\,\mu s$). After 2 µs storage time, the control read pulse retrieves the signal (red graph for $t > 2\,\mu s$). Division of the signal and probe pulse areas gives a storage efficiency of $\eta_{LS} = (9.9 \pm 0.1)\%$.

frequency of $\Omega_c \approx 2\pi \times 200\,kHz$. This is about 30% higher than expected from EIT measurements at zero field which indicates a slightly higher dipole moment of the control transition at the ZEFOZ point. Between the peaks we find a transmission window with residual OD ≈ 0.4. This indicates a working EIT scheme with a maximal transmission limited by background absorption coming from additional ensembles.

Using EIT, we perform light storage of classical pulses. The measured pulse shapes are shown in Figure 4.4(b). We store a 10 µs long probe pulse (blue) using a control write pulse with Rabi frequency $\Omega_c \approx 2\pi \times 170\,kHz$ (indicated by the gray, dashed line). We obtained the highest efficiency for these parameters (when restricting the probe pulse shape to a rectangular temporal profile). The red line shows the leakage of the probe pulse (for $t < 0\,\mu s$) and the signal pulse retrieved after $t_s = 2\,\mu s$ storage time. The efficiency of the storage process is $\eta_{LS} = 9.9 \pm 0.1\%$ which matches our expectation for an absorption feature with OD ≈ 2. This result shows that we developed a working preparation sequence for EIT light storage at the ZEFOZ point which enables a reasonably high efficiency at short storage times.

In this chapter, we discussed the application of a magnetic field to implement ZEFOZ for increasing the coherence time. We confirmed the ZEFOZ behavior at this field by spectroscopy and reached a coherence decay time of $T_2 = 3.3\,s$ in a spin storage experiment. Compared to measurements of Longdell *et al.*, we achieved an almost twofold increase in coherence time which indicates the superior magnetic field homogeneity in our setup. We showed light storage on a short timescale with an efficiency of $\eta_{LS} = 9.9\%$ which required a specific optical preparation sequence. Our result represents the first EIT light storage experiment at this ZEFOZ point in Pr:YSO.

Chapter 5

Efficient Storage of Classical Light Pulses up to One Second

In this chapter, we focus on prolonging the storage time at the ZEFOZ point using DD without compromising the efficiency. This is challenging because DD requires the application of many, potentially imperfect, rephasing pulses, each reducing the efficiency, which is a well known problem. For example, Ma *et al.* report a rephasing efficiency in the range of only 10% for application of 3000 pulses [20]. To achieve efficient storage with DD, we optimize the rephasing pulse parameters, increase the storage efficiency using the multipass setup and finally apply a robust and efficient DD sequence. The latter is a common technique to counteract pulse imperfections via error compensating pulse sequences. Here, we report on the implementation of a universal robust sequence with unprecedented order of error compensation.

5.1 Rephasing for Light Storage at the ZEFOZ Point

As explained in Section 1.2, without rephasing, the storage time is limited to $T_2^* \approx 10\,\mu s$. In this section, we present the optimization of a simple rephasing sequence to extend the storage time beyond T_2^*.

Optimization of π Pulse Parameters

In order to prolong the storage time beyond T_2^*, we must apply π pulses on the transition carrying the coherence, i.e., the ZEFOZ transition at frequency $\nu_Z = \nu_p - \nu_c = 7.269\,\text{MHz}$. Our setup contains a pair of impedance matched Helmholtz coils for application of magnetic fields at this frequency. Since the area of the pulses (i.e., the product of the Rabi frequency and the duration) must be fixed to π and a short duration τ is beneficial (due to the increased spectral width, more ensembles within the inhomogeneous line can be addressed), we use pulses with maximal possible amplitude, limited by the power of the RF amplifier. In order to determine the optimal values for τ and the frequency ν_{RF}, we perform EIT light storage with a storage time of $t_s = 100\,\text{ms}$, i.e., far longer than T_2^* but well below T_2. We apply two RF pulses centered at $t_\pi^{(1)} = 25\,\text{ms}$ and $t_\pi^{(2)} = 75\,\text{ms}$, systematically change the pulse parameters τ and ν_{RF} and determine the light storage efficiency as a measure for the rephasing efficiency.

Figure 5.1(a) shows the measured efficiency for the maximal RF power $P_{RF} \approx 15\,\text{W}$. The power is limited by the 30 W amplifier giving a maximum of 15 W transferred to the Helmholtz coils (assuming perfect impedance matching, i.e., maximal power transfer, and no additional losses). We measure a maximal light storage efficiency of $\eta_{LS} = (1.52 \pm 0.07)\%$ for $\nu_{RF} = 7.259\,\text{MHz}$ and $\tau = 36\,\mu s$ (marked by the green cross). From the π pulse duration τ we conclude a Rabi frequency $\Omega_{RF} = 2\pi \times 1/(2\tau) \approx 2\pi \times 14\,\text{kHz}$. This is lower than the inhomogeneous width of the

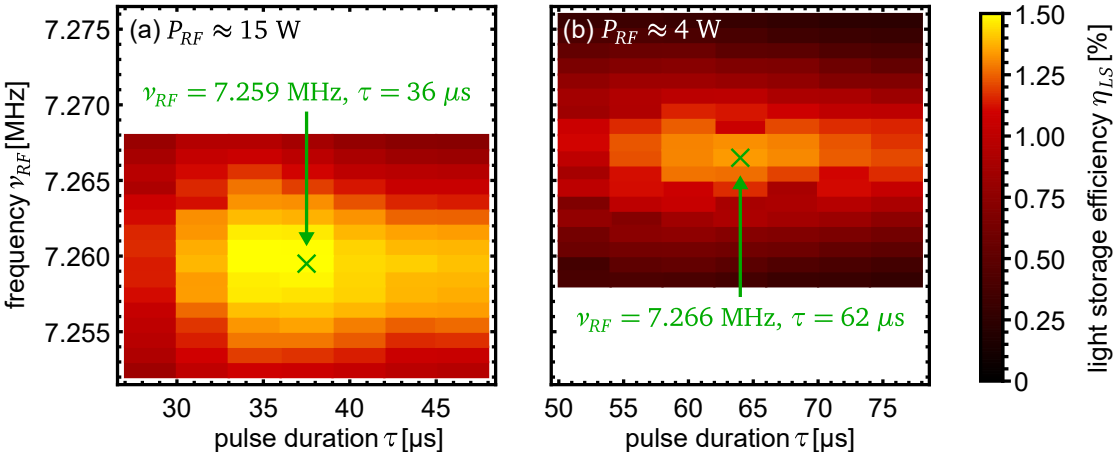

Figure 5.1: Light storage efficiency (color scale) versus the π pulse parameters duration τ and frequency ν_{RF} for rephasing of light storage at the ZEFOZ point with $t_s = 100$ ms storage time rephased by two π pulses. In (a) we use the maximal RF power $P_{RF} \approx 15$ W (in the Helmholtz coils) and in (b) we use half the amplitude, i.e., reduce the power to $P_{RF} \approx 4$ W. For higher P_{RF}, the maximal efficiency ($\eta_{LS} = 1.5\%$) is higher and the optimal frequency ($\nu_{RF} = 7.259$ MHz) and pulse duration ($\tau = 36\,\mu$s) are lower (marked by the green crosses).

transition $\Gamma \approx 2\pi \times 30$ kHz which means that we can rephase only a part of the coherences. This explains the low rephasing efficiency (defined as the ratio of the light storage efficiencies with and without rephasing) of $\eta_r = 15\%$.

The optimal frequency of $\nu_{RF} = 7.259$ MHz differs substantially from the measured transition frequency $\nu_Z = 7.269$ MHz. We explain this by an ac Stark shift which is induced by the RF field. The most relevant off-resonant couplings (i.e., with the lowest detunings) of the RF field with angular frequency $\omega_{RF} = 2\pi \times 7.27$ MHz are shown in Figure 5.2. The detunings Δ_{ij} of the couplings of the states $|2\rangle$ and $|4\rangle$ to the states $|3\rangle$ and $|5\rangle$ are such that the ac Stark shift will increase the energy of $|3\rangle$ and decrease the energy of $|5\rangle$, i.e., lower the transition frequency ν_Z of the ZEFOZ transition $|3\rangle \leftrightarrow |5\rangle$. In order to confirm this explanation, we repeat the π pulse parameter scan with reduced RF power where we expect the ac Stark shift to to be lower.

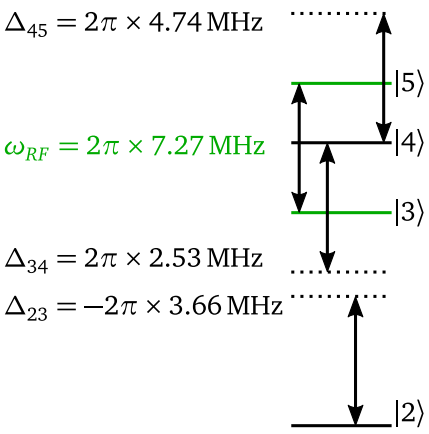

Figure 5.2: Off-resonant couplings (dashed lines) of the RF field at angular frequency ω_{RF}. All couplings are detuned such that the $|3\rangle \leftrightarrow |5\rangle$ transition shifts to lower frequency.

Figure 5.1(b) shows the measurement for halved amplitude of the RF field, i.e., when we apply a quarter of the power. We see that the optimal π pulse duration is now $\tau = 62\,\mu$s, i.e., about 70% longer. We calculate a Rabi frequency of $\Omega_{RF} \approx 2\pi \times 8$ kHz. The lower Rabi frequency causes a further reduction of the efficiency to $\eta_{LS} = (1.34 \pm 0.03)\%$. The optimal frequency is now $\nu_{RF} = 7.266$ MHz, i.e., only 3 kHz different from ν_Z. Based on the assumption of an ac Stark shift, the reduction of the frequency shift from 10 kHz to 3 kHz is consistent with the reduction of Ω_{RF} by 42% since the ac Stark shift scales

quadratically with the Rabi frequency.

In conclusion, we found parameters for RF π pulses that enable rephasing of EIT light storage signals. The rephasing efficiency is only 15% due to a low RF Rabi frequency compared to the inhomogeneous linewidth of the ground state transition. Because of the ac Stark shift, the optimal RF frequency $\nu_{RF} = 7.259\,\text{MHz}$ differs from the transition frequency. Using two π pulses for rephasing, we achieve a light storage efficiency of $\eta_{LS} = 1.5\%$ at 100 ms storage time.

Optimal Timing of π Pulses

In the previously shown experiment we chose a storage time of $t_s = 100\,\text{ms}$. This means that the rephasing π pulses had a temporal separation of $t_{\text{sep}} = t_s/2 = 50\,\text{ms}$. According to the theory of DD, the separation between the rephasing π pulses should be as low as possible in order to reach maximal coherence time [47–49]. Figure 5.3 shows the light storage efficiency for storage times t_s shorter than 100 ms. For all data points, i.e., storage times, we use two π pulses for rephasing. This means that shorter storage times correspond to shorter t_{sep}. We expect a constant efficiency since $t_s \ll T_2$ for all storage times t_s in the investigated parameter range. For $t_s \geq 20\,\text{ms}$ we find a constant efficiency of $\eta_{LS} \approx 1.28\%$. The slightly lower efficiency compared to the previous measurement is due to non-optimized light storage parameters. However, for storage times below 20 ms, i.e., $t_{\text{sep}} < 10\,\text{ms}$, the efficiency drops significantly (red data points). To increase T_2 by DD, smaller t_{sep} are beneficial. Therefore, the unexpected drop of rephasing efficiency poses a limitation for DD (since we cannot reduce t_{sep} below 10 ms). In previous work, the lower bound to the pulse separation t_{sep} was 100 µs, limited by heating of the crystal (note that a shorter separation also means a higher duty cycle, i.e., higher average power) when DD was applied [18]. Since the setup in the cryostat was changed only slightly in this work, we expect heating effects to play a role on a similar timescale, i.e., two orders of magnitude shorter than the limit of $\sim 10\,\text{ms}$. Additionally, in the experiments presented here, we apply only two π pulses, i.e., no DD. Therefore, the overall RF energy is significantly lower than for DD.

In order to investigate the loss of efficiency for short storage times, we measure absorption spectra after application of two π pulses with $t_{\text{sep}} = 50\,\text{ms}$. Figure 5.4(a) shows the absorption plateau for two different waiting times after the second π pulse. Compared to the spectra obtained directly after the preparation sequence [see Figure 4.4(a)], the absorption of the plateau has dropped to OD ≈ 1.6 (from

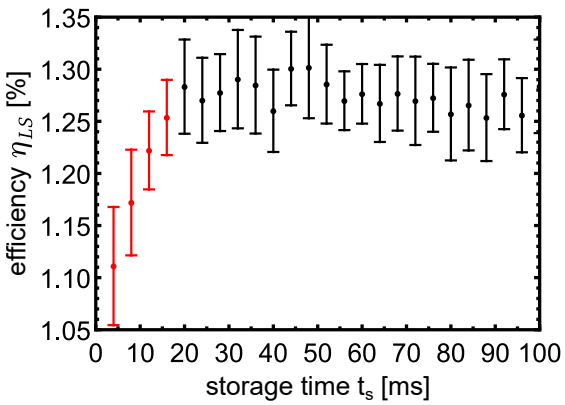

Figure 5.3: EIT Light storage efficiency versus storage time t_s at the ZEFOZ point rephased with two π pulses. The π pulses have maximal amplitude, frequency $\nu_{RF} = 7.259\,\text{MHz}$ and $\tau = 39\,\mu\text{s}$ duration. The parameters were optimized prior to this experiment. The efficiency is constant for times $20\,\text{ms} \leq t_s \leq 100\,\text{ms}$ but drops for times below 20 ms (red data points).

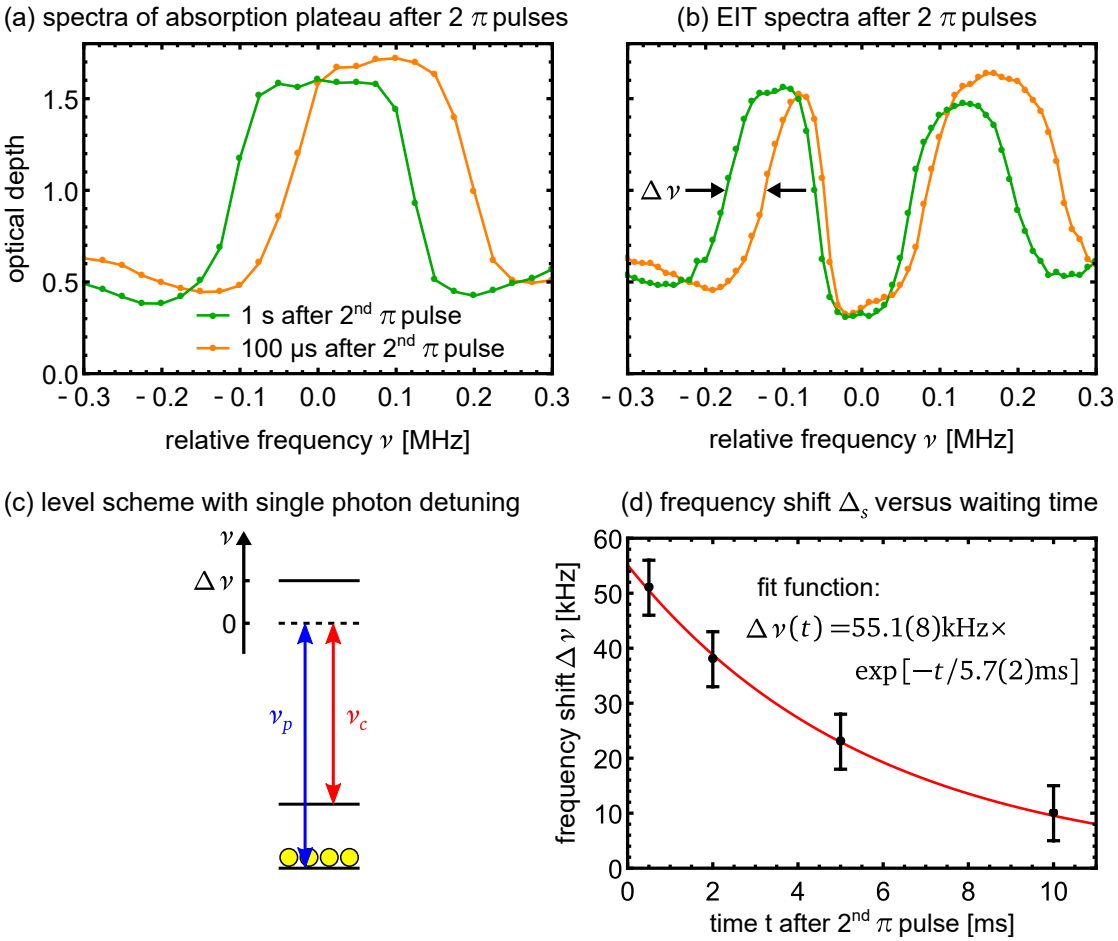

Figure 5.4: Absorption measurement after application of two π pulses. (a)–(b) OD versus frequency. The prepared absorption plateau (a) and EIT for $P_c = 30\,\mathrm{mW}$ (b) are measured $100\,\mu\mathrm{s}$ (orange lines) and $1\,\mathrm{s}$ (green lines) after application of the second π pulse. For the short delay, the absorption plateau is shifted to higher frequencies but the position of the EIT window remains almost unchanged. (c) The EIT level scheme with shifted excited state explains the observed behavior. (d) Frequency shift versus waiting time after the second π pulse. The initial shift of $\Delta\nu \approx 55\,\mathrm{kHz}$ decreases exponentially with time. From the fit (red graph) we deduce a $1/e$ time of $5.7 \pm 0.2\,\mathrm{ms}$.

originally OD ≈ 2.3) which is due to the imperfect π pulses. Additionally, we see that the plateau is shifted to higher frequencies for the measurement $100\,\mu\mathrm{s}$ after the second π pulse (orange graph). We do not expect this as the π pulses should only transfer population between the ground states within an ensemble, i.e., only swap the absorption between the probe and control frequencies. Furthermore, the shift is revoked in the measurement $1\,\mathrm{s}$ after the second π pulse (green graph). This indicates a temporary shift of one of the involved states. We do not expect this shift to be related to the ac Stark shift observed in the previous subsection because of the millisecond timescale on which the shift is present after the RF pulse.

When we apply a control pulse, we obtain the EIT spectra shown in Figure 5.4(b). We still find a shift of the absorption structure by $\Delta\nu$ (measured as the shift of the leftmost flank) for the measurement after $100\,\mu\mathrm{s}$ (orange graph) but the EIT window remains almost unchanged and centered at the relative frequency $\nu = 0\,\mathrm{MHz}$, i.e.,

the probe frequency. This finding proves that the probe and control fields are in two-photon resonance for $\nu = 0\,\mathrm{MHz}$, independent of the shift of the absorption plateau. We illustrate this situation in the level scheme shown in Figure 5.4(c). A shift of the optically excited state to higher energy (or, equivalently, a reduction of both laser frequencies) explains the shifted absorption feature by the resulting single photon detuning. The two-photon detuning, relevant for EIT, remains unaffected.

The experimental origin of the shift is unclear. We note that even if we do not apply a static magnetic field, a pulse with $\nu_{RF} = 7.259\,\mathrm{MHz}$ causes a shift of a previously prepared absorption peak. In this case there is no transition at ν_{RF}, so this finding indicates an external origin. Possible explanations are a heating induced level shift (although we expect heating to be irrelevant on the millisecond timescale) or a shift of the overall frequency of the OPO based laser system. Note, that in contrast to previous work in which RF π pulses were applied, we use a different laser system which might be affected by strayed RF radiation [18, 43, 44]. To compensate the frequency shift and thereby preserve high storage efficiency, we could change the frequency of the control read pulse to be in single photon resonance again. However, as the origin of the shift is not known, we cannot foresee additional consequences, e.g., a violation of the phase matching condition or a changed signal frequency. Instead, we exploit that the shift reduces over time. As we saw in Figure 5.3, the efficiency is only reduced for storage times below $\sim 20\,\mathrm{ms}$. In order to confirm this timescale, we measure the frequency shift $\Delta\nu$ for different waiting time after the second π pulse, see Figure 5.4(d). The frequency shift decays exponentially with a characteristic time of $(5.7 \pm 0.2)\,\mathrm{ms}$ (see fitted function in red). This confirms the timescale of $t_s \geq 20\,\mathrm{ms}$ after which efficient readout is possible since for $t_s = 20\,\mathrm{ms}$ the readout occurs 5 ms after the second π pulse. For shorter separation, which would be beneficial for DD, the light storage efficiency drops.

5.2 Optimizing the Light Storage Efficiency at ZEFOZ

In this section, we focus on increasing the light storage efficiency in general, i.e., already on a short timescale. We first explain the positive effect of performing EIT in an inhomogeneously broadened absorption plateau instead of an isolated peak and then we apply the multipass setup to increase the light storage efficiency.

5.2.1 Exploiting the Increased Dispersion of EIT on an Inhomogeneously Broadened Transition

In Section 4.2 we saw that it is possible to prepare an absorption plateau instead of a single peak by chirping the repumping pulse. EIT remains possible despite the increased inhomogeneous linewidth (see Section 4.3). Indeed, the spectrally broader plateau even enables a slightly larger storage efficiency. In the following, we explain the reason for this feature.

We compare the susceptibility χ of a single absorption peak without inhomogeneous broadening to a uniform distribution (within a certain width) of absorption peaks. By appropriate normalization we ensure the same peak absorption in both cases. This mimics the situation in the experiment as the chirped repumper, com-

pared to a single frequency repumper, will only add ensembles at other transition frequencies but not increase the absorption at the central frequency. We calculate χ according to [32] and set the control Rabi frequency to $\Omega_c = 3\gamma_{12}$.

Figure 5.5 shows the resulting normalized susceptibility $\tilde{\chi}$. In Figure 5.5(a) we plot the imaginary part of $\tilde{\chi}$ which defines the absorption coefficient according to $\alpha \propto (2\pi/\lambda)\,\mathrm{Im}\,\tilde{\chi}$ (note the proportionality due to the normalization of χ). In the case of a single absorption peak and resonant control field (green graph) we find an EIT window with spectral bandwidth $\Gamma_{EIT} = 2.37\gamma_{12}$ (assuming OD = 2, i.e., the situation at the ZEFOZ point). For the detuned peaks (dashed lines), the EIT window is asymmetric but also exhibits high transmission at $\Delta_p = 0$. The nonzero (but low) absorption in the EIT window is due to the nonzero ground state decoherence rate γ_{13}. In the modeled absorption plateau (consisting of absorption peaks evenly distributed over $8\gamma_{12}$), the EIT window has a reduced width of $\Gamma'_{EIT} = 0.89\gamma_{12}$ and a higher residual absorption at $\Delta_p = 0$.

Figure 5.5(b) shows the real part of $\tilde{\chi}$ which (in approximation of optically thin media) defines the refractive index according to $n - 1 \propto \mathrm{Re}\,\tilde{\chi}/2$. For frequencies within the EIT window of all simulated absorption features, we find a positive slope, i.e., normal dispersion. However, in the case of the absorption plateau (orange graph), the slope is significantly steeper. Since the slope is inversely proportional to the group velocity, this effect increases the spatial compression of a probe pulse (compare Section 1.1) and enables the storage of longer pulses. Comparison of the slopes at $\Delta_p = 0$ shows a 5.6 times increased slope for the plateau, compared to

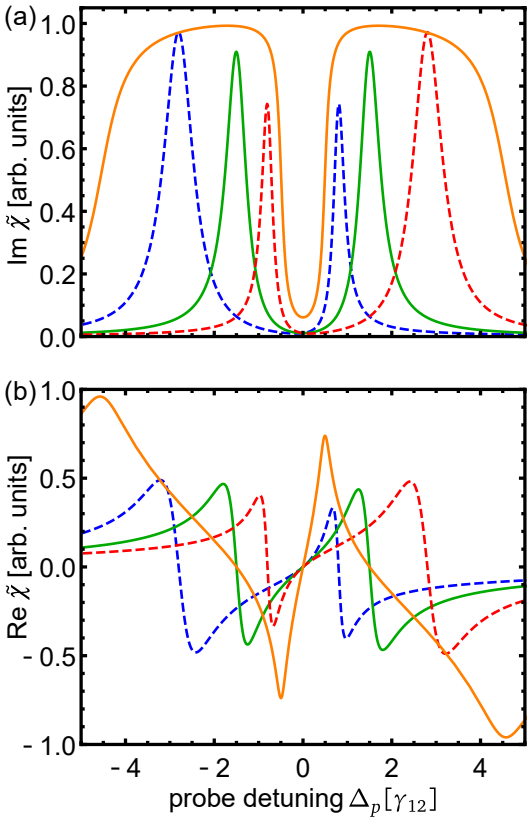

Figure 5.5: Susceptibility for EIT in single absorption peaks and an inhomogeneously broadened absorption plateau versus probe detuning Δ_p. We simulate three absorption peaks centered at different Δ_p ($\Delta_p = \pm 2\gamma_{12}$ for the dashed red and blue lines and $\Delta_p = 0$ for the green lines) and leave the control frequency fixed to give two-photon resonance for $\Delta_p = 0$. We assume a control Rabi frequency of $\Omega_c = 3\gamma_{12}$, a ground state decoherence rate of $\gamma_{13} = 0.1\gamma_{12}$ and a $8\gamma_{12}$ wide distribution of peaks constituting the plateau. (a) The imaginary part of $\tilde{\chi}$ (i.e., the absorption) shows an EIT window at $\Delta_p = 0$ for all single photon detunings and the absorption plateau (orange). In the resonant case (green), the absorption peak is split into two peaks with identical height and in the detuned cases (dashed lines), the peak heights differ. The EIT window of the absorption plateau is about 2.6 times narrower than for the resonant single peak. (b) The real part of the susceptibility has a positive slope (i.e., normal dispersion) around $\Delta_p = 0$. For EIT in the absorption plateau (orange), the slope is about 5.6 times steeper than in the case of a single absorption peak (green).

the single, resonant peak. This means that pulses with 5.6 times longer duration, i.e., 5.6 times narrower spectrum can be stored. At the same time the EIT window width, which limits the spectrum of the probe pulse, is only reduced by a factor of 2.7. This means that the effect of the reduced group velocity outweighs the effect of the narrowed EIT window.

In conclusion, the preparation of a broad absorption plateau instead of an equally high, but narrow absorption peak relieves the spatial condition for efficient EIT light storage significantly (compare Section 1.1) while tightening the spectral condition only slightly. We expect the combination of both effects to enable higher storage efficiency. At the ZEFOZ point we found that the preparation of a 200 kHz wide plateau gives $\sim 15\%$ increase in efficiency compared to preparation of a single peak with FWHM ≈ 75 kHz. In all light storage experiments at the ZEFOZ point presented in this theses we prepare a 200 kHz wide absorption plateau instead of a single peak (as described in Section 4.2).

5.2.2 Optimization of the Probe Pulse Shape and Multipass Order

By using an appropriate pumping scheme and a chirped repumper, we optimized the preparation sequence for efficient EIT light storage at the ZEFOZ point. However, due to the reduced OD, the achieved efficiency of $\sim 10\%$ was well below the value of $\sim 40\%$ achieved with no magnetic field. This means that for storage of weak coherent pulses, the signal level would be reduced by a factor of 4. Furthermore, as we will see in the next chapter, the reduced frequency difference between the probe and control pulses leads to an additional reduction of the SNR. Therefore, we need to further increase the storage efficiency. As we saw in Chapter 1, maximal efficiency is only achieved for storage of an appropriately chosen temporal profile of the probe pulse (for given control write and read pulse profiles). In the following, we present an iterative algorithm that we use to experimentally find the optimal pulse shape. This algorithm was proposed by Gorshkov *et al.* and first applied by Novikova *et al.* [33, 39].

Figure 5.6 shows the pulse shapes when we apply the iterative pulse shaping algorithm to light storage for $N = 1$ at the ZEFOZ point. We start by storage of a rectangular probe pulse as discussed in Section 4.3. The resulting signal pulse (red line for $t > 2\,\mu$s) differs significantly from the rectangular shape of the probe pulse (blue graph). Following the arguments of [33], this means that the efficiency of $\eta_{LS}^{(0)} = (9.90 \pm 0.13)\%$ is not the maximal possible efficiency. We use the measured signal pulse to calculate a new probe pulse shape via time inversion and normalization to the original pulse energy of 1 nJ. Storage of this probe pulse results in an increased efficiency of $\eta_{LS}^{(1)} = (11.28 \pm 0.07)\%$. Now, the signal and probe pulse shapes are nearly identical (despite the lower amplitude of the signal). When we repeat the pulse shaping in a second iteration, the efficiency hardly increases to $\eta_{LS}^{(2)} = (11.31 \pm 0.15)\%$. This shows that the pulse shape has quickly converged to its optimum, i.e., to the temporal profile resulting in the maximal possible efficiency at the given OD ≈ 2.3. At this OD we calculate a maximal possible efficiency of 13% for EIT in a single absorption peak and slightly higher in our case due to the preparation of an absorption plateau. The slightly lower experimental value $\eta_{LS}^{(2)} = 11.3\%$ is due to residual absorption in the EIT window caused by additional ensembles (see Section 4.3).

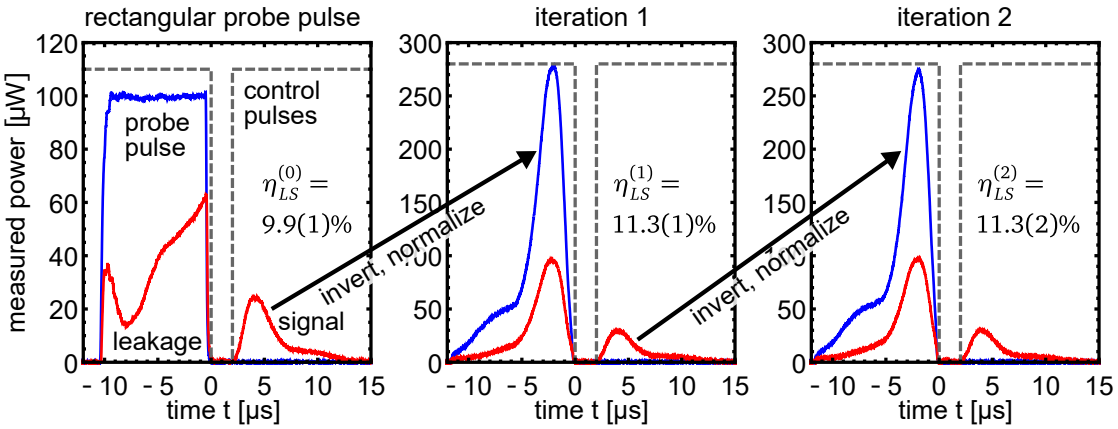

Figure 5.6: Measured optical power versus time during the iterative pulse shaping algorithm for EIT light storage at the ZEFOZ point in a single pass. We use a control pulse power of $P_c = 15\,\mathrm{mW}$ and start with storage of a rectangular probe pulse with duration $\tau_p = 10\,\mu\mathrm{s}$. The storage efficiency is $\eta_{LS}^{(0)} = (9.90 \pm 0.13)\%$. To calculate the probe pulse shape of the fist iteration, we time invert the signal pulse and normalize it to a pulse energy of 1 nJ. This process increases the efficiency to $\eta_{LS}^{(1)} = (11.28 \pm 0.07)\%$. When we repeat the pulse shaping in a second iteration, the pulse shape is changed only marginally and the efficiency hardly increases to $\eta_{LS}^{(2)} = (11.31 \pm 0.15)\%$.

In order to further increase the efficiency, we require larger OD of the storage medium. To achieve this goal, we use a multipass geometry for the probe pulse propagating through the crystal. This increases the OD by the number of passes. However, in this setup the probe pulse has to pass several optics before reentering the crystal. Although the optics have an anti-reflection coating, a small portion of the pulse is lost at each optical surface, reducing the transmission. For storage of weak coherent pulses, this leads to a reduced number of detected photons and, hence, to an increased statistical error. Since the control read pulse, which is the main source of optical background, is not affected by the reduced transmission, the SNR will be reduced due to non-perfect transmission of the signal pulse. At a critical number of passes, the additional efficiency that can be gained by adding another pass cannot outweigh the losses anymore [35]. This is due to the reduced efficiency gain for a given step in OD at higher OD (compare Section 1.1).

In order to find the optimal number of passes, we measure the efficiency η_{LS} (after application of the pulse shaping algorithm) and the transmission $\mathcal{T}$ of our storage setup, i.e., from the entrance window of the storage cryostat to the beginning of the filter setup, for different N. Based on these values, we calculate the setup efficiency $\eta = \eta_{LS}\mathcal{T}$ which is the relevant measure for storage and readout of weak coherent pulses with high SNR. Table 5.1 shows the results. As expected, η_{LS} increases with N and reaches $\eta_{LS} = (23.3 \pm 0.6)\%$ at $N = 3$. The relative increase of η_{LS} is 68% for $N = 1 \rightarrow 2$ but only 23% for $N = 2 \rightarrow 3$. This is the expected behavior for higher OD (see Section 1.1). The transmission $\mathcal{T}$ drops by about 15% with each additional pass. Due to this reduction in $\mathcal{T}$, the setup efficiency η hardly increases for $N = 2 \rightarrow 3$. Within the uncertainty ranges, we achieve $\eta = 14\%$ for both $N = 2$ and 3.

In the ring-type multipass setup the probe pulse passes the Pr:YSO crystal in each pass under a slightly different angle. Due to a minor inhomogeneity in the static

Table 5.1: Maximal efficiency η_{LS}, transmission $\mathcal{T}$, setup efficiency η and coherence time T_2 for different number of passes N through the storage crystal. The storage efficiency increases with N but the transmission reduces. This limits the setup efficiency to $\eta = (14.4 \pm 0.4)\%$. At $N = 3$ the coherence time drops due to increased inhomogeneity of the magnetic field.

N	η_{LS} [%]	$\mathcal{T}$ [%]	η [%]	T_2 [s]
1	11.3±0.2	84.3±0.4	9.5±0.1	1.51±0.02
2	19.0±0.2	72.7±0.6	13.8±0.2	1.75±0.04
3	23.3±0.6	61.8±0.5	14.4±0.4	1.22±0.02

magnetic field, this means that for high N the local magnetic field $\vec{B}$ within the probe beam path differs from the ZEFOZ point. Since the coherence time T_2 is very sensitive to the exact setting of $\vec{B}$, the maximal possible storage time might diminish for increasing N. Table 5.1 gives the T_2 times for each N, measured with two π pulses for rephasing of the optimized light storage signal. Before measuring T_2, we perform a gradient descent algorithm to optimize $\vec{B}$ for each setting of N. We get the maximum $T_2 = (1.75 \pm 0.04)$ s for $N = 2$. This is only about half the time measured in the spin storage experiment (see Section 4.1). We expected the coherence time to be identical to the spin storage experiment and suspect the difference to originate from large pulse errors caused by the low RF Rabi frequency (indicated by the low rephasing efficiency of 15%, see Section 5.1). In the case of light storage, a partial loss of coherence (due to imperfect rephasing) will not only reduce the signal amplitude, as it is the case for spin echoes, but also cause a reabsorption of the obtained signal. Therefore, pulse errors have a different impact on spin storage and light storage experiments. However, the exact process leading to the reduced T_2 time in the light storage experiment remains unknown. Since $T_2 = 1.75$ s is well above 1 s, we omit further investigations.

In the data set given in Table 5.1, T_2 is lower for $N = 1$ than for $N = 2$. This is due to imperfect setting of $\vec{B}$ (in the measurement with $N = 1$) and we measured T_2 times in the range of 1.75 s (i.e., the value for $N = 2$) on several other days of measurement. The drop of T_2 for $N = 3$ to 1.22 s, however, is due to non-perfect overlap of the probe beam passes, as explained above. We performed a thorough optimization of $\vec{B}$ using the gradient descent algorithm but could not increase T_2 further. Due to the decreased T_2 time at $N = 3$ and the fact that the setup efficiency at $N = 3$ is only marginally higher than for $N = 2$ we perform the following measurements using the double pass setup, i.e., $N = 2$. Additionally, this setup has the advantage that the overall length of the beam path is shorter than for higher N. This facilitates the adjustment and mitigates the requirement of interferometric stability of the optics involved in the multipass setup.

In this section, we presented the optimization of the light storage efficiency by means of the preparation of a broad absorption plateau, shaping of the probe pulse and application of the multipass setup. Using $N = 2$ passes, we achieved a setup efficiency of $\eta = 13.8\%$ and, in the same configuration $T_2 = 1.75$ s for rephasing with two π pulses. In the following, we present DD sequences that enable an even longer storage time.

5.3 Composite Pulses for Dynamical Decoupling

In the measurements shown in Section 5.1 we determined the optimal π pulse parameters that give the highest efficiency when we apply two π pulses for rephasing. However, the rephasing efficiency is only 15%. This is due to the low RF Rabi frequency of $\Omega_{RF} \approx 2\pi \times 14\,\mathrm{kHz}$ compared to the inhomogeneous width of $\Gamma \approx 2\pi \times 30\,\mathrm{kHz}$ of the transition [41]. Many ions within the inhomogeneous width are detuned by $\Delta \approx \Omega_{RF}$ from the π pulse's carrier frequency (set to the central frequency). At such a large detuning, the RF pulse is not a π pulse anymore, i.e., does not invert the quantum state and cannot fully refocus the coherence phase. In this section, we briefly present universally robust (UR) composite DD sequences, which enable rephasing of coherences despite such large pulse errors. This includes not only errors in the detuning but also other pulse imperfections, e.g., pulse area errors, which might arise due to the inhomogeneity of the RF field. Here, we give only a brief overview over the technique and refer to [57] for a more detailed description.

When we aim for long storage times, we use DD to suppress the influence of the environment on the stored coherence. The basic idea of DD is to apply a sequence of rephasing pulses during the storage time and thereby cancel many decoherence processes (see also Section 1.2) [47–49]. We assume now that the single π pulses have errors, e.g., variations in the pulse amplitude, pulse shape, or carrier frequency, as it is typical in any experiment. To evaluate the performance of such a rephasing sequence involving pulse errors, we consider the Bloch vector which depicts the state $|\psi\rangle$ of the ground state transition $|1\rangle \leftrightarrow |3\rangle$, i.e., $|\psi\rangle = \cos(\theta/2)|1\rangle + \exp\{i\varphi\}\sin(\theta/2)|3\rangle$, by means of the density operator $\hat{\rho} = |\psi\rangle\langle\psi|$. For EIT light storage, $\hat{\rho}$ represents the state of the medium at a specific position. At different positions, the mixing angle θ and the phase φ vary according to the amplitude and complex phase of the spin wave. Note that the representation by a pure state is only applicable for a single atom and a mixed state has to be used when considering several ensembles. However, the pure state representation is equivalent to the mixed state of identical atoms experiencing the same external influences.

Let us first consider, as a simple example, the effect of a detuning error. We consider a sequence of 8 pulses with a detuning of $\Delta = 0.5\Omega_{RF}$ for rephasing of two different initial states (with different phase φ). Figures 5.7(a) and (b) show the evolution of the Bloch vector from the initial to the final position. When we apply eight π pulses (note that the pulse area of π is only valid for $\Delta = 0$), the final Bloch vector differs significantly from the initial Bloch vector, indicating a low fidelity and hence a low rephasing efficiency. This is due to the large detuning which causes the rotation axis of the Bloch vector to be tilted out of the equatorial plane. Additionally, we find that for $\varphi = \pi/2$ the rephasing efficiency is worse than for $\varphi = 0$.

The position of the axis of rotation (more specifically, its projection onto the equatorial plane) is given by the phase of the applied pulse. In the simplest case, the rephasing sequence consists of 8 equal pulses (Carr-Purcell-Meiboom-Gill, CPMG scheme) [90, 91]. As we saw, the rephasing efficiency of a CPMG sequence suffers from pulse errors and depends on the phase of the initial state.

To overcome such problems, already decades ago composite pulse sequences with pronounced robustness to fluctuations of experimental parameters were developed in NMR [55, 92]. The basic idea is to change the phases of the consecutive pulses.

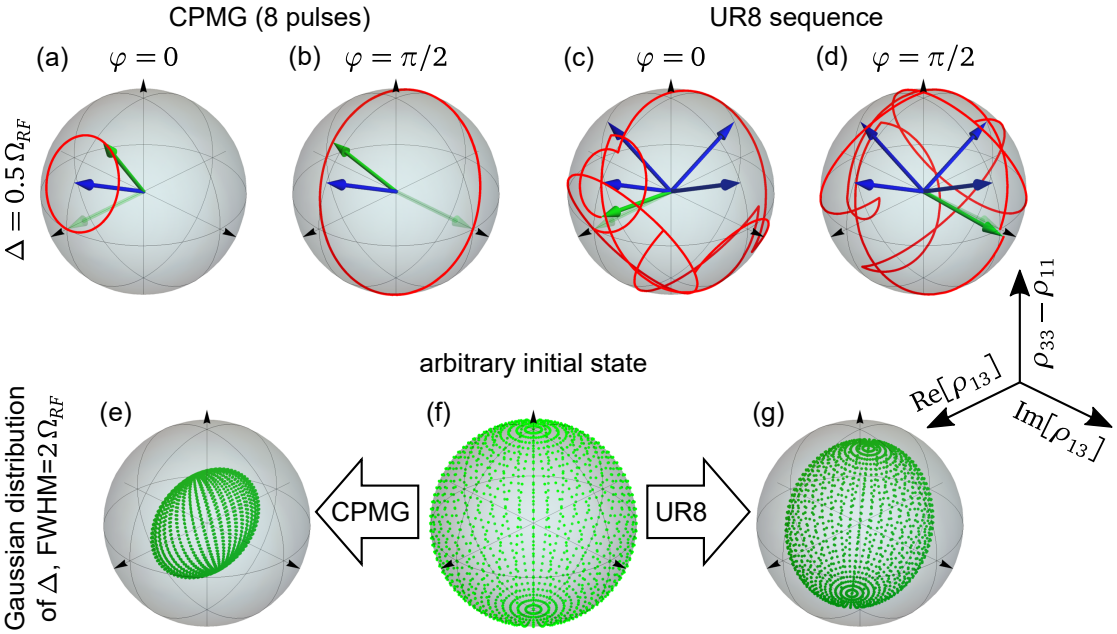

Figure 5.7: Comparison of Bloch spheres for CPMG and UR8 rephasing sequences for different initial states (indicated by the different values φ). (a)–(d) We consider pulses with a detuning of $\Delta = 0.5\,\Omega_{RF}$ and calculate their action on states with maximal coherence ($\theta = \pi/2$) but different complex phase φ of the density matrix element ρ_{13}. We ignore free evolution of the states. The initial and final Bloch vectors are represented by the faint and solid green arrows, respectively. The red lines shows the path of the Bloch vectors during the application of the pulse sequence. (a) During application of a CPMG sequence, the Bloch vector rotates on a circle (red) around axis indicated in blue and after 8 pulses it ends in a state different from the initial state. (b) For a different initial state, the final Bloch vector is almost opposite to the initial one. (c)–(d) The different phases of the pulses in the UR8 sequence cause a complicated path of the Bloch vector (red), designed to compensate pulse errors. The initial and final Bloch vectors almost coincide, indicating the high error compensation capability of the UR8 sequence. (e)–(g) We consider a Gaussian distribution of detunings with $\mathrm{FWHM} = 2\,\Omega_{RF}$ and calculate the final Bloch vectors (dark green dots) for many different initial Bloch vectors [light green dots in (f)] after application of a CPMG (e) and UR8 (g) sequence, each containing 8 rephasing pulses. (e) The rephasing efficiency of CPMG is well below 1 (indicated by the final Bloch vectors not lying on the surface of the Bloch sphere). Additionally, different states have different rephasing efficiency (note the prolate shape of the surface spanned by the darker green points). (g) The UR8 sequence has a higher rephasing efficiency than the CPMG sequence and the efficiency does depend less on the initial state.

This enables manipulation of the path of the Bloch vector during the sequence of pulses. By choosing paths that are insensitive to specific pulse parameters, it is possible to design sequences that give a high rephasing efficiency despite errors of the constituting pulses. We note that also the temporal shape of the pulses' amplitude and detuning can be exploited to improve their rephasing efficiency, e.g., by using rapid adiabatic passage [93] or single-shot shaped pulses [94]. However, in our setup, rectangular pulses with constant frequency are easily implemented and shaped pulses can still be combined with phased sequences to further improve the rephasing efficiency.

There is a multitude of robust sequences, many of which compensate pulse errors only in one or two parameters [50, 57]. In our experiments, we apply a new UR

sequence that compensates pulse imperfections in any parameter [57]. This sequence was developed by G. Genov in cooperation with our theory partner N. V. Vitanov[1]. The UR sequences are designed to minimize the error of the whole sequence by means of the constituting pulses' phases. Error compensation can be achieved for any even number of pulses n and the order of error compensation grows linearly with n. Compared to other composite sequences, e.g., the KDD in XY4 sequence (which is often considered the state-of-the-art), this enables a higher error compensation for the same number of pulses n [57]. Theory shows that the error compensation of UR sequences increases with the number of pulses. However, the total duration of the UR sequence, which relies on coherent interaction, must be short compared to the coherence time or changes in the environment. Hence, the number of pulses is the sequence is limited. In the experiment we must find a compromise between sufficient error compensation (which means large n) and sufficiently short total interaction time (which means small n).

Figures 5.7(c) and (d) show the evolution of two different initial states when we apply a UR8 sequence with detuned pulses. Using appropriate phases (see [57]), the rotation axis changes from pulse to pulse leading to a complicated path of the Bloch vectors. Despite the rather large pulse error, the final Bloch vectors show only a minor deviation from the respective initial Bloch vector for both initial states. This illustrates the capability of the UR sequences to compensate even large pulse errors.

When we generate the coherence by EIT light storage with almost counterpropagating control and probe beams, the phase and amplitude of the initial coherence (described by the spin wave) varies strongly within the storage medium (see Section 1.1). This means that the rephasing sequence must achieve a high rephasing efficiency for an arbitrary initial state. In Figure 5.7(f) we consider Bloch vectors (depicted by the green dots) spread over the whole sphere, representing many different initial states. We simulate the action of a CPMG and a UR8 sequence, each with 8 pulses, on each of the Bloch vectors. To emulate the situation in our experiment, we consider a Gaussian distribution of detunings with FWHM $= 2\,\Omega_{RF}$.

Figure 5.7(e) shows the final states after application of the CPMG sequence. The magnitude of the Bloch vectors (i.e., the distance of the points from the origin) is significantly reduced compared to the initial state which indicates a low rephasing efficiency. Moreover, the final Bloch vectors have different magnitude (note the prolate shape) which means that the rephasing efficiency depends on the initial state. States with large $|\mathrm{Re}[\rho_{13}]|$ are rephased with higher efficiency than other states. When we apply many pulses, this leads to a projection of an arbitrary state onto the $\mathrm{Re}[\rho_{13}]$-axis. This is known as spin locking and impedes faithful storage of an arbitrary state. However, EIT light storage of a single probe pulse in a counterpropagating setup (or generally, when the medium length exceeds the wavelength of the spin wave) leads to different superposition states $|\psi\rangle$ at different positions (according to the spin wave). This is due to the locally different relative phase and amplitude of the control write and probe pulses (see Section 1.1 and [45]). Therefore, an arbitrary probe pulse can still be stored and rephased using a CPMG sequence, but the CPMG sequence will only rephase coherences at very few positions (i.e., for specific phases φ) efficiently. During readout, the signal is built from the coherences of very few ions

[1] St. Kliment Ohridski University of Sofia

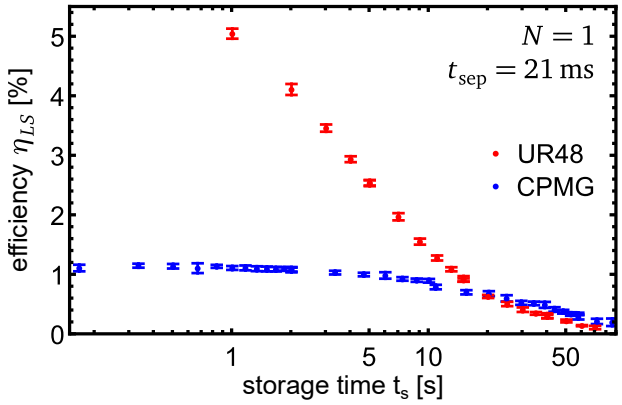

Figure 5.8: Experimental light storage efficiency η_{LS} versus storage time t_s in single pass configuration at the ZEFOZ point. We compare a CPMG (blue) and a UR48 (red) sequence for rephasing. The π pulse separation is $t_{\text{sep}} = 21\,\text{ms}$ in both cases.

(in the case of Pr:YSO) leading to low storage efficiency. Furthermore, once the states are projected, CPMG can rephase the remaining signal very efficiently. Over time this means that the signal will first decrease rapidly during the projection process and then slowly due to the high rephasing efficiency for for the projected state.

In contrast, when we apply the UR8 sequence [see Figure 5.7(g)], the rephasing efficiency is clearly higher than for the CPMG sequence. Additionally, the dependence on the initial state is reduced, proving the superiority compared to the CPMG sequence for rephasing of EIT light storage signals. The higher rephasing efficiency and reduced spin locking effect is especially useful to reduce the effects of the pulse errors when we apply many pulses to prolong the storage time.

To compare the rephasing efficiency of the CPMG and UR sequences, we apply them for rephasing an atomic coherence created by EIT light storage at the ZEFOZ point. We store a rectangular probe pulse with 5 µs duration and 10 µW power and obtain an efficiency of 7.2% for storage over 2 µs (i.e., without applying rephasing pulses). Figure 5.8 shows the measured efficiency versus the storage time when we apply a CPMG or a UR48 sequence for rephasing. With the CPMG sequence, we achieve a maximum efficiency of 1.1% which corresponds to a rephasing efficiency of only 15%, limited by pulse errors. In contrast, using the UR48 sequence, we achieve a fivefold enhancement of the light storage efficiency compared to the CPMG sequence at a storage time of $t_s \approx 1\,\text{s}$. This proves the superior robustness of the UR sequence to pulse errors. Only at long storage times $t_s \geq 20\,\text{s}$, the CPMG sequence gives a higher efficiency. This is due to the spin locking effect present for the CPMG sequence. For specific phases, the rephasing efficiency is close to unity which leads to a relatively high light storage efficiency at long storage times. In contrast, the UR48 sequence has a high rephasing efficiency for all phases, however the efficiency is lower than that of the CPMG sequence for the specific phases. Therefore, the CPMG sequence outperforms the UR48 sequence at long storage times.

5.4 Optimizing Rephasing at the ZEFOZ Point

In the previous section, we presented UR DD sequences that compensate imperfections of the rephasing pulses and maintain high efficiency despite a large number of imperfect pulses. While a high order n of a UR sequence is beneficial for the error compensation, the sequence duration should be kept short compared to the

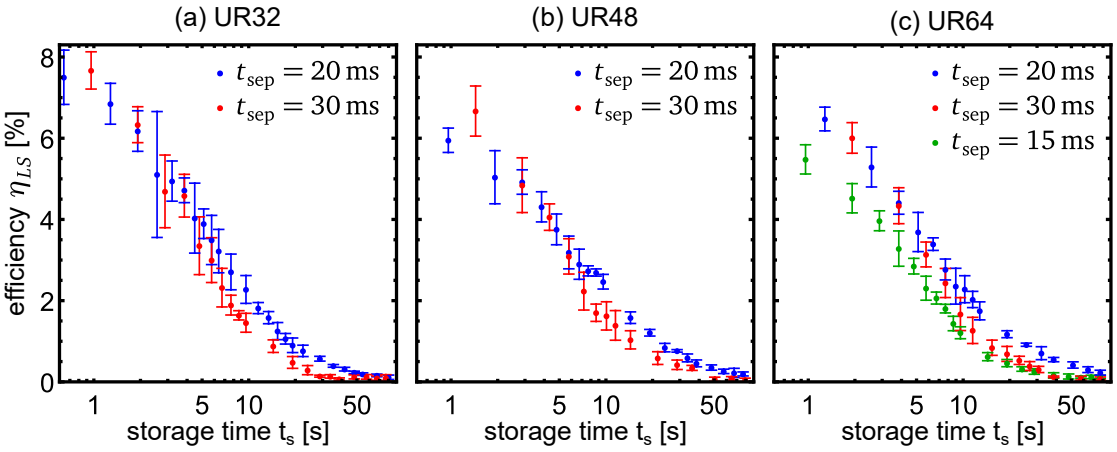

Figure 5.9: Light storage efficiency η_{LS} versus storage time t_s at the ZEFOZ point in double pass configuration. We compare UR sequences with different order, i.e., UR32 (a), UR48 (b), and UR64 (c) sequences and with different separation time t_{sep} of the π pulses for rephasing. For most storage times and all sequences, $t_{sep} = 20$ ms (blue) separation gives the highest efficiency.

decoherence time T_2 in order to maintain the phase information of the constituent pulses. As we saw in Section 5.1, the time separation of the π pulses t_{sep} should not be lower than ~ 10 ms in order to ensure high readout efficiency. Considering $T_2 \approx 1.75$ s, this limits the applicable UR order to $n \lesssim 175$ in our experiment.

For an optimization of the rephasing sequence, i.e., the parameters t_{sep} and n, we perform EIT light storage at the ZEFOZ point in the double pass configuration and measure the light storage efficiency for different storage times. We achieve storage times longer than one cycle of a rephasing sequence by successively applying several (identical) sequences. This ensures continuous application of equally separated π pulses as required for DD. Figure 5.9 shows the result of these measurements for different order n and time separation t_{sep}. We find only minor differences between the decays of the light storage signal for the different sequences. The $1/e$ decay time is $t_s \approx 6$ s for all sequences. This is longer than the T_2 time determined with rephasing by two π pulses, i.e., 1.75 s, and shows the effect of DD. However, the limitation of the π pulse separation time (compare Section 5.1) hinders a more significant improvement of the storage time (as it was seen in previous work [18]). We reach the highest efficiency $\eta_{LS} = (7.7 \pm 0.5)\%$ at $t_s = 960$ ms using the UR32 sequence [see Figure 5.9(a)] with $t_{sep} = 30$ ms pulse separation. However, this is mainly due to the short storage time which most of the higher order sequences cannot reach (due to the larger number of constituent pulses). Considering the efficiency of 19% for 2 µs storage, i.e., without rephasing, the rephasing efficiency is $\eta_r \approx 40\%$. This is almost a threefold increase compared to the rephasing with two π pulses (compare Section 5.1) and demonstrates the high error compensation capability of the UR sequences. When we compare the efficiency for the different t_{sep}, we find that sequences with $t_{sep} = 30$ ms are slightly superior to the ones with shorter t_{sep} when we apply only one cycle of the sequences [compare the first red data point to the blue ones in Figure 5.9(a) and (b)]. Though, at higher number of cycles, i.e., longer storage times, $t_{sep} = 20$ ms consistently gives the highest efficiency. Therefore, we continue our investigation by comparing different UR sequences (with varying

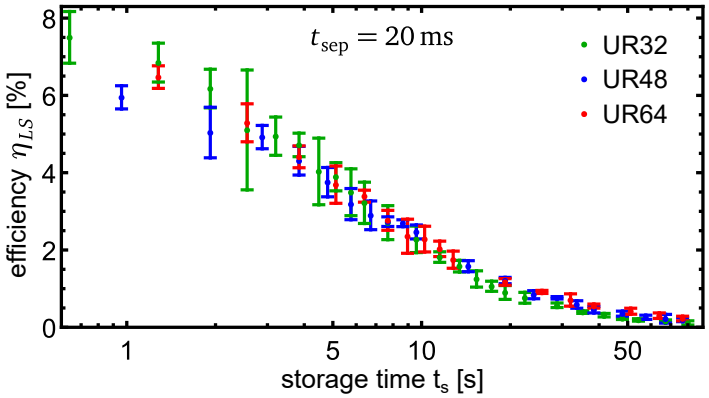

Figure 5.10: Comparison of different UR sequences with pulse separation $t_{sep} = 20\,ms$ at the ZEFOZ point: Light storage efficiency η_{LS} versus storage time t_s.

order n) with the same pulse separation $t_{sep} = 20\,ms$.

Figure 5.10 shows the light storage efficiency η_{LS} over the storage time when we use UR sequences with different orders but equal pulse separation. The difference between the sequences is only marginal. For $t_s \lesssim 3\,s$, the UR32 and UR64 sequences perform slightly better than the UR48 sequence and at longer storage times $t_s \gtrsim 10\,s$, the UR64 sequence gives a little higher η_{LS} than the other sequences.

From the similar behavior of all sequences we conclude that the pulse errors are already mostly compensated using the UR32 sequence. The additional error compensation of higher order sequences is almost canceled by the larger effect of decoherence during longer sequences. The slightly worse efficiency of the UR48 sequence, i.e., with intermediate order, compared to the other sequences, is due to higher order error compensation effects (i.e., better error compensation than expected for the order n) present in the UR32 and UR64 sequences leading to a superior efficiency of those sequences. In conclusion, our experiments show that for the pulse errors in our setup, a UR64 DD sequence with 20 ms pulse separation gives the highest efficiency up to storage times of $t_s = 80\,s$.

In this chapter, we discussed our optimizations for efficient light storage on a long timescale of tens of seconds. We presented that the preparation of an absorption plateau instead of a narrow peak increases the light storage efficiency. By applying an iterative pulse shaping algorithm and the multipass setup, we further increased the efficiency to 11% in the single pass configuration. In our setup, the double pass setup represents the best compromise between a high efficiency of 19%, low transmission losses and a long coherence time of 1.8 s. Furthermore, we found optimal rephasing pulse parameters and adapted the parameters of a robust DD sequence to maximize the efficiency in our experimental setup. When we apply DD, we have to consider a frequency shift reducing the readout efficiency for pulse separations below $\sim 10\,ms$. Although this is a significant limitation for DD, we achieved a storage time of $T_2 \approx 6\,s$ using a UR64 sequence with 20 ms time separation. This is the first time, a UR sequence with order $n > 20$ has been applied. The rephasing efficiency was about 40% which is almost a threefold increase compared to a rephasing based on two π pulses. In the next chapter, we will exploit this high efficiency to store weak coherent pulses on the timescale of several seconds.

Chapter 6

Storage of Weak Coherent Pulses With Prolonged Storage Time

In the previous chapters, we presented the implementation of ZEFOZ and DD for increasing the light storage time as well as the optimization of the setup to reach maximal efficiency for storage of classical pulses. Now, we utilize the high efficiency at long storage times and reduce the energy of the stored probe pulse to the few-photon level. In solid state media, storage of weak coherent pulses on the few-photon level was previously limited to a storage time of 1 ms [21] and in a single rubidium atom, a storage time of 100 ms was achieved [95]. In this chapter, we present the storage of weak coherent pulses with storage times exceeding one second which pushes the state-of-the-art by more than one order of magnitude. This requires adapting the spectral filter to the modified parameters at the ZEFOZ point.

6.1 Filter Setup for Storage at the ZEFOZ point

The goal of this work was to reduce the energy of the stored probe pulse to the few-photon level at storage times in the range of seconds. In order to reach such a long storage time, we use the ZEFOZ technique. However, when we apply the magnetic field required for ZEFOZ, the level structure of Pr:YSO changes significantly compared to the case without a magnetic field (compare Section 4.2). As a consequence, we need to adapt the frequency of the control pulses. Since the control read pulse is the main contribution to the optical background, this means that we need to adjust the preparation sequence of the filter crystal. Furthermore, due to the reduced storage efficiency at the ZEFOZ point, we want to achieve an even better background noise suppression than presented in Chapter 3 in order to maintain operation at the single photon level. In this section, we present an extension of the preparation sequence for the filter crystal and the results obtained in a multipass filter setup leading toward this goal.

6.1.1 Preparation of the Filter Crystal for Storage at ZEFOZ

Light storage under ZEFOZ conditions requires a different preparation of the filter crystal. In particular, the lower frequency difference between the pass- and the stopband which must coincide with the probe and control read pulse frequencies, respectively. By definition, we keep the relative probe frequency at $\nu_p = 0\,\mathrm{MHz}$ and the level structure at the ZEFOZ point implies the frequencies of the control pulses, i.e., write and read pulses, $\nu_c = -7.3\,\mathrm{MHz}$. Figure 6.1 gives an overview over the optical preparation sequence for the filter crystal which we adapted to the new requirements. We show the EIT coupling scheme in the modified level structure in (a). In (b) to (d), we show how the different preparation steps redistribute the

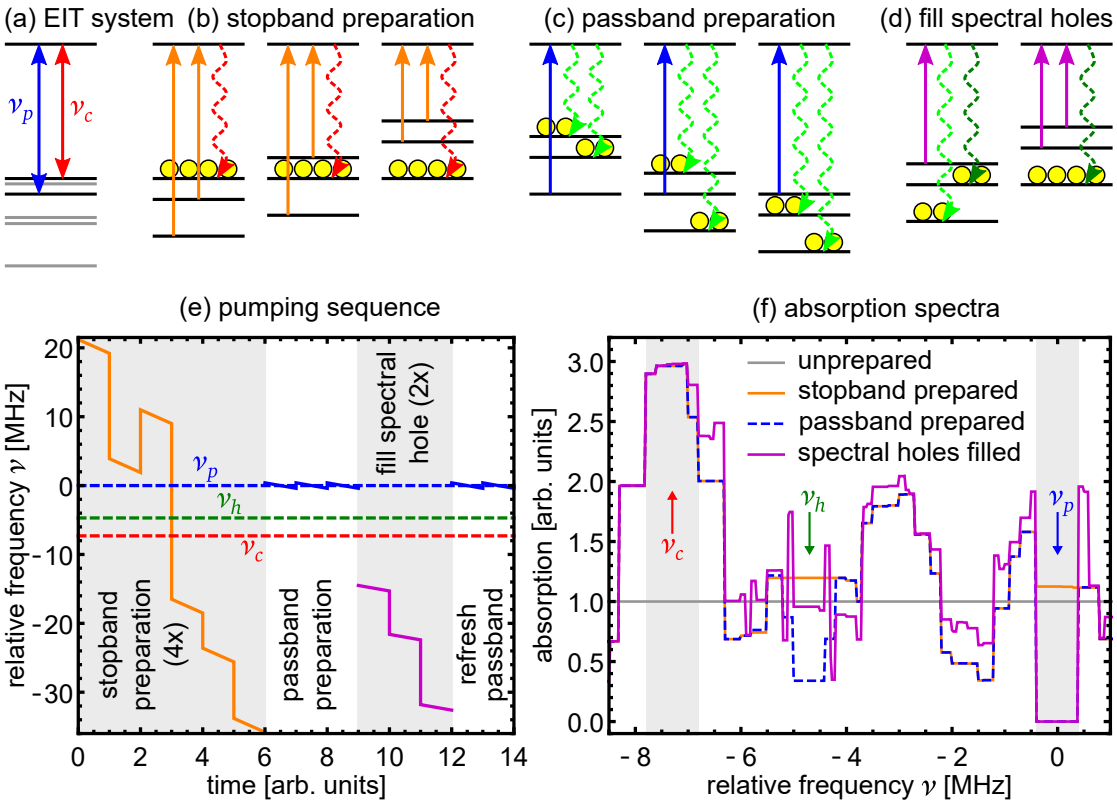

Figure 6.1: Preparation scheme of the filter crystal for EIT light storage at the ZEFOZ point $\vec{B}_0$. For simplicity, we consider only a single optically excited state in (a) to (d). (a) EIT coupling scheme at $\vec{B}_0$. The magnetic field splits and shifts the ground states (lower black and gray lines, black lines represent the ground states for EIT). This leads to a reduced frequency difference between the probe (blue) and control (red) pulses. (b) Optical pumping of the filter crystal at six frequencies prepares the population in the ground states and maximizes the absorption at ν_c, i.e., prepares the stopband. (c) Pumping at the probe frequency ν_p pumps the population into other ground states creating the passband. (d) We fill selected spectral holes created in the previous steps (only one shown) by optical pumping similar to the stopband preparation. To avoid the creation of new spectral holes in the vicinity of ν_c, we perform pumping only at three frequencies. (e) Frequency of the preparation pulses over time. For each optical pumping frequency, we perform a chirp (see falling slopes at each time step). First, we repeat the stopband preparation (orange) four times (only the first repetition is shown). In the first two repetitions, the chirps have a width of 2 MHz in order to prepare a wide stopband, though not at maximal absorption, and the last two repetitions (not shown) use a chirp width of 1 MHz. Next, we perform three 800 kHz wide chirps centered at ν_p to create the passband (blue, solid graph at time units 6 to 9). Then, for each spectral hole to be filled (shown only for one at ν_h), we first perform two repetitions of three chirps which prepare absorption in an 800 kHz wide range around the hole's center. Then, we perform two chirps centered at ν_p to reestablish transmission in the passband. All the latter chirps have a width of 800 kHz in order to prepare broad spectral features and to avoid pumping of population in a circular process (which would happen for broader chirps). (f) Simulated absorption versus frequency after the different preparation steps. In the unprepared medium, the absorption is 1 for all frequencies (gray). After the preparation of the stopband (orange) we find an absorption plateau centered at ν_c. After the passband preparation (dashed, blue graph), we see a narrow spectral pit around ν_p. However, we also find other, though not fully transparent, spectral pits and holes, e.g., at ν_h. In the last preparation step we fill these holes (purple graph), providing a filter spectrum with only one dominant passband at ν_p.

population. To facilitate presentation, the depicted level schemes are simplified, i.e., we only consider one of three optically excited states. We illustrate the time sequence of the preparation in (e) and in (f) we present the simulated absorption spectra at different stages of the preparation (considering the full level scheme of Pr:YSO).

Unlike the storage crystal, the filter crystal is not exposed to the ZEFOZ field. This means that, in contrast to the field free case (see Chapter 3), the level schemes of the two crystals are different. Still, the basic idea for tailoring the absorption spectrum presented in Section 3.1 remains unchanged for storage at the ZEFOZ point. As a first step, we prepare the stopband at the control frequency ν_c [Figure 6.1(b)], followed by the passband preparation. The resulting spectrum with the prepared passband [dashed, blue line in Figure 6.1(f)] exhibits additional, though not fully transparent, transmission windows apart from the relevant one for EIT at ν_p, e.g., around $\nu_h = -4.7\,\mathrm{MHz}$. As we will see later, these partially transparent spectral regions become an obstacle when we try to reach maximal absorption of the control read pulse background. Therefore, we eliminate the spectral holes centered at $-19.7\,\mathrm{MHz}$, $-4.7\,\mathrm{MHz}$, $3.3\,\mathrm{MHz}$, and $4.8\,\mathrm{MHz}$ by optical pumping at appropriately chosen frequencies.

Figure 6.1(d) shows the pumping scheme for filling one of the spectral holes, i.e., increasing the absorption, at $\nu_h = -4.7\,\mathrm{MHz}$. We choose the pumping frequencies as if we were to prepare a second stopband. However, we use only three of the six pumping frequencies in order to avoid creating new spectral holes too close to ν_c. Finally, we refresh the passband preparation since the optical pumping used to fill the spectral holes might have deteriorated the transmission. The purple line in Figure 6.1(f) shows the simulated absorption spectrum after all preparation steps. The stopband around $\nu_c = -7.3\,\mathrm{MHz}$ is still highly absorbing and the absorption at the higher frequency end is increased by the hole filling step (compare purple line to the dashed, blue line between -7.0 and $-6.5\,\mathrm{MHz}$). As intended, the absorption of the spectral hole at ν_h is significantly higher (almost tripled) and, as a positive side effect, the absorption in the region from -2.2 to $-1.2\,\mathrm{MHz}$ is also increased. At the same time, the passband is still perfectly transmissive.

6.1.2 Influence of the Filter Crystal's Dopant Concentration

When we apply the filter preparation sequence to a Pr:YSO crystal, the absorption will depend on the length and dopant concentration of the crystal. Sabooni *et al.* showed that in Pr:YSO the achievable absorption is not always proportional to the crystal length [86]. This is due to a birefringence induced rotation of the polarization and a lower absorption coefficient for the rotated polarization. Furthermore, as explained in Section 1.2, a higher dopant concentration will only lead to a minor increase in OD. However, the inhomogeneous linewidth of the optical transition Γ^e increases with higher dopant concentration. As we will see later, higher Γ^e is beneficial for high absorption of the stopband. In previous work [37], an increase from $\Gamma^e = 2\pi \times 7\,\mathrm{GHz}$ to $\Gamma^e = 2\pi \times 280\,\mathrm{GHz}$ has been observed for a change in dopant concentration from 0.05% to 1%. These effects show that the optimization of crystal length and dopant concentration for a filter crystal is nontrivial when we cannot choose the two parameters freely (as we are restricted to a limited number of available samples). In this section, we investigate the filter performance of two

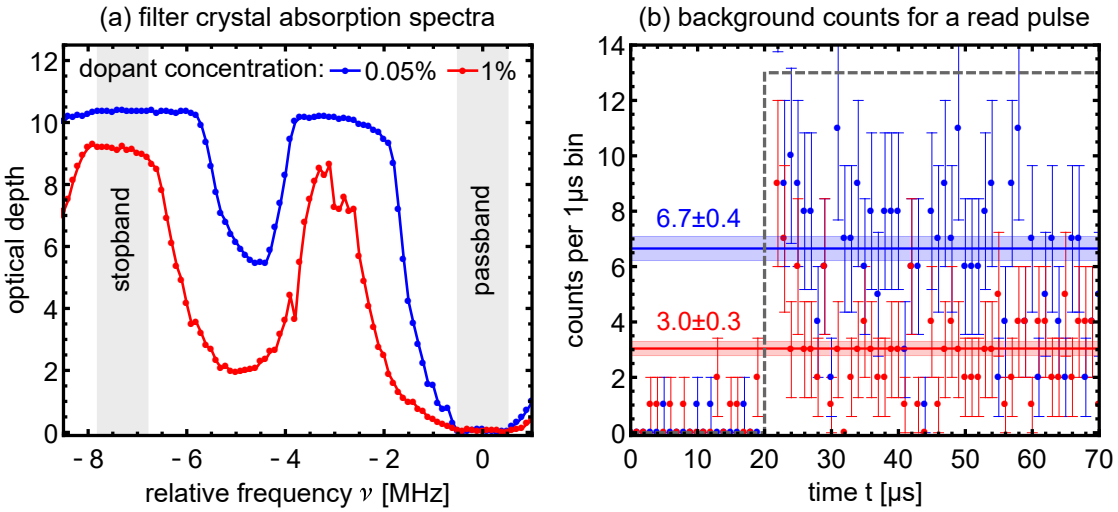

Figure 6.2: Characterization of the filter crystals with different dopant concentration in a single pass ($N_f = 1$) using the preparation sequence for EIT storage at the ZEFOZ point. Here, we prepared a 1 MHz wide passband and omitted the filling of spectral holes. (a) Absorption versus frequency of the crystals with 0.05% (blue) and 1% (red) dopant concentration. We use the SPCM for detection and different ND filters (at different frequencies) to avoid detector saturation at frequencies ν with high transmission. We corrected the OD for the effect of the ND filters using correction factors (i.e., the attenuation of the ND filters) determined at frequencies with intermediate absorption (in the filter crystal) where we used more than one ND filter. For each ν we sum the photon counts of the transmitted pulse over 10 repetitions. At all frequencies outside the passband, the 0.05% doped crystal has a higher OD. In the stopband we measure $\mathrm{OD} = 10.4$ for the 0.05% doped crystal and $\mathrm{OD} = 9.1$ for the 1% doped crystal. (b) Background counts versus time for a control read pulse with 50 mW power starting at $t = 20\,\mu\mathrm{s}$ (indicated by the gray, dashed line) summed over 500 repetitions for each of the filter crystals. After turning on the control read pulse, the counts spike to roughly 1000 (not shown) and settle down after 2 µs, i.e., at $t = 22\,\mu\mathrm{s}$. The average number of counts for $t \geq 22\,\mu\mathrm{s}$ is 6.7 ± 0.4 for the crystal with 0.05% dopant concentration and 3.0 ± 0.3 for the 1% doped crystal (see blue and red lines with shaded areas indicating the uncertainty range).

Pr:YSO crystals[1], one with 10 mm length and 0.05% dopant concentration and the other one with 3 mm length and 1% dopant concentration, referred to as the crystal with low and high dopant concentration, respectively.

First, we measure the absorption spectrum of the filter crystals in a single pass, i.e., for $N_f = 1$, after application of the preparation sequence. We use a weak pulse with 100 nW power and 100 µs duration, i.e., with a pulse area $\Omega_p \tau \approx 0.2\pi$, for probing the absorption at different frequencies. The duration is long enough to ensure a Fourier bandwidth smaller than the linewidth of the OPO system and we set the power (and consequently the pulse area) low enough to avoid optical pumping. We define full transmission via the measurement with maximal photon count. Thereby, we automatically account for any losses of the optical setup.

Figure 6.2(a) shows the absorption spectra for the two different filter crystals. In this early experiment we omit the last preparation step of filling additional spectral holes. The OD of the crystal with low dopant concentration is higher for all frequencies outside the passband. In the stopband the average OD is 10.4 and 9.1 for the

[1] Scientific Materials

low and highly doped crystal, respectively. The difference in OD corresponds to a 3.5 times higher absorption of the crystal with low dopant concentration indicating the crystals superiority. This counterintuitive result can be explained by the small impact of the dopant concentration on the absorption and the larger length of the low doped crystal. This crystal is more than three times longer than the highly doped crystal. Although not all of the length contributes equally to the absorption (due to rotation of the polarization, see [86]), it still outweighs the gain in absorption by the 20 times higher dopant concentration of the other crystal. As described in Section 1.2, the main effect of the increased dopant concentration is an increased inhomogeneous linewidth rather than a higher absorption.

In order to estimate the number of background photons that leak through the filter crystals, we apply a control read pulse with $P_c = 50\,\mathrm{mW}$ power to the storage crystal. We prepare a spectral pit in the storage crystal to avoid fluorescence. Figure 6.2(b) shows the photon counts in bins of 1 µs width summed over 500 repetitions for the low doped filter crystal in blue and for the high doped crystal in red. The control read pulse (indicated by the gray, dashed line) starts at $t = 20\,\mu\mathrm{s}$. Before the control read pulse starts, we observe roughly one count per 2 µs for both datasets, i.e., independent from the choice of the filter crystal. This count rate corresponds to the dark count rate of the detector of 1000 counts per second. This shows that no additional stray light, e.g., from the laboratory lighting, couples into the single-mode fiber in front of the SPCM. At the rising edge of the control read pulse we observe a significant increase in in photon counts (not shown in Figure 6.2) up to roughly 1000. This is due to the high frequency components at the steep slope which lie outside the filter stopband. After $t = 22\,\mu\mathrm{s}$ the count rate settles to a constant value. The 2 µs long spike of background counts poses only a minor obstacle for a light storage experiment because the signals typically have a duration in the order of 10 µs. Therefore, we can ignore the first 2 µs of the signal without a huge loss of efficiency.

For our estimation of background counts we calculate the average number of counts for $22\,\mu\mathrm{s} \leq t \leq 70\,\mu\mathrm{s}$ for the low and high dopant concentration [see blue and red lines in Figure 6.2(b) with shaded areas indicating the standard deviation]. The average number of background counts is 6.7 ± 0.4 for the low dopant concentration and 3.0 ± 0.3 for the high concentration. This means that the filter crystal with high dopant concentration reduces the number of background photons from the control read pulse more than twice as good as the low doped crystal. This seems to be in contradiction to the spectroscopic measurement in which the highly doped crystal showed a lower absorption. However, in the two measurements we use completely different optical paths and power. While we use the well defined probe beam path and a power of 100 nW in the absorption measurement, the control read pulse uses the control beam path. This means that the filter crystal is illuminated only diffusely by a reflected portion of the control read pulse. The exact power of the reflected portion is not known and depends strongly on the adjustment of the optics in the storage part of our setup. This makes it impossible to directly compare the spectroscopic measurement and the measurement of control read pulse background photons. However, the latter corresponds directly to the EIT light storage experiments because it uses the control beam path for probing the suppression of the control read pulse. Therefore, we conclude that the highly doped filter crystal gives a

higher suppression under the conditions relevant for storage of weak coherent pulses. We note that a slightly different adjustment of the control beam paths used for the measurements shown in Figure 6.2(b) might have influenced the comparison of the background counts. However, we still found the tendency that the highly doped filter crystal gives a higher control beam suppression over several days of measurements, despite different alignments.

6.1.3 Influence of Spectral Holes and Double Pass Configuration on the Filter Performance

We selected the crystal with 1% dopant concentration as the filter crystal because of its superior absorption of the control read pulse. However, we did not apply the full filter preparation sequence so far, i.e., we did not fill additional spectral holes.

Figure 6.3(a) shows the spectra after application of two different preparation sequences for $N_f = 1$. For $N_f = 2$ we show the spectrum after the full preparation sequence. In the first sequence, represented by the red dots for $N_f = 1$, we only prepare 1 MHz wide pass- and stopbands and in the second sequence we lower the width of the passband to 800 kHz and fill spectral holes according to the preparation sequence described above. For $N_f = 1$ the latter sequence shows a significantly higher absorption at all frequencies outside the passband (see green data). In the stopband the OD is on average 11.5, i.e., by 2.4 higher than the OD of the first sequence. This corresponds to an 11 times higher absorption. This is a surprising result because the simulation of the absorption spectrum [see Figure 6.1(f)] shows only a minor influence on the stopband.

We explain the rather large impact of the hole filling step by a weak but spectrally broad optical background that leaks through any transmission window in the filter crystal. We suspect this background to originate from the OPO based laser system and, hence, that it is centered at the dominating optical frequency, i.e., at ν_c for the control read pulse, and that is has a width in the order of the acceptance bandwidth of the OPO-SFG crystal, i.e., of ~ 100 GHz. For frequencies different from ν_c, we expect the background amplitude to drop with spectral distance. Therefore, it is advantageous to eliminate spectral holes in the vicinity of ν_c even if this requires the creation of new spectral holes, as long as the newly created spectral holes have a bigger spectral distance to ν_c. This means that we can lower the negative effect of the spectrally broad background noise on the filter absorption by optical pumping at appropriately chosen frequencies. The contribution of a (partially transparent) spectral hole to the residual transmission of the control read pulse depends on its OD and frequency as well as the spectrum of the control read pulse. Using the simulated absorption spectrum shown in Figure 6.1(f) (dashed, blue graph) and assuming a Lorentzian lineshape of the control read pulse we calculate the contribution of each spectral hole to the total transmission. We choose a Lorentzian lineshape because it exhibits wide tails at low amplitude which fits our assumption of a broad but weak background spectrum. We find that the assumed linewidth has no qualitative impact when we sort the spectral holes with respect to their contribution to the total transmission. Based on the calculation we decide to reduce the transmission of four spectral holes centered at -19.7 MHz, -4.7 MHz, 3.3 MHz, and 4.8 MHz.

For the second sequence we also applied the multipass setup for the filter crystal

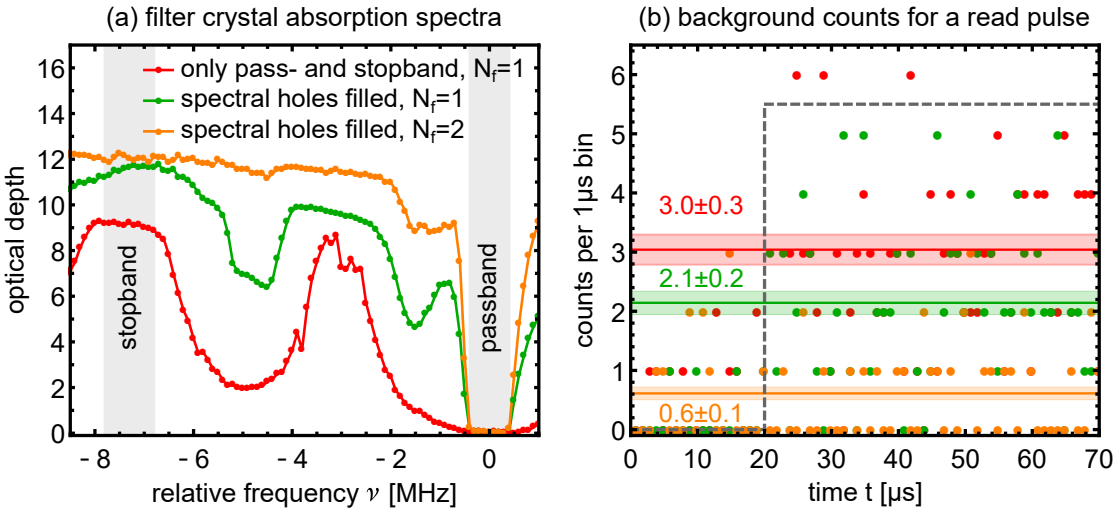

Figure 6.3: Comparison of different preparation sequences and effect of the filter double pass configuration for the filter crystal with 1% dopant concentration. (a) OD versus frequency for different configurations of the filter setup. The red data shows the spectrum when we prepare a pass- and stopband with 1 MHz width for $N_f = 1$. For the measurement shown by the green dots, we additionally fill spectral holes (see main text) and prepare the passband only with 800 kHz width. The orange data shows the spectrum when we additionally use a double pass configuration, i.e., $N_f = 2$. With each change in the configuration, i.e., adding the hole filling step and applying the double pass, the absorption increases for all frequencies outside the passband. In the stopband the average OD is 9.1, 11.5, and 12.0 for the three configurations, respectively. (b) Photon counts (summed over 500 repetitions) versus time t for application of a control read pulse with 50 mW power. The control read pulse (indicated by the gray, dashed line) starts at $t = 20\,\mu s$. The color of the dots represents the configuration of the filter setup [according to (a)]. We omit error bars for clarity reasons. The solid lines and corresponding shaded areas represent the mean number of counts and its standard deviation for $t \geq 22\,\mu s$, i.e., when the count rate has settled after the initial peak at $t = 20\,\mu s$ (not shown). When we prepare only the pass- and stopband at $N_f = 1$, the mean of the background counts is 3.0 ± 0.3. It drops to 2.1 ± 0.2 when we additionally fill spectral holes and reduce the passband width to 800 kHz. With the latter preparation and $N_f = 2$, the background counts drop to an average value of 0.6 ± 0.1.

with $N_f = 2$ passes. The corresponding spectrum [see Figure 6.3 (a)] shows a further increase in absorption. However, in contrast to the expectation of a doubled OD, in the stopband the OD only increases to 12.0, i.e., by only 0.5. The high OD of about 12 is maintained not only in the stopband but over a wide plateau. Up to $\nu = -2$ MHz, the OD drops only slightly with increasing frequency. Even in the region around $\nu = -5$ MHz, where we observe a dip in the OD for $N_f = 1$ (see green data), the absorption stays high. We explain this behavior again by a spectrally broad background of the OPO system. The actual absorption of the filter crystal is higher than determined in the spectroscopy and it comprises more structure (similar to the measurement for $N_f = 1$). However, the broad background leaking through spectral holes limits the maximal measurable OD since we will always detect photons, even for full absorption at the central frequency. For $N_f = 2$ the falling OD for increasing frequency (in the region from $\nu = -8.5$ MHz to $\nu = -2$ MHz) indicates that the background leaks through the passband at $\nu = 0$ MHz which is the only relevant

transmission window in the filter spectrum. Since full transmission of the passband is necessary, a higher suppression of the control read pulse can only be achieved by lowering the spectral width or amplitude of the broad background of the OPO system. In particular, using a higher number of passes N_f will increase the actual absorption of the stopband but as photons leaking through the passband limit the measurement, this will not improve the suppression of a pulse centered in the stopband.

For additional investigation of the different filter configurations, we apply a control read pulse with $P_c = 50\,\mathrm{mW}$ power after preparing the filter crystal and measure the background counts accumulated over 500 repetitions, see Figure 6.3(b). For $N_f = 1$ we observe an average of 2.1 ± 0.2 background counts per µs when we use the full preparation sequence (see green line). Compared to the measurement without the hole filling step (red line), this is only a reduction by 0.9 counts per µs, i.e., much less than expected from the spectroscopy. However, as we saw in the previous section, we cannot directly compare both measurements.

When we apply the double pass setup, i.e., $N_f = 2$, the average number of background counts drops to 0.6 ± 0.1 which is just above the number of detector dark counts of 0.5. This is a significant improvement over the single pass setup, however we also have to consider that the overall transmission of the filter setup drops when we increase the number of passes. A reduced transmission also impacts the signal pulse and we should avoid it if possible. We measure the transmission of the filter setup, i.e., from the exit of the storage setup to the SPCM (this includes coupling into the single mode fiber), and obtain $\mathcal{T}_f = (40.9 \pm 0.8)\%$ for $N_f = 1$ and $\mathcal{T}_f = (19.1 \pm 0.7)\%$ for $N_f = 2$. Since the reduction in background count rate is a factor of 3.5 when changing $N_f = 1$ to 2, the increased absorption of the filter crystal outweighs the loss in transmission of about 50%. As explained above, increasing N_f further will not increase the absorption anymore (due to photons leaking through the passband), so $N_f = 2$, i.e., a double pass, represents the optimal filter setup.

In this section, we presented the optimization of the filter setup for EIT light storage at the ZEFOZ point by choosing the filter crystal with the highest control read pulse suppression, extending the preparation sequence and optimizing the number of passes through the filter crystal. Using a 3 mm long Pr:YSO crystal with 1% dopant concentration, a preparation sequence that includes additional pumping to fill undesired spectral holes and a double pass configuration, we reduced the background count rate during the control read pulse to 0.6 counts per µs in 500 repetitions, or equivalently to $1200\,\mathrm{s}^{-1}$. For a 12 µs long integration gate [compare the signal pulse shown in Figure 6.4(b)] this means 0.014 background counts. Considering the efficiency and transmission of our setup, we expect this to be low enough to detect the signal when storing weak coherent pulses at the ZEFOZ point.

6.2 Storage of Weak Coherent Pulses at ZEFOZ

Above we found the optimal parameters for our spectral filter to permit EIT light storage of weak coherent pulses at the ZEFOZ point. We proceed now to the main goal of our work, i.e., storage of light pulses at the few-photon level on the timescale of seconds. First, we explore the limitations of our setup regarding the minimal

photon number, though still at a rather short storage time. Then, we present our results for storage of weak coherent pulses with a mean photon number down to less than 10 photons, at storage times in the regime of seconds. Our results presented here are part of a manuscript that we prepared for publication.

6.2.1 Storage of Weak Coherent Pulses at the ZEFOZ Point Without Rephasing

In the first stage of our experiments on EIT light storage of weak coherent pulses, we work at a storage time of 2 µs, without rephasing and without the static magnetic fields required for ZEFOZ (see Chapter 3). The aim is to demonstrate storage of pulses with as low as possible mean photon number in our Pr:YSO crystal and, thus, to pave the way toward storage of few-photon pulses also under ZEFOZ conditions.

We apply the double pass configuration of the storage setup, i.e., $N = 2$, set $\vec{B}$ using the gradient descent algorithm and optimize the probe pulse shape with the iterative algorithm (as described in Section 5.2). We choose a short storage time $t_s = 2\,\mu s$ well below the dephasing time $T_2^* \approx 10\,\mu s$, such that we do not require rephasing pulses. This enables the characterization of the filter setup under experimental conditions without unnecessarily rendering the light storage complicated.

Figure 6.4(b) shows the probe and signal pulses for storage of $\bar{n} = 10.2$ photons using $N_f = 2$. Using only the bins in the integration window, the efficiency is $\eta_{LS} = (15.8 \pm 1.9)\%$ and the SNR $= 1.3 \pm 0.2$. In the integration window the average number of background counts is 12 per bin which corresponds to 9600 s^{-1},

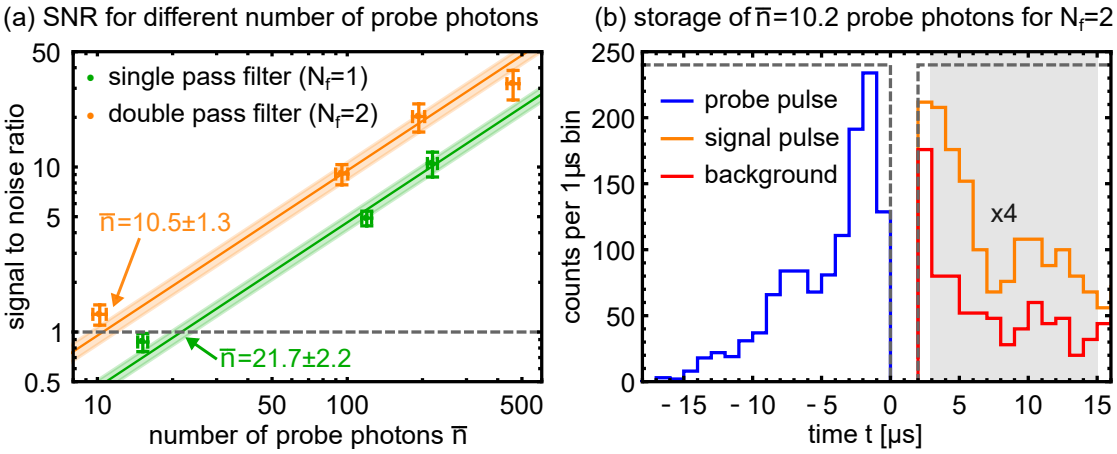

Figure 6.4: Storage of weak coherent pulses for 2 µs at the ZEFOZ point. (a) SNR versus $\bar{n}$ for the filter in single (green) and double pass (orange) configuration. The colored lines show linear fits to the data with uncertainties represented by the shaded areas. From the fits we find that we reach the threshold of SNR $= 1$ (gray, dashed line) at $\bar{n} = 21.7 \pm 2.2$ or $\bar{n} = 10.5 \pm 1.3$ for $N_f = 1$ or 2, respectively. (b) Photon counts versus time for storage of $\bar{n} = 10.2$ probe photons for $N_f = 2$ and accumulated over 1250 repetitions [corresponding to the leftmost data point in (a)]. We store and read the probe pulse (blue) using control pulses with 15 mW power (gray, dashed line). The obtained signal pulse (orange) and background (red) are integrated from $t = 3\,\mu s$ to $t = 15\,\mu s$ (gray shaded area). The efficiency is $\eta_{LS} = (15.8 \pm 1.9)\%$ and the SNR $= 1.3 \pm 0.2$. For presentation purposes, we magnify signal and background by a factor of 4.

considering the accumulation over 1250 repetitions. This is significantly higher than during the characterization in the previous section although the control read pulse power of $P_c = 15\,\mathrm{mW}$ is lower. We explain this discrepancy by the daily fluctuations of the beam alignment (note that the alignment of the control beam has a big impact on the number of photons that are strayed into the probe beam path) and the different preparation of the storage crystal. For the filter characterization we prepared a 10.5 MHz wide spectral pit in the storage crystal while for EIT light storage at the ZEFOZ point the pit at ν_c is only 300 kHz wide. Therefore, the broad spectral components of the control read pulse might pump significantly more population in the light storage experiment which will cause fluorescence. Nevertheless, the background level in our light storage experiment is low enough for the detection of a signal on the few-photon level.

Now we change the number of stored probe photons $\bar{n}$ and characterize the limitations of our setup. Figure 6.4(a) shows the SNR for different $\bar{n}$ obtained with the filter in a single pass and a double pass configuration. For similar $\bar{n}$, we consistently achieve higher SNR in the double pass configuration which matches the investigation of the filter setup in the previous section. We perform a fit of a linear function to each of the two data sets. We fix the function to SNR $= 0$ at $\bar{n} = 0$ since the definition of the signal includes the subtraction of background counts obtained for $\bar{n} = 0$. The fitting algorithm includes weighting of the data according to the uncertainties of both the SNR and $\bar{n}$ [96]. In Figure 6.4(a) we show the fitted functions and their uncertainty for both configurations. The data points clearly follow the linear fit which confirms a linear behavior of our memory, i.e., the number of signal photons is proportional to the number of probe photons, and a constant background level. The number of probe photons at which the fitted functions reach SNR $= 1$ [gray, dashed line in Figure 6.4(a)] indicates the performance of the filter setup. In single pass configuration, this threshold is reached at $\bar{n} = 21.7 \pm 2.2$ and in double pass configuration at $\bar{n} = 10.5 \pm 1.3$. This improvement by about a factor of 2 fits our expectation based on a reduction of background photons by a factor of 3.5 and a loss in transmission by a factor of 2.

Comparison of the threshold of $\bar{n} = 21.7$ for SNR $= 1$ to our results on single photon storage without ZEFOZ (see Figure 3.5) shows that we now require roughly 60 times more probe photons under ZEFOZ conditions to obtain a similar SNR when using the filter crystal in a single pass configuration. This is due to the lower storage efficiency (by a factor of 3) at the lower OD under ZEFOZ conditions and due to the reduced control suppression at the smaller frequency difference $\nu_p - \nu_c$ caused by the spectrally broad background of the OPO laser system (compare Section 6.1). The value $\bar{n} = 10.5$ means that the background level in our experiment is still an order of magnitude too high (or, equivalently, the transmission too low) for actual storage at the single photon level. Still, it proves that the filter setup enables EIT based storage of weak coherent pulses even under the less favorable conditions at the ZEFOZ point.

6.2.2 Storage of Weak Coherent Pulses on a Second Timescale

In the last stage of our experiments on light storage of few-photon pulses, we apply ZEFOZ and DD (involving our robust and efficient pulse sequences) to considerably prolong the storage time. We use a double pass configuration for the storage and

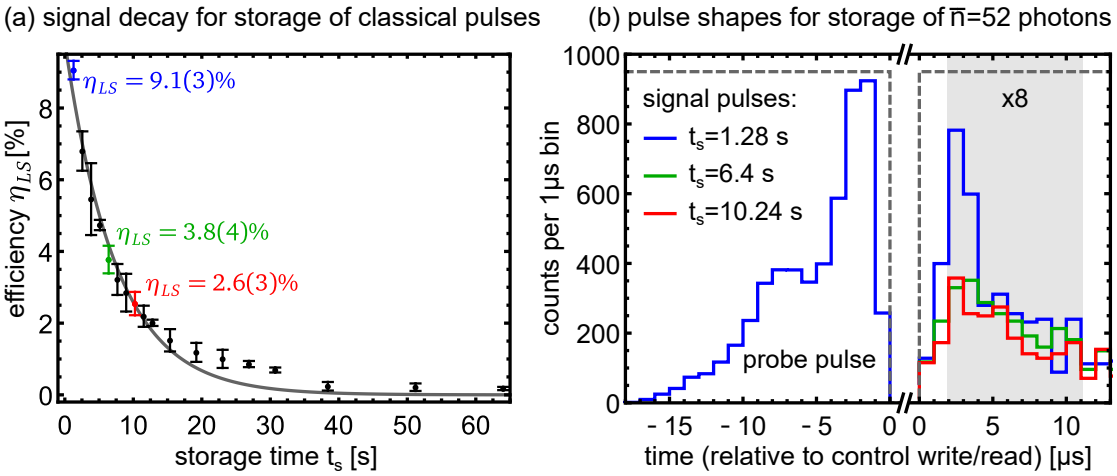

Figure 6.5: EIT light storage at the ZEFOZ point with DD using a UR64 sequence and $N = 2$ passes. (a) Efficiency η_{LS} measured with classical light pulses versus storage time t_s. The gray line represents the fitted exponential decay $\eta_{LS}(t_s) = 9.9(4)\% \exp[-t_s/7.5(4)\,\mathrm{s}]$. For the storage times indicated by the colored points, we also store weak coherent pulses with $\bar{n} = 52 \pm 2$. (b) Photon counts (in 1 µs bins) of the probe pulse (blue pulse on the left) and signals for $t_s = 1.28$ s (blue pulse on the right), 6.4 s (green), and 10.24 s (red) versus time. We accumulate the signals for $t_s = 1.28$ s, 6.4 s, and 10.24 s over 1000, 750, and 1250 repetitions, respectively. For the different storage times we determine the light storage efficiencies $\eta_{LS} = (5.6 \pm 0.4)\%$, $(3.0 \pm 0.5)\%$, and $(1.7 \pm 0.3)\%$, respectively. For better comparison, we normalize all counts to 1000 repetitions and magnify them by a factor of 8. We also show the timing of the control pulses (gray, dashed line) and the integration gate (gray shaded area) which we set to avoid integration of bins mainly containing noise while capturing about 75% of the signal.

filter setups (i.e., $N = N_f = 2$), optimize $\vec{B}$ and the probe pulse shape using the algorithms described above and achieve an efficiency of $\eta_{LS} = (20.3 \pm 0.3)\%$ for storage of classical pulses over $t_s = 2\,\mu$s. Now, we apply a UR64 sequence consisting of 64 RF π pulses with a separation of $t_{\mathrm{sep}} = 20$ ms and $\tau = 42\,\mu$s duration, i.e., $\Omega_{RF} = 2\pi \times 12$ kHz Rabi frequency. Thus, a single rephasing sequence has a duration of 1.28 s and we can increase the storage time t_s in steps of 1.28 s. Figure 6.5(a) shows the efficiency versus t_s measured with classical pulses. For $t_s = 1.28$ s the efficiency is $\eta_{LS} = (9.1 \pm 0.3)\%$ and the decay of efficiency takes place on a timescale of roughly 10 s. We perform a fit of an exponential decay (gray graph), i.e., $\eta_{LS}(t_s) = \eta_{LS}^{(0)} \exp(-t_s/T_2)$ and obtain $\eta_{LS}^{(0)} = (9.9 \pm 0.4)\%$ and $T_2 = (7.5 \pm 0.4)$ s. This means that we achieve a rephasing efficiency of almost 50% and an unprecedented storage time of 7.5 s for a memory ready to work at the few-photon level.

For selected storage times [$t_s = 1.28$ s, 6.4 s, and 10.24 s, indicated by the colored data points in Figure 6.5(a)], we store weak coherent pulses. Figure 6.5(b) shows the photon counts of the probe pulse with $\bar{n} = 52 \pm 2$ photons as well as the signal pulses after the different storage times. We can clearly distinguish the weak coherent signal pulses from the background even for the longest storage time of $t_s = 10.24$ s. From the data we determine storage efficiencies of $\eta_{LS} = (5.6 \pm 0.4)\%$, $(3.0 \pm 0.5)\%$, and $(1.7 \pm 0.3)\%$ for $t_s = 1.28$ s, 6.4 s, and 10.24 s, respectively. Considering the integration gate, for the two longer storage times this is consistent with the measurement using classical pulses. For the retrieved few-photon pulses at $t_s = 1.28$ s the efficiency is

about 20% lower than expected. We explain this by a decay of the transmission of the filter passband. The probe pulse reference measurement takes place 10 ms after the first filter preparation sequence is finished but the signal pulse detection occurs 280 ms after the additional filter preparation (during the storage time). This means that a decay of the population prepared in the filter crystal within the 270 ms longer waiting time will reduce the measured efficiency. The timescale of ~ 100 ms between filter preparation and signal pulse is well below the population lifetime $T_1 \approx 100$ s so this effect should be negligible. However, we measured an increase of the OD in the filter passband by about 0.3 within 100 ms. This effect might correlate to the delicate preparation of the filter setup or noise introduced in the filter crystal's cryostat. For $t_s > 1.28$ s, we repeat the preparation of the filter crystal more often. This alters the distribution of the population slightly (i.e., toward the aimed distribution) and leads to a reduced effect of the decay. We did not see a similar decay of transmission in the storage crystal after preparation of a spectral pit. Since the decay of the filter transmission reduces the number of detected signal photons we should investigate it more closely in future work.

Despite the slightly lower efficiency for $t_s = 1.28$ s, the data confirm that we maintain the coherence time of $T_2 = 7.5$ s measured for classical pulses also at the few-photon level. To the best of our knowledge, our results represent the first demonstration of storage of weak coherent pulses on a 10 s timescale. The coherence time of $T_2 = 7.5$ s pushes the state-of-the-art by over an order of magnitude [95]. We note, however, that the background noise prevented us from storing also single photon pulses with $\bar{n} = 1$ on this very long timescale.

We explore now the limits of our memory at a fixed storage time of $t_s = 1.28$ s. Figure 6.6(b) shows the photon counts for storage of pulses with different average photon number. We can easily discriminate the retrieved signal pulses for $\bar{n} = 109$ and $\bar{n} = 55$ from the background noise. The retrieved pulse with $\bar{n} = 7$ is just visible above the noise level. The SNR is in this case 0.6 ± 0.2. As described above, the efficiency of $\eta_{LS} = (5.9 \pm 0.3)\%$ (averaged over all three measurements) is lower than expected when we consider the tight integration range (covering $\sim 75\%$ of the signal) and the classical measurement with $\eta_{LS} = (9.1 \pm 0.3)\%$. Nevertheless, we are able to detect the signal pulses for storage of weak coherent pulses over $t_s = 1.28$ s.

When we determine and plot the SNR for the three pulses at different photon numbers [see Figure 6.6(a)], we can apply a linear fit to estimate the probe pulse photon number required to obtain a SNR of 1 (gray, dashed line). From the fit we see, that this is the case for a probe pulse with $\bar{n} = 10.9 \pm 0.2$ photons. Although the efficiency is reduced by almost a factor of 3, this threshold is at the same photon number as for $t_s = 2\,\mu$s. This is due to a better control read pulse suppression which we explain by a slightly different control beam alignment on the different days of measurement. We calculate, that at the single photon level we get SNR $= 0.091 \pm 0.002$. Though this is not yet sufficient for single photon storage, the data nevertheless confirm EIT light storage at the few-photon level, beyond 1 s storage time, implemented in a solid state system.

In this chapter, we presented our optimization of the setup for efficient storage of weak coherent pulses on the timescale of seconds. Using an optimized composite

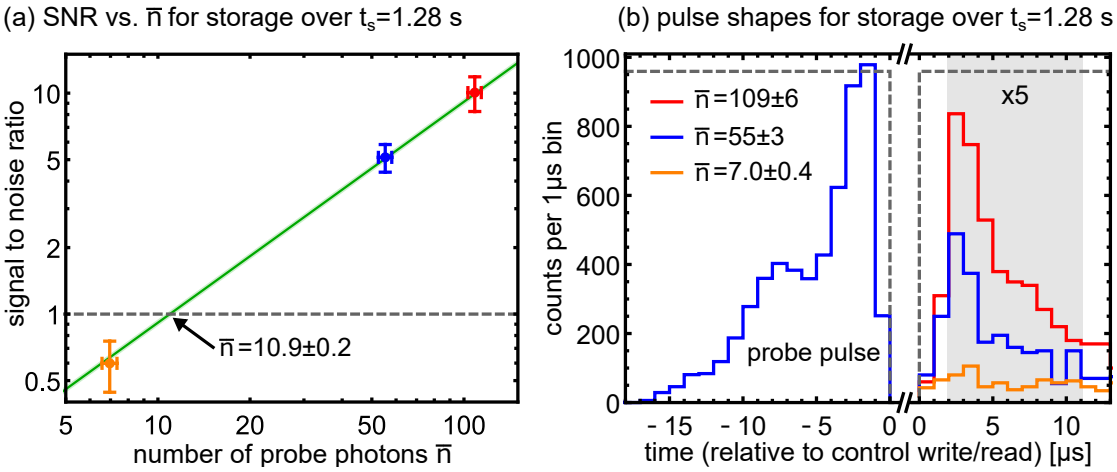

Figure 6.6: EIT light storage of weak coherent pulses at the ZEFOZ point with $N = N_f = 2$ passes of the storage and filter crystals and one DD cycle using a UR64 sequence, giving a storage time $t_s = 1.28\,\mathrm{s}$. (a) SNR versus number of probe photons $\bar{n}$. With larger $\bar{n}$ the SNR increases. The green, solid line represents a linear fit from which we deduce that for $\bar{n} = 10.9 \pm 0.2$ the SNR is 1 (see intersection with the gray, dashed line). (b) Photon counts (in $1\,\mu\mathrm{s}$ bins) versus time for storage of $\bar{n} = 109 \pm 6$ (red), 55 ± 3 (blue), and 7.0 ± 0.4 (orange) photons. For simplicity we show only the probe pulse of the $\bar{n} = 55 \pm 3$ measurement. We accumulate the data over 500, 1000, and 1750 repetitions, respectively, normalize them to 1000 repetitions for better comparison, and magnify the signals by a factor of 5. The gray, dashed line represents the control intensity for time reference and the gray shaded area shows the signal integration gate.

rephasing sequence combined with the ZEFOZ technique we achieved storage of weak coherent pulses with an average of 52 photons for up to 10 s storage time. The $1/e$ decay time of our memory is 7.5 s. At a storage time of 1.28 s, we characterized the background noise level and found that the threshold of SNR = 1 is reached for storage of 11 photons. In previous research on storage of single photons, the longest storage time was 100 ms [95]. Although we cannot quite operate at the single photon level, our storage time of 7.5 s sets a new benchmark for storage of weak coherent pulses. Therefore, this result is part of a manuscript prepared for publication.

Applying our concepts (i.e., multipass setups for increased efficiency and background noise suppression and combining ZEFOZ with composite rephasing techniques) to other storage protocols with intrinsically less noise (e.g., the AFC protocol) could significantly enhance the efficiency and storage time of single photon memories. Our experimental results are therefore of relevance for a bigger community, including groups implementing other storage protocols or using different storage media.

Chapter 7

Composite Pulses for Population Inversion in Pr:YSO

In Chapter 5 we presented UR sequences that enable efficient rephasing of coherences despite pulse errors. These sequences are designed to act as an identity propagator, i.e., to preserve an arbitrary initial state. A related problem is to invert an arbitrary state in a robust way, i.e., to flip a superposition of two quantum states $|\psi\rangle_i = c_1|1\rangle + c_2|2\rangle$ into $|\psi\rangle_f = c_2|1\rangle + c_1|2\rangle$. A single π pulse performs such an inversion but it suffers from pulse errors. Composite sequences of pulses with different phases can compensate these pulse imperfections and are well known from NMR [92]. In this chapter, we introduce universal composite pulses (UCPs) and present a variant of UCPs that enables shaping of the excitation profile with respect to pulse area and detuning errors. Our proposal and convincing experimental demonstration which confirms the superior performance led to a publication in Physical Review A [97].

7.1 Universal Composite Pulses With Arbitrary Excitation Profile

UCPs were developed in our team for robust population inversion [58]. Similar to the derivation of UR sequences (compare Section 5.3 and [57]), we consider the action of a sequence of identical pulses (apart from their different phases) on an arbitrary state. Using the phases as control parameters, we maximize the transition probability P_{12} of the sequence, i.e., minimize the influence of pulse errors. With higher number of pulses n in a sequence, we achieve higher order error compensation. The sequences perform robust population inversion for an arbitrary initial state and the phases do not depend on the imperfection of the constituting pulses.

In the original proposal, Genov *et al.* identified two classes of robust sequences (termed "a" and "b") [58]. The sequences labeled "a" perform better against errors in the pulse area (i.e., pulse duration and amplitude) and the sequences labeled "b" perform better against errors in the detuning. In Table 7.1 we list the phases ϕ_k of each pulse of the "a" and "b" type sequences up to order $n = 7$.

To illustrate the robustness of the different classes of sequences, we simulate the evolution of a system which we initially prepare in state $|1\rangle$ under the influence of our pulse sequence which aims to transfer the system to state $|2\rangle$. In Figures 7.1(a), (e), and (i) we show the transfer probability P_{12} versus the pulse parameters duration and detuning. For a single pulse (a), P_{12} drops quickly when the pulse duration τ (or, more general, pulse area $\Omega\tau$) and detuning Δ deviate from their optimal values $\tau = 10\,\mu s$ and $\Delta = 0$. In contrast, the simulated U5 sequences [i.e., with order $n = 5$, Figures 7.1(e) and (i)] are significantly more robust against variations in τ and Δ (compare, e.g., the red regions with $P_{12} > 0.95$). Furthermore, the U5a sequence

Table 7.1: Phases ϕ_k of UCPs with n pulses. Each phase is defined modulo 2π. The phases ϕ_k are examples for different sequences (defined by choosing ϕ_2) and are determined according to [97]. In order to permit comparison to [58], we include also the labels of the "a" and "b" classes of the UCPs. The excitation dynamics remain the same when we simultaneously add a constant shift to all phases ϕ_k.

Group	Sequence	Label a/b	Phases $\phi_k,\ k = 1, \ldots, n$
U3	U3(0°)	U3b	$(0, 0, 1)\pi$
	U3(45°)		$(0, 1, 6)\pi/4$
	U3(90°)	U3a	$(0, 1, 0)\pi/2$
	U3(135°)		$(0, 3, 2)\pi/4$
U5	U5(0°)		$(0, 0, 2, 1, 2)\pi/3$
	U5(60°)		$(0, 1, 4, 4, 0)\pi/3$
	U5(90°)		$(0, 3, 10, 11, 4)\pi/6$
	U5(150°)	U5a	$(0, 5, 2, 5, 0)\pi/6$
	U5(180°)		$(0, 3, 2, 4, 2)\pi/3$
	U5(240°)		$(0, 4, 4, 1, 0)\pi/3$
	U5(270°)		$(0, 9, 10, 5, 4)\pi/6$
	U5(330°)	U5b	$(0, 11, 2, 11, 0)\pi/6$
U7	U7(75°)		$(0, 5, 22, 23, 10, 5, 12)\pi/12$
	U7(165°)	U7a	$(0, 11, 10, 17, 10, 11, 0)\pi/12$
	U7(255°)		$(0, 17, 22, 11, 10, 17, 12)\pi/12$
	U7(345°)	U7b	$(0, 23, 10, 5, 10, 23, 0)\pi/12$

has a higher robustness with respect to variations of τ and the U5b sequence is more robust against variations of Δ. The additional robustness is due to higher order error correction for errors in the respective parameter.

Now, we present an extended version of UCPs that enables higher order error correction for an arbitrary combination of errors in τ and Δ. For a detailed description and the derivation, we refer to our work [97]. In the new approach, we use a more general analytic solution to determine appropriate phases for the sequences in order to maximize the transition probability. This solution achieves the same order of error compensation as the original one, however, with the phase ϕ_2 of the second pulse as a free parameter. Choice of ϕ_2 fixes the phases of the other pulses in the sequence. Table 7.1 lists some specific values of the phases ϕ_k for sequences of order $n = 3, 5$, and 7.

To evaluate the different performance of the UCPs with different ϕ_2, we perform a simulation of the U5 sequence for different values of ϕ_2. Figure 7.1 shows the resulting excitation profiles with respect to τ and Δ. When we change ϕ_2, the excitation profiles rotate, i.e., we get higher order error compensation when the errors in the pulse area (i.e., $\Omega\tau$) and the detuning Δ correlate. This correlation might, e.g., be due to a Stark shift induced by the pulses as discussed in Chapter 5. By tuning ϕ_2, the excitation profile can be matched to the specific fluctuations of parameters in an experiment and enable additional error compensation at no additional cost. By extensive simulations, we confirmed this behavior of the excitation profile for any order of the UCP sequence.

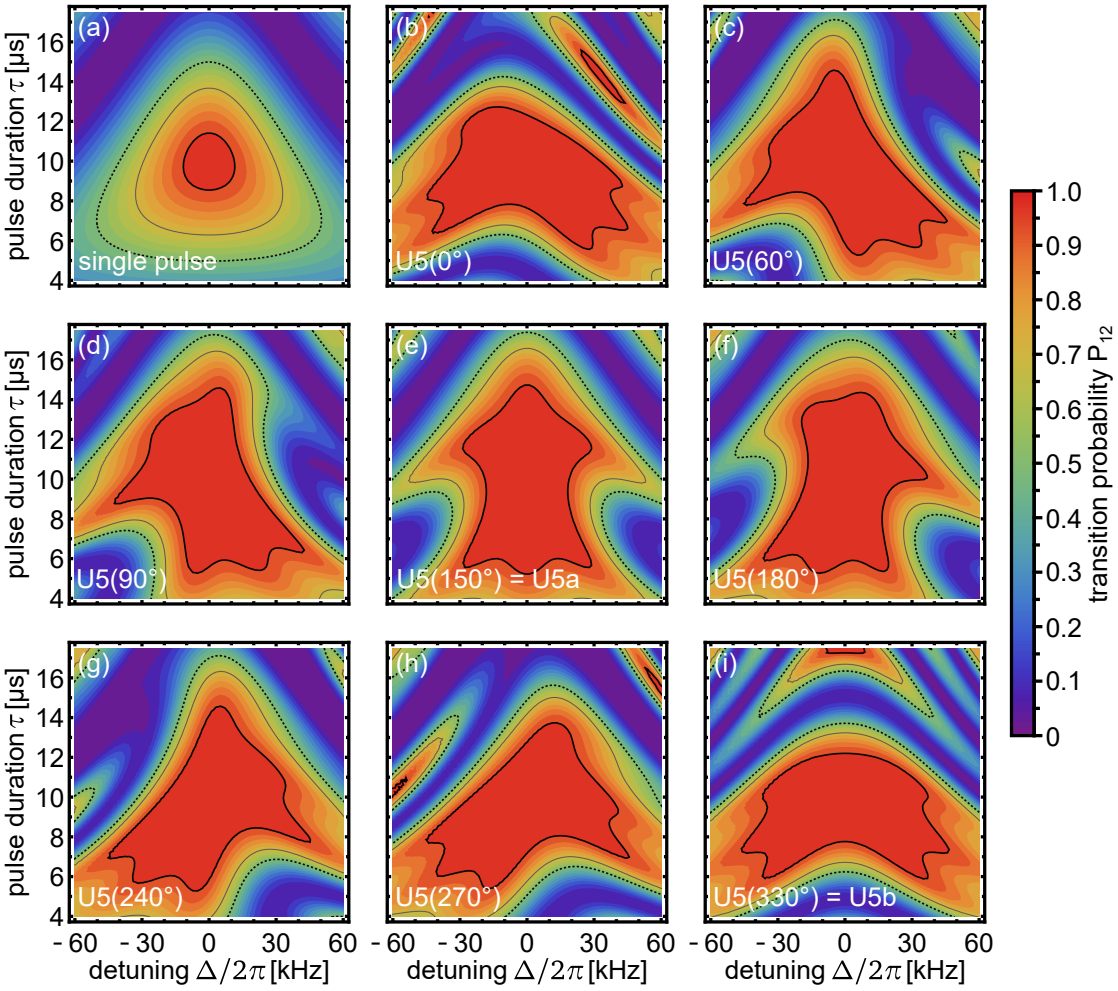

Figure 7.1: Simulated transition probability P_{12} (color scale) for a single pulse (a) and U5 sequences with different ϕ_2 (b)–(i) versus pulse duration τ and detuning Δ. We assume rectangular pulses with a Rabi frequency of $\Omega_{RF} = 2\pi \times 50$ kHz. Thick solid lines indicate regions of high transition probability $P_{12} > 0.95$, thin solid lines regions with $P_{12} > 0.7$, and dashed lines regions with $P_{12} > 0.5$. Increasing the value of ϕ_2 causes a rotation of the excitation profile [compare the profiles from (b) to (i)].

7.2 Rephasing of EIT Light Storage by UCPs

To experimentally confirm the performance of the UCPs, we apply them to rephasing of EIT light storage signals. We note that the UR sequences presented in Chapter 5 are more appropriate (i.e., efficient) for rephasing. However, as we can use UCPs as an efficient replacement for π pulses, rephasing of atomic coherences (e.g., prepared by EIT) represents an adequate test system for evaluating their performance. The EIT light storage signal serves as a measure for the rephasing efficiency and hence the efficiency of a π pulse or UCP.

We perform EIT light storage at zero magnetic field in a single ensemble. After optimizing the pulse parameters, we achieve an efficiency of $\eta_{LS} = (20.0 \pm 0.4)\%$ at a short storage time of $t_s = 2\mu s \ll T_2^*$. To provide the rephasing pulses, we use the RF coils described in [18] and an impedance matching circuit outside the cryostat which provides impedance matching with 600 kHz bandwidth (FWHM), i.e., much

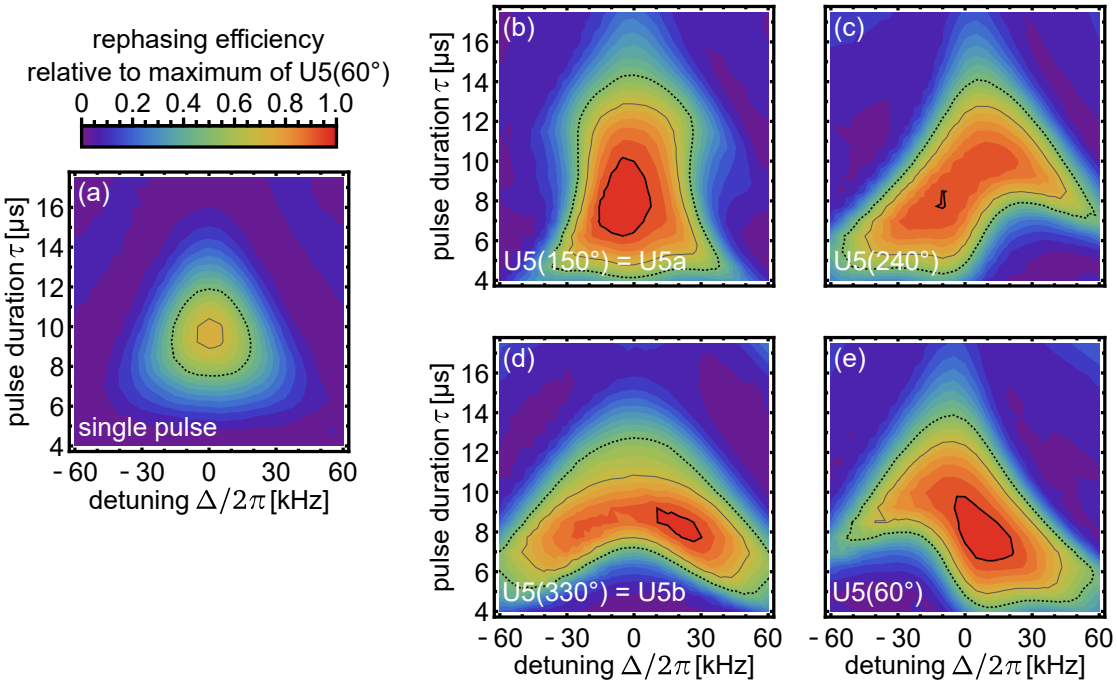

Figure 7.2: Experimental data: Rephasing efficiency (color scale) versus pulse duration τ and detuning Δ for EIT light storage using single π pulses and U5 pulses with different ϕ_2. We normalize the rephasing efficiency to the maximal efficiency of all investigated sequences, i.e., the maximum of the U5(60°) sequence.

broader than the considered detuning range of 120 kHz, at the central frequency $\nu_{RF} = 10.2$ MHz. Furthermore, we note that the fiber seed laser[1] of the OPO system differs from the one described in Section 2.1. This results in an increased optical linewidth of about 100 kHz on a timescale of 100 ms.

We set the storage time to $t_s = 400\,\mu$s, i.e., much longer than T_2^* but below the decoherence time $T_2 \approx 500\,\mu$s and set the RF amplitude such that the Rabi frequency is $\Omega_{RF} = 2\pi \times 50$ kHz. The higher Rabi frequency compared to the measurements shown in Chapter 5 is due to the higher dipole moment of the transition used here, i.e., at zero magnetic field. We first measure the performance of rephasing with two π pulses when we vary the pulse duration τ and detuning Δ. We show the measured rephasing efficiency [normalized to the maximum of all investigated sequences, i.e., the maximum of the U5(60°) sequence] in Figure 7.2(a). As expected, we find the highest rephasing efficiency at $\Delta = 0$ and $\tau = 10\,\mu$s, i.e., a pulse area of $\Omega_{RF}\tau = \pi$. However, the maximal light storage efficiency is only $\eta_{LS} = 4.7\%$, i.e., reduced by a factor of four compared to the result at $t_s = 2\,\mu$s. This reduction is partially due to pulse errors and partially due to decoherence (note that $t_s \lesssim T_2$). When we deviate from the optimal pulse parameters, the rephasing efficiency quickly drops. Comparison to the simulation of the transition probability [Figure 7.1(a)] shows that the excitation profile has the same shape but the rephasing efficiency drops more quickly when we deviate from the optimal pulse parameters. This is due to the application of the second pulse in the case of rephasing. In this case, we can estimate the rephasing efficiency by the square of the transition probability leading to the

[1] Koheras AdjustiK Y10 PM PztM, NKT Photonics

narrower rephasing profile [45]. Furthermore, in the case of imperfect rephasing, the system is not fully prepared correctly during readout. This causes reabsorption of the signal and decreases the efficiency further.

Now we replace each of the π pulses by five consecutive π pulses (without temporal separation) with relative phases according to the U5 group (see Table 7.1) and repeat the parameter scan. Figures 7.2(b)–(e) show the experimentally determined rephasing efficiencies for four different choices of the parameter ϕ_2. For all values of ϕ_2, the parameter range of high rephasing efficiency is significantly increased compared to the single pulse measurement. The shapes of the rephasing profiles match the simulated excitation profiles, i.e., choice of ϕ_2 rotates the rephasing profile. This enables matching of the profile to the specific imperfections of the rephasing pulses. Upon careful comparison of the rephasing profiles to the simulation, we find that smaller features [e.g., the "wings" of the U5(150°) excitation profile at $\Delta = \pm 2\pi \times (30 \ldots 60)\,\mathrm{kHz}$ and $\tau = (9 \ldots 12)\,\mu\mathrm{s}$] are not present in our experimental data. We explain this by a field inhomogeneity and resulting averaging effects that wash out these smaller structures. Furthermore, we find the tendency of worse rephasing efficiency for higher pulse durations [e.g., the region of high transition probability of the U5(330°) sequence at $\Delta = 0$ and $\tau > 16\,\mu\mathrm{s}$]. This can be explained by inhomogeneous broadening and field inhomogeneity that reduce the rephasing efficiency for longer interaction times and that are not considered in our simulation. Additionally, we reach higher efficiency using the U5(60°) sequence than using the U5(240°) sequence [compare Figure 7.2(c) and (e)]. Also, the U5(330°) sequence [Figure 7.2(d)] is slightly asymmetrical, i.e., reaches a higher efficiency for positive detuning, although we expect a symmetrical profile [compare Figure 7.1(i)]. We explain this behaviour by a slight positive detuning of the impedance matching circuit in combination with averaging over different Rabi frequencies due an inhomogeneous RF field.

We achieve the maximal rephasing efficiency using the U5(60°) sequence [see Figure 7.2(e)]. At $\Delta = 2\pi \times 5\,\mathrm{kHz}$ and $\tau = 7.75\,\mu\mathrm{s}$, the rephasing efficiency is 37% higher than for the π pulse rephasing. We note that the magnitude of the gained efficiency depends on the amount and type of pulse errors and the given value is specific to our experimental setup. Our data confirm the predicted high error compensation of UCPs and the higher order error compensation for combination of specific errors. We can distort and rotate the excitation profile of a UCP sequence continuously in a controlled way by changing the phases. This is of relevance for systems in which different pulse errors are correlated to each other.

Chapter 8

Composite STIRAP

In the previous chapter, we presented UCPs as an alternative to single π pulses for efficient population inversion of arbitrary states in a two-level system. In three-level systems, stimulated Raman adiabatic passage (STIRAP) is a common technique for efficient population transfer. STIRAP has numerous applications, e.g., in atomic, molecular and solid state physics and chemistry, as well as in quantum information technology [98, 99]. To further enhance the efficiency and robustness of STIRAP, Torosov *et al.* proposed to combine STIRAP with composite techniques, i.e., composite STIRAP (CSTIRAP) [100]. In the following, we present an experimental implementation of CSTIRAP as well as further developments toward a universal robust version of CSTIRAP. Our implementation is the first proof-of-concept demonstration and we published the results in Physical Review A [101].

8.1 Efficient Population Inversion by STIRAP

The coupling scheme of STIRAP is similar to EIT, involving three states and two laser pulses, which are for STIRAP conventionally termed pump and Stokes (rather than probe and control as in EIT). This mirrors the fact that in STIRAP both pulses are strong while in EIT we consider only the control pulse strong and the probe pulse does not affect the level structure. In the following, we use the indices P and S to refer to the Rabi frequencies Ω_i and detunings Δ_i of the pump and Stokes pulses, respectively. For details on STIRAP, we refer the reader to [99].

Figures 8.1(b) and (c) show the pulse sequence and the population during STIRAP. First, we apply a Stokes pulse and after a delay t_{SP} the pump pulse. This is called the counterintuitive order because the first pulse does not couple the populated ground state. Still, this sequence achieves a higher population transfer efficiency than the

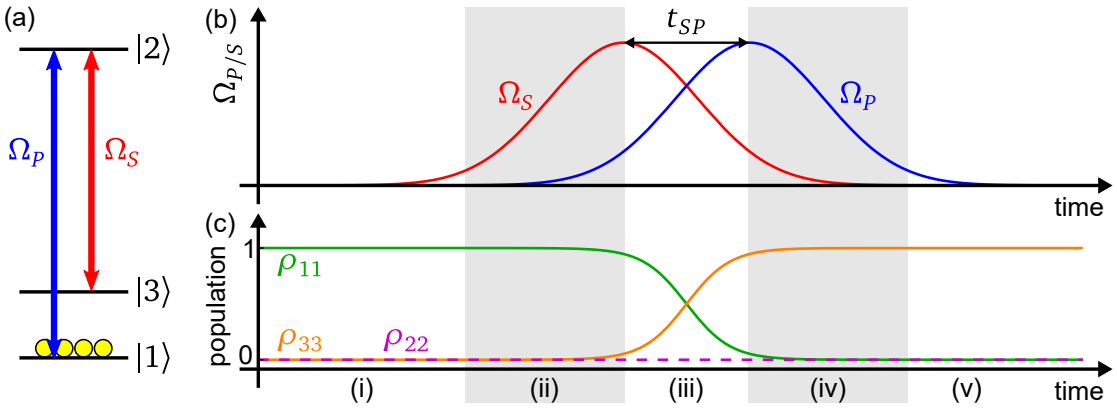

Figure 8.1: STIRAP scheme. (a) Λ-type coupling scheme with population (yellow disks) initially prepared in $|1\rangle$. (b) Rabi frequency of the Stokes (red) and pump (blue) pulses versus time. (c) Population in the three states versus time during STIRAP.

intuitive order. To understand this, we consider the system Hamiltonian $\hat{H}$ given in Chapter 1 and replace the quantum probe field by the classical pump field. By diagonalizing $\hat{H}$, we find the eigenstates of the coupled system, called dressed states. Relevant for STIRAP is the dark state $|a^0\rangle = \cos(\theta/2)|1\rangle + \sin(\theta/2)|3\rangle$, where the mixing angle $\theta = -2\arctan(\Omega_P/\Omega_S)$ determines the contribution of the bare states $|1\rangle$ and $|3\rangle$. The dark state has no contribution of the decaying state $|2\rangle$. Therefore, the dark state (and hence the STIRAP transfer efficiency) does not suffer from decay.

For STIRAP, we initially prepare the system in $|1\rangle$ and apply the Stokes pulse **(i)**. The dark state $|a^0\rangle$ coincides with the prepared state $|1\rangle$, i.e., the medium is prepared in $|a^0\rangle$. When we apply the pump pulse in parallel to the Stokes pulse **(ii)**, the mixing angle θ decreases (below 0) and the dark state becomes a superposition of $|1\rangle$ and $|3\rangle$. Initially, the Rabi frequency of the pump pulse is low compared to the Stokes pulse which corresponds to the EIT scheme for the pump pulse. Therefore, the population remains in $|1\rangle$, i.e., it is not excited to $|2\rangle$. When Ω_P increases further and above Ω_S **(iii)**, the mixing angle decreases toward $-\pi$, i.e., the population is transferred from $|1\rangle$ to $|3\rangle$ without populating $|2\rangle$. When the Stokes Rabi frequency approaches zero **(iv)**, the EIT situation is inverted, i.e., the strong pump pulse acts as the EIT control field such that the Stokes pulse does not excite the population into $|2\rangle$. Finally, we turn off the pump field **(v)**.

STIRAP exploits the dark state to efficiently transfer the population from $|1\rangle$ to $|3\rangle$. This process has the advantage that it is insensitive to variations in amplitude, shape and timing of the pulses provided some limits are kept. Furthermore, there is no population in the (lossy) optically excited state $|2\rangle$ [99].

To achieve the efficient population transfer, the system must remain in the dark state despite the external manipulation. This requires slow, i.e., adiabatic, changes of the pump and Stokes fields which we can express (for smooth pulses) by the adiabaticity condition $\mathcal{A} = \int \Omega_{rms}(t)\mathrm{d}t \gg 1$, i.e., the pulse area $\mathcal{A}$ must be sufficiently large [99]. Here, $\Omega_{rms}(t) = \sqrt{|\Omega_P(t)|^2 + |\Omega_S(t)|^2}$ is the root mean square Rabi frequency. The larger $\mathcal{A}$, the closer the transfer efficiency approaches unity. Hence, under realistic conditions of limited pulse area (i.e., finite interaction time and limited pulse intensity) the fidelity of the transfer efficiency of STIRAP is always limited. This becomes a particular obstacle, if we require repeated (cyclic) STIRAP processes, e.g., to drive logic operations [102].

Torosov *et al.* proposed to replace the single STIRAP pulse sequence by several STIRAP sequences with the relative phases of the pulses as control parameters. Similar to composite pulses, this allows for compensation of losses due to imperfect adiabaticity, and enables arbitrarily accurate population inversion [100]. In the sequence of STIRAP pulse pairs, we transfer the population back and forth between the initial and the target state. To ensure that the initial state for each constituent

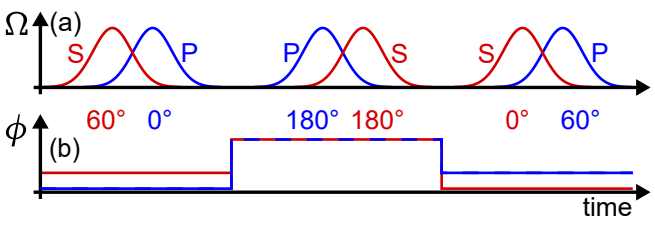

Figure 8.2: R3 CSTIRAP scheme. (a) The Rabi frequency versus time shows the alternating pulse order. (b) Phases of the Stokes (red) and probe (blue) pulses versus time.

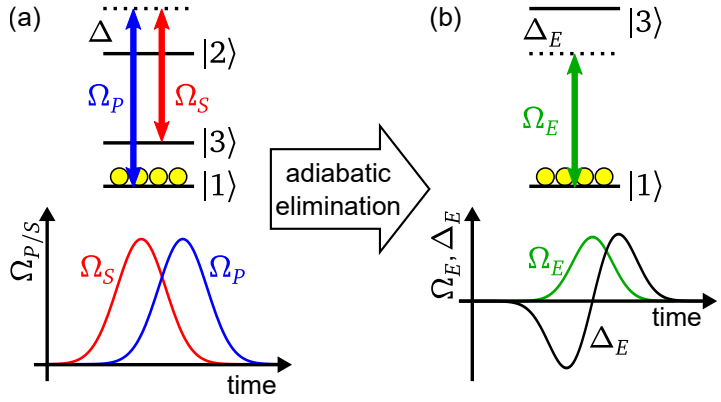

Figure 8.3: Adiabatic elimination of $|2\rangle$ converting a three-level system (a) to an effective two-level system (b). The plots show the Rabi frequencies of the Stokes and pump field Ω_S and Ω_P (a) and the effective Rabi frequency Ω_E and detuning Δ_E(b) versus time.

STIRAP pulse pair is the dark state, the order of the pump and Stokes pulses alternates for each consecutive pair (see Figure 8.2).

We implemented first proof-of-concept experiments on CSTIRAP, as proposed in [100] and briefly explained above, for population transfer in Pr:YSO. However, we found that the additional efficiency gain by CSTIRAP is canceled due to the inhomogeneous broadening of the optical transition. We refer to [101, 103] for details of these measurements. As CSTIRAP via resonant couplings did not improve the transfer efficiency in our experiment, we modified the approach toward the detuned regime, i.e., for $\Delta_P = \Delta_S \equiv \Delta \gg \Omega_{P/S}$. In this case, we can treat the three-level system as an effective two-level system by using adiabatic elimination of $|2\rangle$ [104]. The two level system of $|1\rangle$ and $|3\rangle$ is then driven by a field with an effective two-photon Rabi frequency $\Omega_E(t) = -\Omega_P(t)\Omega_S(t)/(2\Delta)$ and detuning $\Delta_E(t) = (|\Omega_P(t)|^2 - |\Omega_S(t)|^2)/(2\Delta)$. Figure 8.3 shows the temporal behavior of the Rabi frequency and detuning before (a) and after (b) adiabatic elimination for a detuned STIRAP pulse pair on two-photon resonance (i.e., $\Delta_P = \Delta_S \equiv \Delta$). The symmetric temporal change of the detuning $\Delta_E(t)$ over the resonance resembles rapid adiabatic passage (RAP) in the effective two-state system [105].

RAP enables population transfer in a two-level system. The transfer efficiency is independent of the sign of the (chirped) detuning, i.e., the order of the pump and Stokes pulses applied in the three-level system. This means that for repeated application of detuned STIRAP, the pulse order does not need to be alternating to achieve high efficiency. Furthermore, we can exploit the description as a two-level system and apply the UCPs which we introduced in the previous chapter. This allows for development of UR detuned STIRAP sequences. The relative phase between the pump and Stokes fields directly translates to the phase of the effective two-photon Rabi frequency. Therefore, we can set the phase of the Stokes field to zero without

Sequence	ϕ_P
D3	$(0,1,0)2\pi/3$
D5	$(0,2,1,2,0)2\pi/5$
U3a	$(0,1,0)\pi/2$
U5a	$(0,5,2,5,0)\pi/6$
U5b	$(0,11,2,11,0)\pi/6$

Table 8.1: Pump pulse phases ϕ_P for different CSTIRAP sequences with $n = 3$ and 5 pulse pairs. The Stokes pulses have phase $\phi_S = 0$ for all sequences. Sequences labeled "D" correspond to detuned CSTIRAP, as originally proposed in [100]. Labels "U" correspond to our universal version of detuned CSTIRAP and equal the phases given in Table 7.1 [101]. The number attached to the labels denotes the number n of pulse pairs in a sequence.

loss of generality and use the phase ϕ_P of the pump field as a control parameter.

Torosov *et al.* also derived phases for robust detuned CSTIRAP. In Table 8.1 we list them along with the phases for the UR detuned CSTIRAP (which are equivalent to the UCP phases given in the previous chapter). Torosov *et al.* designed the solutions for detuned CSTIRAP to improve the performance for limited (weak) adiabaticity due to insufficiently large pulse areas [100]. However, the sequences do not compensate other errors or variations, e.g., in the two-photon detuning $\delta = \Delta_P - \Delta_S$. It is well known that the efficiency of STIRAP is highly sensitive to the latter (hence, to laser frequency changes or two-photon inhomogeneous broadening) [99]. When we apply the phases known from UCP, we compensate errors in any pulse parameter. Therefore, we expect universal CSTIRAP to outperform the original proposal in terms of transfer efficiency.

8.2 CSTIRAP in Pr:YSO

To test the performance of CSTIRAP, we apply it for population transfer among the hyperfine states in Pr:YSO. In contrast to EIT, which requires a weak probe and a strong control field, we require two strong fields for STIRAP. Therefore, we use an additional beamline as shown in Figure 8.4. In the Pr:YSO crystal (0.05% dopant concentration, $5 \times 5 \times 3\,\mathrm{mm}^3$), the pump and Stokes beams intersect under a small angle, are collimated and have a cross section of $600 \times 380\,\mu\mathrm{m}^2$ and $480 \times 400\,\mu\mathrm{m}^2$ (FWHM), respectively, resulting in peak Rabi frequencies of $\Omega_{P/S}^{\max} \approx 2\pi \times 700\,\mathrm{kHz}$. To measure the population distribution, we use a focused probe beam with a diameter of 190 µm (FWHM) that intersects the central region of the interaction zone of the pump and Stokes beamlines. The smaller diameter of the probe beam minimizes spatial averaging effects as we only probe the population in the central fraction of the Gaussian pump and Stokes beam profiles. To implement the phase shifted pump and Stokes pulses, we use the AWG to provide the RF fields driving the respective AOMs. The setup achieves a phase accuracy of $< 0.5°$ with a phase jitter of roughly $0.7°$ on a timescale of 100 µs which is the duration of a typical CSTIRAP sequence (see [103] for more detailed information).

We apply (C)STIRAP for transferring the ground state population in Pr:YSO from $|1\rangle = |^3\mathrm{H}_4(0), \mathrm{m_I} = \pm\frac{3}{2}\rangle$ (which we initialized by the preparation described in Chapter 2) to $|3\rangle = |^3\mathrm{H}_4(0), \mathrm{m_I} = \pm\frac{1}{2}\rangle$. To ensure well-defined transition moments, we use a single ensemble preparation and couple to the excited state $|2\rangle = |^1\mathrm{D}_2(0), \mathrm{m_I} = \pm\frac{3}{2}\rangle$.

Figure 8.5 shows the experimental sequence of our (C)STIRAP measurements. After the preparation, we wait for 1.5 ms before we start the (C)STIRAP sequence. This ensures that no population is left in the excited state $|2\rangle$ (which decays on a timescale of $T_1^e = 164\,\mu\mathrm{s}$). The (C)STIRAP sequence duration is much shorter than

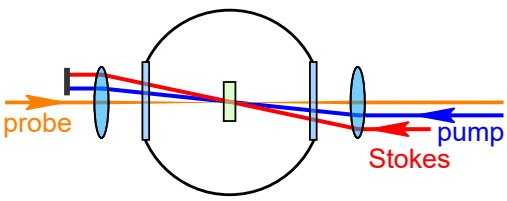

Figure 8.4: Beamlines for STIRAP. The pump and Stokes beams are collimated and intersect in the Pr:YSO crystal (faint green). The probe beam has a focus in the center of the interaction region of the other two beams.

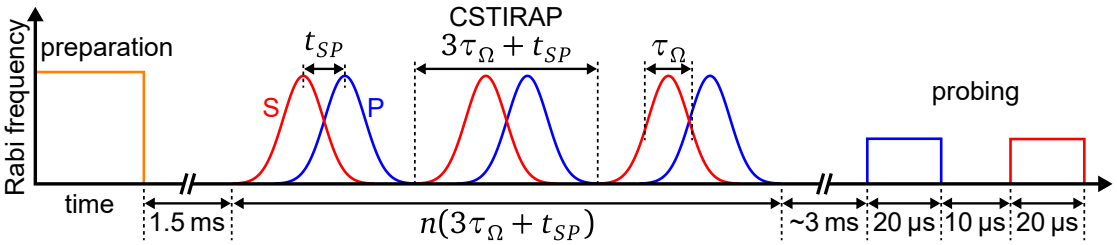

Figure 8.5: Experimental CSTIRAP sequence: Rabi frequency versus time. After the preparation, we apply CSTIRAP for inversion of the ground state population. As an example, we depict a sequence of $n = 3$ pulse pairs. The Rabi frequencies of all pulses have a temporal Gaussian shape with a duration (FWHM) of $\tau_\Omega = 14\,\mu s$. We truncate the pulses at $3\tau_\Omega$. There is no additional delay between consecutive pulse pairs, to minimize the duration of the total sequence. In the experiments, we systematically vary the delay t_{SP} between pump and Stokes pulses in each pair. To determine the population distribution, we apply two probe pulses to measure the absorption on both optical transitions.

the coherence time T_2 to ensure a proper phase relationship between the pulses. After (C)STIRAP, we determine the final populations in $|1\rangle$ and $|3\rangle$ by absorption measurements with two weak probe pulses at the pump and the Stokes transitions. The measurement on both transitions ensures a high measurement accuracy even for high absorption on one of the transitions. We estimate the uncertainty in the transfer efficiency to be well below 3% for the regime of high transfer efficiency (see [103]).

Now we compare the transfer efficiency η_t of standard detuned STIRAP to five times repeated STIRAP and the robust D5 and U5b CSTIRAP sequences. We choose a detuning of $\Delta = 1.75\,\text{MHz}$ as a compromise between high effective Rabi frequency (which scales with $1/\Delta$) and high enough detuning to fulfill the requirement for adiabatic elimination $\Delta \gg \Omega_{P/S}$. Figure 8.6 shows η_t for the different sequences when we systematically vary the pulse delay t_{SP}. Single detuned STIRAP yields equal η_t above 80% for both intuitive ($t_{SP} \approx -5\,\mu s$) and counterintuitive pulse order ($t_{SP} \approx 5\,\mu s$). This indicates that the detuning is high enough to apply the adiabatic elimination of $|2\rangle$.

When we apply five STIRAP pulse pairs, η_t suffers substantially from accumulated errors and does not exceed 50%. In contrast, D5-CSTIRAP reaches the peak efficiency of single STIRAP at 80% while simultaneously increasing the width of the efficient

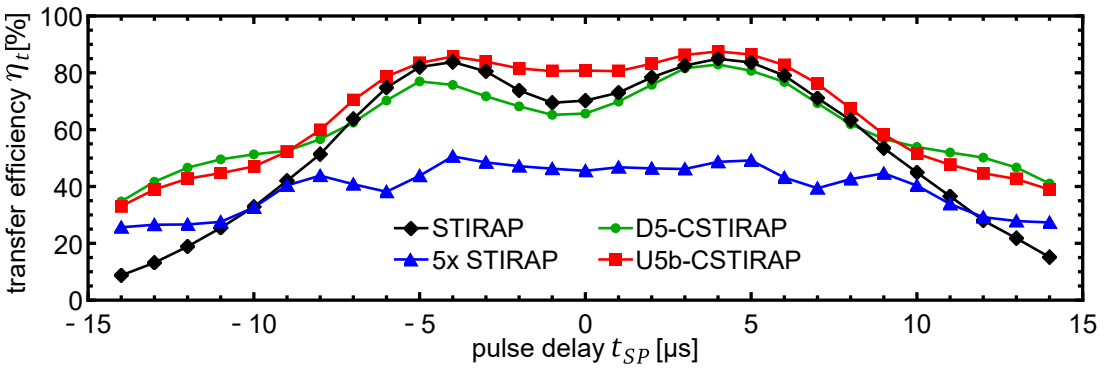

Figure 8.6: Experimentally determined transfer efficiencies η_t of detuned (C)STIRAP versus pulse delay t_{SP}. We apply $n = 5$ pulses in the repeated (C)STIRAP sequences. We adapted the single photon peak Rabi frequencies $\Omega_P = 2\pi \times 640\,\text{kHz}$ and $\Omega_S = 2\pi \times 550\,\text{kHz}$ to give equal η_t for intuitive and counterintuitive pulse order.

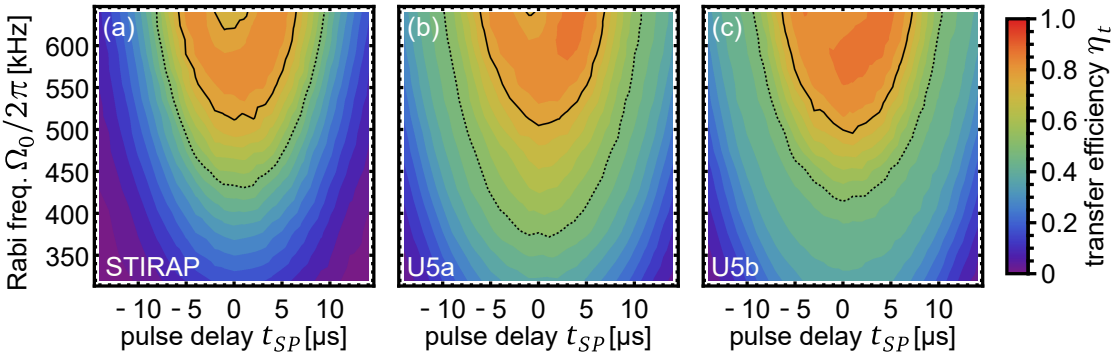

Figure 8.7: Experimental transfer efficiencies η_t of different detuned (C)STIRAP processes for variation of both pulse delay t_{SP} and peak Rabi frequency Ω_0. The single photon peak Rabi frequencies of the pump and Stokes pulses are $\Omega_P = \Omega_0$ and $\Omega_S = 0.85\Omega_0$, with Ω_0 given in the plots. We adapted the ratio of Ω_S and Ω_P to give equal η_t for intuitive and counterintuitive pulse order. Solid lines indicate regions of high transfer efficiency ($\eta_t > 0.75$) and dashed lines indicate regions with $\eta_t > 0.5$.

transfer region. Finally, the novel universal sequence U5b-CSTIRAP outperforms all other configurations. It combines peak transfer efficiencies around 85% with similarly large robustness against delay variations as D5-CSTIRAP. We note that U5a (not shown in Figure 8.6) and U5b-CSTIRAP have very similar performance with a slightly better performance of the U5b version for zero pulse delay.

To confirm the universal robustness of the U5-CSTIRAP sequences, we measure η_t and systematically vary the pulse delay t_{SP} as well as the peak Rabi frequency of the pulses. Figures 8.7(a)–(c) show the resulting efficiency profiles. The maximal transfer efficiency of detuned STIRAP (a) is $\eta_t = 84\%$. Despite the higher number of pulse pairs, U5a and U5b CSTIRAP achieve a slightly higher transfer efficiency of up to $\eta_t = 88\%$. The parameter scans clearly show a higher η_t of the CSTIRAP sequences for all parameters in the investigated region [compare Figures 8.7(b) and (c) to (a)]. This includes lower Rabi frequencies Ω_0, i.e., pulse pairs with smaller pulse area which have higher diabatic losses.

The strong performance of the universal sequences is due to their robustness with regard to variations in any arbitrary experimental parameter, while the D5-CSTIRAP sequences compensate only limited adiabaticity [100]. We note that we also applied higher order sequences of seven and nine pulse pairs for detuned CSTIRAP but they did not improve performance in comparison to U5b-CSTIRAP. We explain this by the smaller additional error compensation of the higher order sequences, which cannot make up for the higher number of (low efficiency) STIRAPs and the longer duration of the whole sequence.

In this chapter, we presented the application of UCP for improving the robustness of detuned STIRAP. We provided the first proof-of-concept demonstration of CSTIRAP and showed the additional robustness for population transfer between ground states of Pr:YSO. We found that our novel combination of UCP with STIRAP achieves a higher robustness than a previously proposed CSTIRAP sequence. The concept has applications for rephasing of coherences, e.g., in our EIT light storage experiments. Here, the two-photon transitions of CSTIRAP can replace the single-photon transitions of the RF pulses which facilitates the experimental setup.

Conclusion and Outlook

The research project dealt with the implementation of EIT light storage in the solid state medium Pr:YSO for storage of single photons on a microsecond timescale and weak coherent pulses on a timescale of seconds. The main challenge was to maintain a large efficiency at long storage times and suppress control pulse background by about 120 dB to enable detection of signals on the single photon level. We used a configuration with counterpropagating probe and control beams which enabled a control pulse suppression of about 80 dB and achieved the remaining suppression by spectral filtering. Since the signal and control read pulse frequencies differ only by ~ 10 MHz, we built a filter based on a second Pr:YSO crystal in which we tailored the absorption spectrum to the experimental requirements by optical pumping. For short storage times of 2 µs, the filter enhanced the separation between the signal and control read pulses by 42 dB. This enabled the storage of a weak coherent pulse with an average photon number of 1.1 with an efficiency of 42% and a SNR of 3.2. The efficiency was limited by the OD of the storage medium and could be increased by a multipass setup. Residual leakage of the control pulse through the filter limited the SNR. Still, to the best of our knowledge, our result represents the first implementation of single photon storage based on EIT in a solid state medium.

To prolong the coherence lifetime, we implemented ZEFOZ. The influence of the magnetic field reduced the OD of the Pr:YSO crystal which led to a lower storage efficiency. We characterized light storage under ZEFOZ conditions at a short storage time of 2 µs. By application of a multipass setup with three passes and temporal shaping of the probe pulse, we partially compensated the reduced OD and achieved efficiencies of up to 23% for storage of classical light pulses. In order to maintain a high setup transmission, we used only two passes for storage of weak coherent pulses. We demonstrated storage of a weak coherent pulse with an average of 10.2 photons for 2 µs with 16% efficiency and a SNR of 1.3. Again, leakage of the control read pulse through the spectral filter limited the SNR. We found this leakage to be due to a weak but spectrally broad pedestal in the spectrum of our OPO-SFG laser system.

In order to prolong the light storage time and exploit the long coherence lifetime under ZEFOZ conditions, we applied different sequences for rephasing with RF pulses. In the design of our RF coils for rephasing, we had to consider restrictions given by the static magnetic field setup. Therefore, the rephasing π pulses had a significant inhomogeneity which led to a low rephasing efficiency of 15% when we applied two π pulses. To compensate these errors, we applied UR DD which increased the rephasing efficiency to 40%. Due to an experimental limitation, we could not reduce the separation of the rephasing π pulses below 10 ms without reducing the storage efficiency. This limited the effectiveness of DD. Nevertheless, we achieved a storage time of 7.5 s for classical light pulses and confirmed this timescale for storage of weak coherent pulses with an average of 52 photons. We stored weak coherent pulses with different photon number for 1.28 s and extrapolated a SNR of 0.09 for storage of a single photon. For storage of a weak coherent pulse with an average of 7 photons, we determined an efficiency of 6% and a SNR of 0.6. This represents

the first implementation of a memory for weak coherent pulses close to the single photon level with a storage time in the regime of seconds. Compared to the current state-of-the-art single photon storage time of 100 ms [95], we achieve a more than one order of magnitude longer storage time.

As an extension of our investigations, we developed, implemented and studied novel universal composite pulse sequences to invert superposition states or efficiently transfer population between two states. In particular, we experimentally demonstrated UCPs for population inversion which are especially suited for situations in which pulse area and detuning errors are correlated. We showed that we can rotate the excitation profile of the sequence by changing the phases of the excitation pulses. This enables adaption to the specific correlation of errors present in an experiment. Moreover, we demonstrated a composite version of STIRAP. We showed that for detuned pulses, the phases of UCPs enhance the robustness to variations in any experimental parameter. We achieved an increase in population transfer efficiency from 50% for five times repeated detuned STIRAP to 85% for UR CSTIRAP.

Prospects for Future Work: The efficiency of the DD sequence limited the storage time of our experiment. Due to the rather long time separation of the rephasing pulses of 20 ms, the coherence carrying the light storage signal was not well protected against external influences. This lead to a decay time of the light storage signal of 7.5 s which was only about twice the coherence lifetime observed in a spin echo experiment. In order to proceed toward longer light storage times, we should investigate and rectify the reason behind the limitation to the pulse separation time. Considering the superior properties of the ZEFOZ point used in this work compared to previous work [18], we expect this to enable a storage time for weak coherent pulses longer than a minute.

To enable storage of single photons on the timescale of seconds, we must increase the SNR by at least a factor of 10. In our experiments, it was limited by the control read pulse background, the setup transmission of 14%, and the storage efficiency of 6%. The residual background is due to the broad control read pulse spectrum leaking through the filter passband. This leakage could be decreased by reducing the linewidth of the laser system or pre-filtering the read pulse spectrum. We expect that the background can be reduced below the detector dark count rate. Furthermore, we could enhance the setup transmission by designing a new multipass setup with fewer optics. This would also facilitate the use of more than two passes and enable a higher storage efficiency. Finally, a redesigned coil system for reduced eddy currents and increased RF field homogeneity could enhance the rephasing efficiency. Based on previous results [59], we expect that rephasing with near unity efficiency is possible which means a more than twofold increase of the efficiency and SNR.

To omit the large background due to the control pulse (which is in EIT coincident with the signal pulse), we could use the AFC protocol as an alternative. Here, the signal pulse is temporally separated from the driving pulses. Furthermore, the AFC protocol offers broader bandwidth and multimode capacity and is therefore better suited for the implementation of a quantum memory. In preliminary experiments shown in Appendix A, we implemented AFC light storage under ZEFOZ conditions. We showed the feasibility of the concept but to reach efficiencies comparable to or results on EIT, we require smaller spectral bandwidth of the laser system.

Zusammenfassung

Die vorliegende Arbeit beschäftigt sich mit der Implementierung von Lichtspeicherung basierend auf EIT im Festkörpermedium Pr:YSO zur Speicherung einzelner Photonen auf einer Zeitskala von Mikrosekunden und schwacher kohärenter Lichtpulse über mehrere Sekunden. Die Herausforderungen lagen hierbei im Erhalt der Speichereffizienz bei langen Speicherzeiten und in der Unterdrückung des Hintergrundsignals aufgrund des starken Kontrolllesepulses um etwa 120 dB, welche notwendig zur Detektion des schwachen Signals ist. Es wurde ein Aufbau mit gegenläufigen Nachweis- und Kontrollstrahlen gewählt, wodurch eine Unterdrückung des Kontrollpulses um etwa 80 dB erreicht werden konnte. Die verbleibende Unterdrückung von 40 dB wurde durch spektrales Filtern erreicht. Da sich die Frequenzen von Kontroll- und Signalpuls nur um ~ 10 MHz unterscheiden, wurde ein spektraler Filter basierend auf einem zweiten Pr:YSO Kristall aufgebaut, in welchem das Absorptionsspektrum mit Hilfe von optischem Pumpen flexibel an die Anforderungen angepasst werden konnte. Für kurze Speicherzeiten von 2 µs verbesserte der Filter die Unterdrückung des Kontrollpulses um 42 dB. Dies ermöglichte die Speicherung schwacher kohärenter Pulse mit einer mittleren Photonenzahl von 1,1 mit einer Effizienz von 42% und einem Signal-Hintergrund-Verhältnis von 3,2. Hierbei war die Effizienz durch die optische Dichte des Speichermediums limitiert. Durch Anwenden eines Aufbaus mit mehreren Durchläufen könnte diese weiter gesteigert werden. Das Signal-Hintergrund-Verhältnis war durch die verbleibende Transmission des Kontrollpulses durch den spektralen Filter begrenzt. Dennoch stellt das erreichte Ergebnis die erste Implementierung eines Speichers für einzelne Photonen mittels EIT in einem Festkörpermedium dar.

Zur Verlängerung der Kohärenzlebensdauer wurde die ZEFOZ Technik angewandt. Aufgrund des für ZEFOZ notwendigen Magnetfeldes, sank die optische Dichte des Pr:YSO Kristalls, was zu einer geringeren Speichereffizienz führte. Zunächst wurde die Lichtspeicherung unter ZEFOZ-Bedingungen bei einer kurzen Speicherzeit von 2 µs charakterisiert. Mittels eines Aufbaus mit drei Durchläufen und Formung des zeitlichen Profils des Nachweispulses konnte die reduzierte optische Dichte teilweise ausgeglichen werden und eine Effizienz von bis zu 23% bei Speicherung klassischer Lichtpulse erreicht werden. Um eine hohe Transmission des Aufbaus sicherzustellen, wurden zur Speicherung schwacher kohärenter Pulse lediglich zwei Durchläufe verwendet. Mit diesem Aufbau wurde die Speicherung schwacher kohärenter Pulse mit einer mittleren Photonenzahl von 10,2 für 2 µs mit einer Effizienz von 16% demonstriert. Hierbei war das Signal-Hintergrund-Verhältnis von 1,3 erneut durch die Resttransmission des Lesepulses durch den spektralen Filter begrenzt. Es hat sich gezeigt, dass diese Resttransmission von einem schwachen, aber spektral breiten Untergrund des Lasersystems herrührt.

Um die verlängerte Kohärenzlebensdauer bei der Speicherung von Lichtpulsen zu nutzen, wurden verschiedene Sequenzen zur Rephasierung mittels Radiofrequenzpulsen eingesetzt. Da es beim Entwurf der Radiofrequenzspulen Einschränkungen durch das ZEFOZ Spulensystem gab, wies das Radiofrequenzfeld eine signifikante Inhomogenität auf. Dies führte zu einer geringen Rephasierungseffizienz von 15% bei der Anwendung von zwei π Pulsen. Um diese Pulsfehler zu kompensieren, wur-

de universell robuste dynamische Dekohärenzkontrolle angewendet, wodurch die Rephasiereffizienz auf 40% gesteigert werden konnte. Der zeitliche Abstand der Rephasierungspulse konnte aufgrund nicht weiter untersuchter experimenteller Einschränkungen nicht unter 10 ms verringert werden, ohne Verluste in der Effizienz in Kauf zu nehmen. Dies beschränkte die Effektivität der dynamischen Dekohärenzkontrolle. Trotzdem konnte eine Speicherzeit von 7,5 s für klassische Lichtpulse erreicht werden und diese Zeitskala auch für die Speicherung schwacher kohärenter Pulse mit einer mittleren Photonenzahl von 52 bestätigt werden. Weiterhin wurden schwache kohärente Pulse mit unterschiedlicher Photonenzahl für 1,28 s gespeichert und ein Signal-Hintergrund-Verhältnis von 0,09 für die Speicherung eines einzelnen Photons extrapoliert. Für die Speicherung eines schwachen kohärenten Pulses mit einer mittleren Photonenzahl von 7 wurde eine Effizienz von 6% und ein Signal-Hintergrund-Verhältnis von 0,6 bestimmt. Dies stellt die erste Implementierung eines Speichers für schwache kohärente Lichtpulse nahe dem Einzelphotonenniveau mit Speicherzeiten im Bereich von Sekunden dar. Im Vergleich zum aktuellen Stand der Forschung zur Speicherung einzelner Photonen über möglichst lange Zeiten, also einer Speicherzeit von 100 ms [95], wurde somit in dieser Arbeit eine Steigerung von mehr als einer Größenordnung erreicht.

Die Untersuchungen wurden ergänzt um die Entwicklung, Implementierung und Charakterisierung neuartiger universell robuster Sequenzen für die Invertierung von Überlagerungszuständen und für den Transfer von Besetzung. Insbesondere wurden universelle komposite Pulse für Besetzungstransfer eingesetzt, welche besonders geeignet sind für Experimente, bei denen Pulsflächen- und Verstimmungsfehler korreliert sind. Es wurde gezeigt, dass das Anregungsprofil der Sequenz durch das Ändern der Phasen rotiert werden kann. Dies ermöglicht das Abstimmen der Sequenz auf die experimentell vorhandene Korrelationsstärke. Weiterhin wurde die erste experimentelle Implementierung von kompositem STIRAP demonstriert. Es wurde für verstimmtes STIRAP gezeigt, dass die Anwendung der Phasen universell robuster Pulse die Robustheit gegenüber Fehlern in beliebigen experimentellen Fehlern steigert. Für fünffach angewendetes STIRAP wurde eine Steigerung der Effizienz des Besetzungstransfers von 50% auf 85% mittels universell robustem kompositem STIRAP erzielt.

Appendix A

AFC Light Storage at ZEFOZ Conditions

The AFC light storage protocol is an alternative approach to EIT light storage. It was proposed by Afzelius *et al.* and first implemented by de Riedmatten *et al.* [23, 106]. For light storage via AFC, we optically prepare an absorption feature consisting of spectrally narrow, equally separated absorption peaks in an inhomogeneously broadened medium (see Figure A.1). When an incoming probe pulse, with a bandwidth matched to the AFC, is absorbed, it creates a total coherence which is the sum of many individual coherences. The spectral distribution of the individual coherences equals the absorption feature, i.e., it has the same periodicity δ_p. Since the transition frequency of each individual coherence determines the time evolution, the total coherence initially dephases (due to the broad frequency distribution) but the periodic structure causes a rephasing of the coherence after $t_{AFC} = 1/\delta_p$. The rephased coherence acts as a source for the electromagnetic field and causes the reemission of the absorbed pulse, i.e., the signal emission.

To enable longer storage times and on-demand readout, we can stop the time evolution of the optical coherence by mapping it to a ground state coherence. This is called AFC spin storage (AFCSS) and is achieved by applying an appropriate optical π pulse prior to t_{AFC}. This π pulse couples the optically excited state to an empty ground state and transfers the atomic coherence from the optical transition to the ground state transition. We can prolong the ground state coherence lifetime using the same techniques as described in the main text. For readout, we apply a second optical π pulse which maps the coherence back to the optical transition. Then, the time evolution of the optical coherence continues, leading to the signal emission.

Compared to EIT light storage, AFC has several advantages. First, during the signal emission, there is no other light field which enables background-free signal detection. Second, AFC enables simultaneous storage of multiple temporally separated probe pulses. When we apply several pulses to the AFC within t_{AFC}, i.e., before the first pulse is reemitted, then the corresponding signals are emitted in the same order as the probe pulses. The multimode capacity, i.e., the maximal number of simultaneously stored probe pulses, is given by the ratio of the total spectral width of the AFC

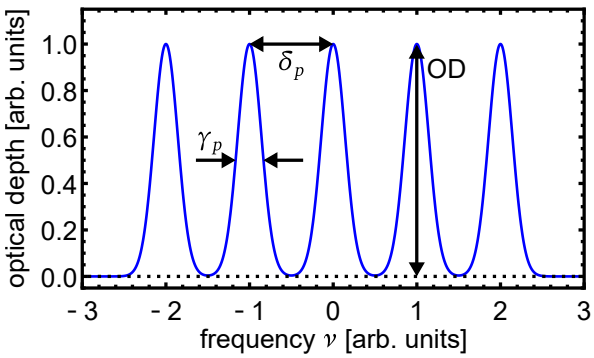

Figure A.1: Sketch of the absorption spectrum, i.e., OD versus frequency, of an AFC of Gaussian absorption peaks. The definition of the parameters peak optical depth OD, peak width (FWHM) γ_p, and peak separation δ_p are given in the plot.

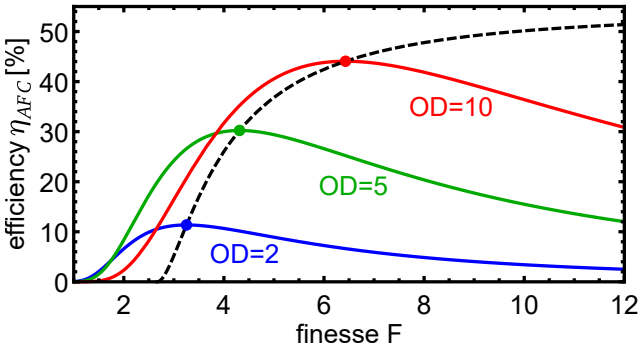

Figure A.2: AFC light storage efficiency η_{AFC} versus finesse F. The colored lines show η_{AFC} for different but constant OD. The dots indicate the position of the maxima. The dashed line shows the maximal efficiency versus F (note that the OD varies along the graph).

structure to the peak separation, i.e., the number of prepared peaks. Lastly, AFC enables storage of pulses with a higher bandwidth (given by the spectral width of the AFC structure) than usually possible with EIT where the EIT window width limits the bandwidth.

The efficiency η_{AFC} of AFC light storage depends on the shape of the individual absorption peaks [107]. For Gaussian peaks with peak optical depth OD and comb finesse $F = \delta_p/\gamma_p$, η_{AFC} is given by [23]

$$\eta_{AFC} = \frac{\pi}{\ln 2}\left(\frac{\mathrm{OD}}{2F}\right)^2 \exp\left(-\sqrt{\frac{\pi}{\ln 2}}\frac{\mathrm{OD}}{2F}\right)\exp\left(-\frac{\pi^2}{2F^2\ln 2}\right). \tag{A.1}$$

The colored graphs in Figure A.2 show the efficiency versus the finesse for different OD. The maximal efficiency (indicated by the dots) increases with the OD and shifts to higher finesse when the OD increases. Furthermore, the dashed line shows the maximal efficiency versus the finesse. The graph converges to $\eta_{AFC} = 4\exp(-2) \approx 54\%$ in the limit of infinite finesse (and consequently infinite OD). This is due to reabsorption of the signal pulse which we can avoid in a backward readout scheme [23, 108]. Backward readout requires optical π pulses with appropriate phase matching and enables efficiencies up to 100% in the limit of infinite OD.

As we saw in the main text, storage of single photons by EIT at the ZEFOZ point was not possible due to the strong control read pulse background. Using AFC light storage, we can avoid this background. However, at the ZEFOZ point, the pit width in which we can prepare the AFC is limited to 600 kHz. Due to the linewidth of the laser system, the minimum absorption peak width is ~ 50 kHz. Therefore, we have limited margins regarding the number of absorption peaks and the finesse of the AFC.

We implement AFC in Pr:YSO at the ZEFOZ point using a similar preparation sequence as described in Section 4.2. However, we use a different excited state for coupling the probe and mapping π pulses [see Figure A.3(a)] and prepare a pit with 550 kHz width. Furthermore, we do not prepare the additional pits for avoiding unintended population transfer as described in Section 4.2. In contrast to EIT, we now apply the control beamline to provide the mapping π pulses. The optical linewidth of the OPO-SFG laser system is ~ 100 kHz on a timescale of 100 ms. We prepare the AFC by a repumping pulse with several (simultaneous) frequencies, each corresponding to a peak of the AFC.

Using our preparation scheme, we achieve OD ≈ 1.4. According to Equation A.1, a finesse of $F = 3$ is optimal for reaching the maximal efficiency. Due to the linewidth of

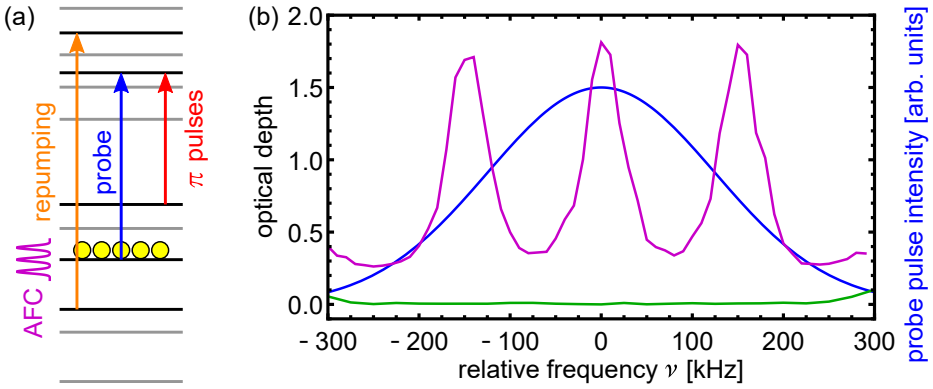

Figure A.3: (a) Level scheme for AFC light storage at the ZEFOZ point. (b) Measured OD versus frequency of the prepared AFC (purple) and the pit (green) before application of the repumping pulse. The AFC has a peak separation of $\delta_p = 150\,\text{kHz}$ and the peaks have a Gaussian shape with OD ≈ 1.4 and $\gamma_p \approx 50\,\text{kHz}$. Note the absorption baseline, i.e., background absorption, of OD ≈ 0.3. The blue graph shows the intensity spectrum of the stored probe pulse.

the laser system, the peak width is $\gamma_p \approx 50\,\text{kHz}$. Hence, we choose a peak separation of $\delta_p = F\gamma_p = 150\,\text{kHz}$ corresponding to an AFC storage time of $t_{AFC} = 6.7\,\mu\text{s}$. Figure A.3(b) shows the measured spectrum of the AFC. Due to the limited pit width given by the level structure, we can only prepare three peaks. With this low number of peaks we can barely match the probe pulse spectrum to cover several peaks but not exceed the total AFC width (which is required for high efficiency [23]). Additionally, a fit of the measured spectrum shows a baseline, i.e., background absorption, of OD ≈ 0.3 which causes $\sim 25\%$ absorption of the signal.

We use the AFC to store an probe pulse with Gaussian temporal shape with a FWHM of $1.5\,\mu\text{s}$. We chose the FWHM such that the spectral width of the pulse of $\sim 300\,\text{kHz}$ roughly matches the width of the AFC [see Figure A.3(b)]. Figure A.4 shows the probe and signal pulses of the experiment. We achieve a storage efficiency of $\eta_{AFC} = (5.3 \pm 0.3)\%$ which fits to the expected value of 5% (note that this expectation also consideres the 25% absorption due to the background absorption observed in the spectrum). In order to increase the storage efficiency, we can increase the OD of the medium using the multipass setup. However, due to the dependence of the efficiency on the finesse, this would also require a reduction of the peak width γ_p (note that

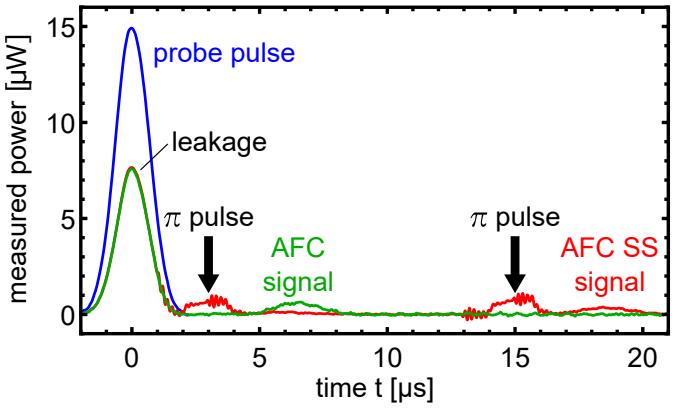

Figure A.4: Optical power versus time for AFC light storage. We store a Gaussian shaped probe pulse (blue) with $1.5\,\mu\text{s}$ FWHM. After $t_{AFC} = 6.7\,\mu\text{s}$, the signal (green) is emitted. We also perform AFCSS (red) by applying two optical π pulses with $2\,\mu\text{s}$ duration (visible in the red graph due to crosstalk between the optical paths). The AFCSS signal is emitted at $t = 18.7\,\mu\text{s}$.

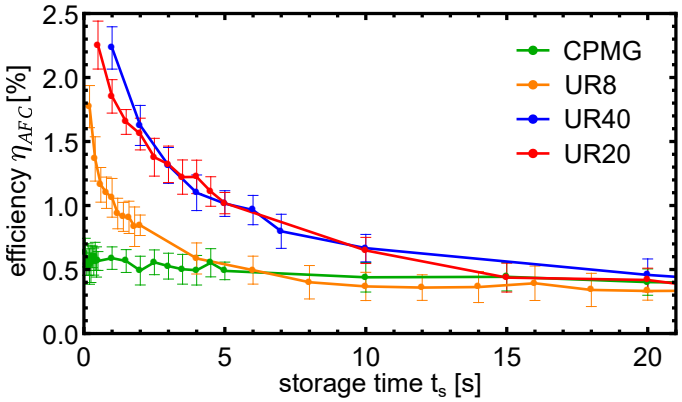

Figure A.5: AFCSS at the ZEFOZ point: Efficiency η_{AFC} versus storage time t_s for different rephasing sequences. For all sequences we use π pulses with a duration of 38 µs and a temporal separation of 25 ms.

the pit width limits δ_p). For example, in order to reach an efficiency of 50%, we require $F = 9.8$ and OD = 17. This means that if we keep the peak separation δ_p, we require a threefold reduction of γ_p. Furthermore, it is beneficial to use even lower δ_p as it increases t_{AFC} and enables storage of multiple temporally separated modes. Therefore, we conclude that we require a reduction of the linewidth of the laser system by at least a factor of 3 to enable significantly higher efficiencies.

In order to exploit the long coherence lifetime of the ZEFOZ point, we perform AFCSS. We apply two optical π pulses with $2\pi \times 250$ kHz Rabi frequency using the control beampath and 60 mW optical power. Due to crosstalk of the control and signal beam paths, the pulses are visible in the red graph in Figure A.4. However, it is possible to reduce the crosstalk below the noise level using a single mode fiber in front of the PD. The signal is now emitted 12 µs later, according to the delay between the π pulses. We calculate an efficiency of $\eta_{AFC} = (3.3 \pm 0.2)\%$, i.e., a reduction by about 38% compared to the pure AFC protocol. This reduction is partially due to the spin storage time of 12 µs which exceeds the dephasing time $T_2^* \approx 10$ µs and partially due to the imperfect transfer of the π pulses. We could reduce the latter by applying pulses with higher Rabi frequency or chirped pulses to cover the whole width of the AFC [109].

To counteract dephasing, we apply rephasing sequences on the ground state coherence using RF π pulses. We measure the storage efficiency η_{AFC} for different sequences of π pulses. In all sequences, we apply a π pulse every 25 ms and we vary the phases as described in Section 5.3. Figure A.5 shows η_{AFC} versus the storage time t_s. We find that the UR20 and UR40 sequences are superior to the UR8 and CPMG sequence which indicates the presence of pulse errors. At a storage time $t_s \approx 1$ s, we achieve a storage efficiency of $\eta_{AFC} \approx 2.3\%$. By fitting an exponential decay to η_{AFC} we find a 1/e time of ~ 4 s which is comparable to the results obtained using EIT light storage (see Chapter 6). However, for longer storage times, η_{AFC} converges to $\sim 0.4\%$ instead of decaying to 0. We explain this by imperfections of the RF pulses leading to population in the ground state of the optical π pulse transition and consequently to fluorescence after the application of the optical π pulse. We could reduce this effect by using the full preparation sequence described in Section 4.2, i.e., including the preparation of additional pits. Nevertheless, our result represents the first implementation of AFC light storage under ZEFOZ conditions in Pr:YSO reaching a storage time in the regime of seconds.

Our results demonstrate the feasibility of AFC light storage at the ZEFOZ point.

However, due to the linewidth of the laser system, the maximal finesse was limited and we could only prepare three AFC peaks. This restricted the probe pulse bandwidth and impeded multimode storage. In order to proceed toward higher storage efficiency, we could apply the multipass setup to increase the OD but would also require higher AFC finesse, i.e., narrower spectral peaks, which is not possible with the current OPO laser system. We did not explore the background noise level of our AFC memory but since AFC generally exhibits less noise than EIT, we expect no further limitations for proceeding toward storage on the single photon level in future work.

Recently, Ma *et al.* reported on AFC light storage at a ZEFOZ point in Eu^{3+}:Y_2SiO_5 [20]. Due to the superior coherence lifetime of Eu^{3+}:Y_2SiO_5, they achieved a storage time of up to 53 min which is almost 3 orders of magnitude longer than our result of 4 s. Furthermore, they prepared a slightly broader AFC with 1 MHz bandwidth, enabled by the larger level splittings in Eu^{3+}:Y_2SiO_5. Without mapping the coherence to the ground state, they achieved a storage efficiency of 4.5% which is comparable to our result. However, the mapping efficiency to the ground states and back was only $\sim$ 15%, limited by a non-optimal orientation of the polarization. Furthermore, the rephasing efficiency was in the range of $\sim$ 10%, even for application of a composite sequence. This limited the total storage efficiency to about 0.05% which is more than 40 times less than our result of 2.3%.

Bibliography

[1] A. Ekert and R. Jozsa. *Quantum computation and Shor's factoring algorithm.* Reviews of Modern Physics **68,** 733 (1996).

[2] T. D. Ladd *et al. Quantum computers.* Nature **464,** 45 (2010).

[3] P. Shor. *Algorithms for Quantum Computation: Discrete Logarithms and Factoring.* in *Proceedings of the 35th Annual Symposium on the Foundations of Computer Science* (ed S. Goldwasser) (IEEE Comput. Soc. Press, 1994), 124.

[4] R. P. Feynman. *Simulating Physics with Computers.* International Journal of Theoretical Physics **21,** 467 (1982).

[5] D. P. DiVincenzo. *Quantum Computation.* Science **270,** 255 (1995).

[6] H. J. Kimble. *The quantum internet.* Nature **453,** 1023 (2008).

[7] H.-J. Briegel, W. Dür, J. I. Cirac, and P. Zoller. *Quantum Repeaters: The Role of Imperfect Local Operations in Quantum Communication.* Physical Review Letters **81,** 5932 (1998).

[8] N. Sangouard *et al. Long-distance entanglement distribution with single-photon sources.* Physical Review A **76,** 050301(R) (2007).

[9] C. Simon *et al. Quantum Repeaters with Photon Pair Sources and Multimode Memories.* Physical Review Letters **98,** 190503 (2007).

[10] C. Simon *et al. Quantum memories.* The European Physical Journal D **58,** 1 (2010).

[11] Y.-F. Hsiao *et al. Highly Efficient Coherent Optical Memory Based on Electromagnetically Induced Transparency.* Physical Review Letters **120,** 183602 (2018).

[12] Y. Wang *et al. Efficient quantum memory for single-photon polarization qubits.* Nature Photonics **13,** 346 (2019).

[13] B. Zhao *et al. A millisecond quantum memory for scalable quantum networks.* Nature Physics **5,** 95 (2009).

[14] U. Schnorrberger *et al. Electromagnetically Induced Transparency and Light Storage in an Atomic Mott Insulator.* Physical Review Letters **103,** 033003 (2009).

[15] R. Zhang, S. R. Garner, and L. V. Hau. *Creation of Long-Term Coherent Optical Memory via Controlled Nonlinear Interactions in Bose-Einstein Condensates.* Physical Review Letters **103,** 233602 (2009).

[16] Y. O. Dudin, L. Li, and A. Kuzmich. *Light storage on the time scale of a minute.* Physical Review A **87,** 031801(R) (2013).

[17] O. Katz and O. Firstenberg. *Light storage for one second in room-temperature alkali vapor.* Nature Communications **9,** 2074 (2018).

[18] G. Heinze. *Kohärente optische Datenspeicherung mittels EIT in einem Pr^{3+}:Y_2SiO_5-Kristall.* Dissertation, Technische Universität Darmstadt (2013).

[19] G. Heinze, C. Hubrich, and T. Halfmann. *Stopped Light and Image Storage by Electromagnetically Induced Transparency up to the Regime of One Minute.* Physical Review Letters **111,** 033601 (2013).

[20] Y. Ma, Y.-Z. Ma, Z.-Q. Zhou, C.-F. Li, and G.-C. Guo. *One-hour coherent optical storage in an atomic frequency comb memory.* Nature Communications **12,** 2381 (2021).

[21] P. Jobez *et al. Coherent Spin Control at the Quantum Level in an Ensemble-Based Optical Memory.* Physical Review Letters **114,** 230502 (2015).

[22] D. Schraft, M. Hain, N. Lorenz, and T. Halfmann. *Stopped Light at High Storage Efficiency in a Pr^{3+}:Y_2SiO_5 Crystal.* Physical Review Letters **116,** 073602 (2016).

[23] M. Afzelius, C. Simon, H. de Riedmatten, and N. Gisin. *Multimode quantum memory based on atomic frequency combs.* Physical Review A **79,** 052329 (2009).

[24] A. L. Alexander, J. J. Longdell, M. J. Sellars, and N. B. Manson. *Photon Echoes Produced by Switching Electric Fields.* Physical Review Letters **96,** 043602 (2006).

[25] Y.-W. Cho *et al. Highly efficient optical quantum memory with long coherence time in cold atoms.* Optica **3,** 100 (2016).

[26] S. P. Horvath *et al. Noise-free on-demand atomic frequency comb quantum memory.* Physical Review Research **3,** 023099 (2021).

[27] K. F. Reim *et al. Towards high-speed optical quantum memories.* Nature Photonics **4,** 218 (2010).

[28] C. Liu, Z. Dutton, C. H. Behroozi, and L. V. Hau. *Observation of coherent optical information storage in an atomic medium using halted light pulses.* Nature **409,** 490 (2001).

[29] D. F. Phillips, A. Fleischhauer, A. Mair, R. L. Walsworth, and M. D. Lukin. *Storage of Light in Atomic Vapor.* Physical Review Letters **86,** 783 (2001).

[30] M. Fleischhauer and M. D. Lukin. *Dark-State Polaritons in Electromagnetically Induced Transparency.* Physical Review Letters **84,** 5094 (2000).

[31] M. Fleischhauer and M. D. Lukin. *Quantum memory for photons: Dark-state polaritons.* Physical Review A **65,** 022314 (2002).

[32] M. Fleischhauer, A. Imamoglu, and J. P. Marangos. *Electromagnetically induced transparency: Optics in coherent media.* Reviews of Modern Physics **77,** 633 (2005).

[33] A. V. Gorshkov, A. André, M. Fleischhauer, A. S. Sørensen, and M. D. Lukin. *Universal Approach to Optimal Photon Storage in Atomic Media.* Physical Review Letters **98,** 123601 (2007).

[34] A. Gorshkov, A. André, M. Lukin, and A. Sørensen. *Photon storage in Λ-type optically dense atomic media. II. Free-space model.* Physical Review A **76,** 033805 (2007).

[35] M. Hain. *Increasing the EIT Light Storage Efficiency in Pr^{3+}:Y_2SiO_5 Using Multipass Configurations.* Master's Thesis, Technische Universität Darmstadt (2016).

[36] A. S. Zibrov *et al. Transporting and Time Reversing Light via Atomic Coherence.* Physical Review Letters **88,** 103601 (2002).

[37] N. Lorenz. *Optimising EIT Light Storage Efficiency in Pr^{3+}:Y_2SiO_5.* Master's Thesis, Technische Universität Darmstadt (2014).

[38] M. D. Lukin, S. F. Yelin, and M. Fleischhauer. *Entanglement of Atomic Ensembles by Trapping Correlated Photon States.* Physical Review Letters **84,** 4232 (2000).

[39] I. Novikova *et al. Optimal Control of Light Pulse Storage and Retrieval.* Physical Review Letters **98,** 243602 (2007).

[40] I. Novikova, R. Walsworth, and Y. Xiao. *Electromagnetically induced transparency-based slow and stored light in warm atoms.* Laser & Photonics Reviews **6,** 333 (2012).

[41] K. Holliday, M. Croci, E. Vauthey, and U. P. Wild. *Spectral hole burning and holography in an Y_2SiO_5:Pr^{3+} crystal.* Physical Review B **47,** 14741 (1993).

[42] R. W. Equall, R. L. Cone, and R. M. Macfarlane. *Homogeneous broadening and hyperfine structure of optical transitions in Pr^{3+}:Y_2SiO_5.* Physical Review B **52,** 3963 (1995).

[43] S. Mieth. *Preserving Atomic Coherences for Light Storage in Pr^{3+}:Y_2SiO_5 Driven by an OPO Laser System.* Dissertation, Technische Universität Darmstadt (2015).

[44] D. Schraft. *Composite and Adiabatic Techniques for Efficient EIT Light Storage in Pr^{3+}:Y_2SiO_5.* Dissertation, Technische Universität Darmstadt (2016).

[45] G. T. Genov, D. Schraft, and T. Halfmann. *Rephasing efficiency of sequences of phased pulses in spin-echo and light-storage experiments.* Physical Review A **98,** 063836 (2018).

[46] E. Fraval, M. J. Sellars, A. Morrison, and A. Ferris. *Pr–Y interaction in Pr^{3+}:Y_2SiO_5.* Journal of Luminescence **107,** 347 (2004).

[47] L. Viola and S. Lloyd. *Dynamical suppression of decoherence in two-state quantum systems.* Physical Review A **58,** 2733 (1998).

[48] L. Viola, E. Knill, and S. Lloyd. *Dynamical Decoupling of Open Quantum Systems.* Physical Review Letters **82,** 2417 (1999).

[49] D. Suter and G. A. Álvarez. *Colloquium: Protecting quantum information against environmental noise.* Reviews of Modern Physics **88,** 041001 (2016).

[50] A. M. Souza, G. A. Álvarez, and D. Suter. *Robust dynamical decoupling.* Philosophical Transactions of the Royal Society A: Mathematical, Physical and Engineering Sciences **370,** 4748 (2012).

[51] C. Hardy, W. Edelstein, and D. Vatis. *Efficient Adiabatic Fast Passage for NMR Population Inversion in the Presence of Radiofrequency Field Inhomogeneity and Frequency Offsets.* Journal of Magnetic Resonance **66,** 470 (1986).

[52] M. Garwood and L. DelaBarre. *The Return of the Frequency Sweep: Designing Adiabatic Pulses for Contemporary NMR.* Journal of Magnetic Resonance **153,** 155 (2001).

[53] M. F. Pascual-Winter, R.-C. Tongning, T. Chanelière, and J.-L. Le Gouët. *Securing coherence rephasing with a pair of adiabatic rapid passages.* New Journal of Physics **15,** 055024 (2013).

[54] X. Chen, I. Lizuain, A. Ruschhaupt, D. Guéry-Odelin, and J. G. Muga. *Shortcut to Adiabatic Passage in Two- and Three-Level Atoms.* Physical Review Letters **105,** 123003 (2010).

[55] M. H. Levitt and R. Freeman. *NMR population inversion using a composite pulse.* Journal of Magnetic Resonance **33,** 473 (1979).

[56] M. A. Ali Ahmed, G. A. Álvarez, and D. Suter. *Robustness of dynamical decoupling sequences.* Physical Review A **87,** 042309 (2013).

[57] G. T. Genov, D. Schraft, N. V. Vitanov, and T. Halfmann. *Arbitrarily Accurate Pulse Sequences for Robust Dynamical Decoupling.* Physical Review Letters **118,** 133202 (2017).

[58] G. T. Genov, D. Schraft, T. Halfmann, and N. V. Vitanov. *Correction of Arbitrary Field Errors in Population Inversion of Quantum Systems by Universal Composite Pulses.* Physical Review Letters **113,** 043001 (2014).

[59] J. Zessin. *Dynamische und statische Dekohärenzkontrolle bei effizienter EIT-Lichtspeicherung in Pr^{3+}:Y_2SiO_5.* Master's Thesis, Technische Universität Darmstadt (2017).

[60] N. Bloembergen. *On the interaction of nuclear spins in a crystalline lattice.* Physica **15,** 386 (1949).

[61] M. Zhong *et al. Optically addressable nuclear spins in a solid with a six-hour coherence time.* Nature **517,** 177 (2015).

[62] E. Fraval. *Minimising the Decoherence of Rare Earth Ion Solid State Spin Qubits.* Dissertation, Australian National University, Canberra (2006).

[63] M. Lovrić, P. Glasenapp, and D. Suter. *Spin Hamiltonian characterization and refinement for Pr^{3+}:$YAlO_3$ and Pr^{3+}:Y_2SiO_5.* Physical Review B **85,** 014429 (2012).

[64] J. J. Longdell, A. L. Alexander, and M. J. Sellars. *Characterization of the hyperfine interaction in europium-doped yttrium orthosilicate and europium chloride hexahydrate.* Physical Review B **74,** 195101 (2006).

[65] E. Fraval, M. J. Sellars, and J. J. Longdell. *Method of Extending Hyperfine Coherence Times in Pr^{3+}:Y_2SiO_5.* Physical Review Letters **92,** 077601 (2004).

[66] E. Fraval, M. J. Sellars, and J. J. Longdell. *Dynamic Decoherence Control of a Solid-State Nuclear-Quadrupole Qubit.* Physical Review Letters **95,** 030506 (2005).

[67] J. J. Longdell, E. Fraval, M. J. Sellars, and N. B. Manson. *Stopped Light with Storage Times Greater than One Second Using Electromagnetically Induced Transparency in a Solid.* Physical Review Letters **95,** 063601 (2005).

[68] S. E. Beavan, E. Fraval, M. J. Sellars, and J. J. Longdell. *Demonstration of the reduction of decoherent errors in a solid-state qubit using dynamic decoupling techniques.* Physical Review A **80,** 032308 (2009).

[69] G. Heinze, C. Hubrich, and T. Halfmann. *Coherence time extension in Pr^{3+}:Y_2SiO_5 by self-optimized magnetic fields and dynamical decoupling.* Physical Review A **89,** 053825 (2014).

[70] S. Mieth, A. Henderson, and T. Halfmann. *Tunable, continuous-wave optical parametric oscillator with more than 1W output power in the orange visible spectrum.* Optics Express **22,** 11182 (2014).

[71] G. T. Moore and K. Koch. *Optical Parametric Oscillation with Intracavity Sum-Frequency Generation.* IEEE Journal of Quantum Electronics **29,** 961 (1993).

[72] W. R. Bosenberg, J. I. Alexander, L. E. Myers, and R. W. Wallace. *2.5-W, continuous-wave, 629-nm solid-state laser source.* Optics Letters **23,** 207 (1998).

[73] R. V. Pound. *Electronic Frequency Stabilization of Microwave Oscillators.* Review of Scientific Instruments **17,** 490 (1946).

[74] R. W. P. Drever *et al. Laser Phase and Frequency Stabilization Using an Optical Resonator.* Applied Physics B **31,** 97 (1983).

[75] E. A. Donley, T. P. Heavner, F. Levi, M. O. Tataw, and S. R. Jefferts. *Double-pass acousto-optic modulator system.* Review of Scientific Instruments **76,** 063112 (2005).

[76] C. Li, C. Wyon, and R. Moncorgé. *Spectroscopic Properties and Fluorescence Dynamics of Er^{3+} and Yb^{3+} in Y_2SiO_5.* IEEE Journal of Quantum Electronics **28,** 1209 (1992).

[77] M. Stabel. *EIT Light Storage of Weak Coherent Pulses in Pr^{3+}:Y_2SiO_5.* Master's Thesis, Technische Universität Darmstadt (2019).

[78] J. Mlynek, N. C. Wong, R. G. DeVoe, E. S. Kintzer, and R. G. Brewer. *Raman Heterodyne Detection of Nuclear Magnetic Resonance.* Physical Review Letters **50,** 993 (1983).

[79] N. C. Wong, E. S. Kintzer, J. Mlynek, R. G. DeVoe, and R. G. Brewer. *Raman heterodyne detection of nuclear magnetic resonance.* Physical Review B **28,** 4993 (1983).

[80] D. C. Meeker. *Finite Element Method Magnetics (version 4.2)*. 2019.

[81] M. Nilsson, L. Rippe, N. Ohlsson, T. Christiansson, and S. Kröll. *Initial Experiments Concerning Quantum Information Processing in Rare-Earth-Ion Doped Crystals.* Physica Scripta **T102,** 178 (2002).

[82] M. Nilsson, L. Rippe, S. Kröll, R. Klieber, and D. Suter. *Hole-burning techniques for isolation and study of individual hyperfine transitions in inhomogeneously broadened solids demonstrated in Pr^{3+}:Y_2SiO_5.* Physical Review B **70,** 214116 (2004).

[83] S. E. Beavan, E. A. Goldschmidt, and M. J. Sellars. *Demonstration of a dynamic bandpass frequency filter in a rare-earth ion-doped crystal.* Journal of the Optical Society of America B **30,** 1173 (2013).

[84] A. Kinos, Q. Li, L. Rippe, and S. Kröll. *Development and characterization of high suppression and high étendue narrowband spectral filters.* Applied Optics **55,** 10442 (2016).

[85] M. Gündoğan, P. M. Ledingham, K. Kutluer, M. Mazzera, and H. de Riedmatten. *Solid State Spin-Wave Quantum Memory for Time-Bin Qubits.* Physical Review Letters **114,** 230501 (2015).

[86] M. Sabooni, A. N. Nilsson, G. Kristensson, and L. Rippe. *Wave propagation in birefringent materials with off-axis absorption or gain.* Physical Review A **93,** 013842 (2016).

[87] G. H. Zhang, B. Braverman, A. Kawasaki, and V. Vuletić. *Note: Fast compact laser shutter using a direct current motor and three-dimensional printing.* Review of Scientific Instruments **86,** 126105 (2015).

[88] J. Huang, J. M. Zhang, A. Lezama, and T. W. Mossberg. *Excess Dephasing in Photon-Echo Experiments Arising from Excitation-Induced Electronic Level Shifts.* Physical Review Letters **63,** 78 (1989).

[89] B. Lauritzen *et al. Spectroscopic investigations of* Eu^{3+}*:*Y_2SiO_5 *for quantum memory applications.* Physical Review B **85,** 115111 (2012).

[90] H. Y. Carr and E. M. Purcell. *Effects of Diffusion on Free Precession in Nuclear Magnetic Resonance Experiments.* Physical Review **94,** 630 (1954).

[91] S. Meiboom and D. Gill. *Modified Spin-Echo Method for Measuring Nuclear Relaxation Times.* Review of Scientific Instruments **29,** 688 (1958).

[92] M. H. Levitt. *Composite Pulses.* Progress in Nuclear Magnetic Resonance Spectroscopy **18,** 61 (1986).

[93] R. Lauro, T. Chanelière, and J.-L. Le Gouët. *Adiabatic refocusing of nuclear spins in* Tm^{3+}*:YAG.* Physical Review B **83,** 035124 (2011).

[94] D. Daems, A. Ruschhaupt, D. Sugny, and S. Guérin. *Robust Quantum Control by a Single-Shot Shaped Pulse.* Physical Review Letters **111,** 050404 (2013).

[95] M. Körber *et al. Decoherence-protected memory for a single-photon qubit.* Nature Photonics **12,** 18 (2018).

[96] M. Krystek and M. Anton. *A weighted total least-squares algorithm for fitting a straight line.* Measurement Science and Technology **18,** 3438 (2007).

[97] G. T. Genov, M. Hain, N. V. Vitanov, and T. Halfmann. *Universal composite pulses for efficient population inversion with an arbitrary excitation profile.* Physical Review A **101,** 013827 (2020).

[98] K. Bergmann, N. V. Vitanov, and B. W. Shore. *Perspective: Stimulated Raman adiabatic passage: The status after 25 years.* The Journal of Chemical Physics **142,** 170901 (2015).

[99] N. V. Vitanov, A. A. Rangelov, B. W. Shore, and K. Bergmann. *Stimulated Raman adiabatic passage in physics, chemistry, and beyond.* Reviews of Modern Physics **89,** 015006 (2017).

[100] B. T. Torosov and N. V. Vitanov. *Composite stimulated Raman adiabatic passage.* Physical Review A **87,** 043418 (2013).

[101] A. Bruns, G. T. Genov, M. Hain, N. V. Vitanov, and T. Halfmann. *Experimental demonstration of composite stimulated Raman adiabatic passage.* Physical Review A **98,** 053413 (2018).

[102] F. Beil, T. Halfmann, F. Remacle, and R. D. Levine. *Logic operations in a doped solid driven by stimulated Raman adiabatic passage.* Physical Review A **83,** 033421 (2011).

[103] A. Bruns. *Population Transfer by Composite Stimulated Raman Adiabatic Passage.* Master's Thesis, Technische Universität Darmstadt (2017).

[104] N. V. Vitanov and S. Stenholm. *Analytic properties and effective two-level problems in stimulated Raman adiabatic passage.* Physical Review A **55,** 648 (1997).

[105] N. V. Vitanov, T. Halfmann, B. W. Shore, and K. Bergmann. *Laser Induced Population Transfer by Adiabatic Passage Techniques.* Annual Review of Physical Chemistry **52,** 763 (2001).

[106] H. de Riedmatten, M. Afzelius, M. U. Staudt, C. Simon, and N. Gisin. *A solid-state light–matter interface at the single-photon level.* Nature **456,** 773 (2008).

[107] T. Chanelière, J. Ruggiero, M. Bonarota, M. Afzelius, and J.-L. Le Gouët. *Efficient light storage in a crystal using an atomic frequency comb.* New Journal of Physics **12,** 023025 (2010).

[108] N. Sangouard, C. Simon, M. Afzelius, and N. Gisin. *Analysis of a quantum memory for photons based on controlled reversible inhomogeneous broadening.* Physical Review A **75,** 032327 (2007).

[109] M. Afzelius *et al. Demonstration of Atomic Frequency Comb Memory for Light with Spin-Wave Storage.* Physical Review Letters **104,** 040503 (2010).

Publications and Contributions to Conferences

Publications in Peer-Reviewed Journals

- G. T. Genov, M. Hain, N. V. Vitanov, and T. Halfmann.
  Universal composite pulses for efficient population inversion with an arbitrary excitation profile.
  Physical Review A **101**, 013827 (2020)

- A. Bruns, G. T. Genov, M. Hain, N. V. Vitanov, and T. Halfmann.
  Experimental demonstration of composite stimulated Raman adiabatic passage.
  Physical Review A **98**, 053413 (2018)

- D. Schraft, M. Hain, N. Lorenz, and T. Halfmann.
  Stopped Light at High Storage Efficiency in a Pr^{3+}:Y_2SiO_5 Crystal.
  Physical Review Letters **116**, 073602 (2016)

Manuscripts in Preparation

- M. Hain, M. Stabel, and T. Halfmann.
  Solid-State Few-Photon Storage on a Second Timescale Using Electromagnetically Induced Transparency.

Talks at International Conferences

- M. Hain, T. Weidner, and T. Halfmann.
  AFC Light Storage Under ZEFOZ Condition in Pr:YSO and Eu:YSO.
  Workshop on Rare-Earth Ions XIII (REIW XIII) – Geneva (Switzerland), October 2018

- M. Hain, N. Lorenz, D. Schraft, and T. Halfmann.
  Stopped Light at High Storage Efficiency in a Pr^{3+}:Y_2SiO_5 Crystal.
  Workshop on Control of Quantum Dynamics of Atoms, Molecules and Ensembles by Light (CAMEL XII) – Nessebar (Bulgaria), June 2016

- M. Hain, N. Lorenz, D. Schraft, and T. Halfmann.
  Light storage by EIT, using multi-pass configurations in a doped solid to reach efficiencies up to 76%.
  Conference on Quantum Light-Matter Interaction in Solid State Systems (QLIMS) – Marie Curie Initial Training Network CIPRIS – Barcelona (Spain), November 2015

Posters at National and International Conferences

- D. Schraft, M. Hain, N. Lorenz, and T. Halfmann.
  Stopped Light at High Storage Efficiency in a Pr^{3+}:Y_2SiO_5 Crystal.
  662. WE-Heraeus-Seminar on Quantum Networks – from building blocks to application (QUANET) – Bad Honnef (Germany), February 2018

- M. Hain, D. Schraft, N. Lorenz, and T. Halfmann.
  Stopped Light at High Storage Efficiency in a Pr^{3+}:Y_2SiO_5 Crystal.
  European Conference on Atoms Molecules and Photons 12 (ECAMP 12) – Frankfurt am Main (Germany), September 2016

Supervisions and Contributions to Teaching

Master's Thesis

- Markus Stabel. *EIT Light Storage of Weak Coherent Pulses in Pr^{3+}:Y_2SiO_5*. 2019
- Alexander Bruns. *Population Transfer by Composite Stimulated Raman Adiabatic Passage*. 2017
- Jonas Zessin. *Dynamische und statische Dekohärenzkontrolle bei effizienter EIT-Lichtspeicherung in Pr^{3+}:Y_2SiO_5*. 2017
- Thomas Weidner. *Aufbau eines Magnetfeldsystems zur Verlängerung der Kohärenzzeiten in Eu^{3+}:Y_2SiO_5*. 2017

Bachelor's Thesis

- Maurice Bardel. *Steigerung der Lichtspeichereffizienz in atomaren Frequenzkämmen in Pr^{3+}:Y_2SiO_5 mittels Mehrfachreflexion*. 2019
- Benedikt Moneke. *Laserfrequenzstabilisierung mit AOM für atomare Frequenzkämme in Pr^{3+}:Y_2SiO_5*. 2018
- Lucas Bialowons. *Optical Preparation for EIT Light Storage in Pr:YSO at ZEFOZ Conditions*. 2017

Internships and Laboratory Courses

- Supervision of Advanced Lab Courses
  - *Acousto-Optic Modulator* (04/2016 – 08/2019)
  - *Hong-Ou-Mandel Effect* (12/2016 – 02/2019)
- Supervision of Laboratory Internship "Miniforschung"
  - Benedikt Moneke. *Implementierung eines spektralen Filters in Pr^{3+}:Y_2SiO_5*. 2018
- Supervision of Basic Lab Courses
  - Optics: *Polarization and Birefringence*, *Optical Spectral Analysis* (WS 2014/15)
  - Nuclear Physics: *Absorption of γ Radiation*, *Dosimetry and Radiation Protection*, *Artificial Radioactivity*, *Deflection of β Rays* (WS 2012/13 – SS 2014)
  - Electricity: *Phase Shift*, *Millikan Experiment* (SS 2012)

Contributions to Teaching

- Supervision of Exercise Groups
  - *Physics IV* (SS 2015)
  - *Specialist Course "Optics"* (WS 2014/15)
  - *Physics II for Chemists* (SS 2014)
- Labtours 2016 – 2019

Erklärung gemäß §9 Promotionsordnung

Hiermit versichere ich, dass ich die vorliegende Dissertation selbstständig angefertigt und keine anderen als die angegebenen Quellen und Hilfsmittel verwendet habe. Alle wörtlichen und paraphrasierten Zitate wurden angemessen kenntlich gemacht. Die Arbeit hat bisher noch nicht zu Prüfungszwecken gedient.

Darmstadt, 29. Juni 2021

(Marcel Hain)